Title
Characterization of Degradation Mechanisms in Energy Generation and Storage Devices for Extended Lifetimes

Author
Scharf, Jonathan

Publication Date
2021

UNIVERSITY OF CALIFORNIA SAN DIEGO

Characterization of Degradation Mechanisms in Energy Generation and Storage Devices for Extended Lifetimes

A dissertation submitted in partial satisfaction of the
requirements for the degree Doctor of Philosophy

in

NanoEngineering

by

Jonathan David Scharf

Committee in charge:
- Professor Ying Shirley Meng, Chair
- Professor David Fenning, Co-chair
- Professor Prab Bandaru
- Professor Renkun Chen
- Professor Joseph Wang

2021

The dissertation of Jonathan David Scharf is approved, and it is acceptable in quality and form for publication on microfilm and electronically.

University of California San Diego

2021

DEDICATION

To my wonderful family and friends

My success and purpose originate from the love, care, and support you have blessed me with

TABLE OF CONTENTS

LIST OF FIGURES

LIST OF SUPPLEMENTARY FIGURES

LIST OF TABLES

LIST OF SUPPLEMENTAL MATERIAL

ACKNOWLEDGEMENTS

I would like to thank my advisor Professor Ying Shirley Meng for all the support, opportunities, and guidance in my personal life, academic research, and future career. I would also like to thank my committee Co-Chair Professor David Fenning for his support at the start of my PhD. I would like to recognize my committee Chairs, Professor Joseph Wang and Professor Prab Bandaru for their guidance and collaboration in research projects and Professor Renkun Chen for his valuable feedback.

I am extremely grateful toward the past and present members of the Zinc battery team, Dr. Jean-Marie Doux, Christopher Redquest, Lu Yin, Xueying Li, and George Duong. I am also exceedingly grateful for the post-doctoral mentors that have guided me along my way, Dr. Abhik Banerjee, Dr. Weikang Li, and Dr. Micheol Kim. The compassion, patience, and intellect of the people in my team are unparalleled and I am so incrediblely grateful to have worked along side them. Special thanks as well to my friends within my research group, Øystein Fjeldberg, Macwin Savio Dsouza, Ashley Cronk, Bingyu Lu, and Yin Yijie. The greats times we shared gave me the strength to preserver and accomplish what was before me.

I would also like to thank Dr. Jeff Ortega and Dr. Xia Wei at ZPower LLC and Derrick Lin at Qualcomm for their insight and experience in aiding in my research projects. Both Dr. Ortega and Dr. Wei provided invaluable expertise in electrochemistry and battery fabrication that proved pivotal for the success of projects, and Derrick Lin provided insights on circuitry necessary for the development of demonstratable prototypes. I would like to thank Professor Alejandro Franco and Mehdi Chouchane at the Université de Picardie Jules Verne and Dr. Donal Finnegan at the National Renewable Energy Lab (NREL) for the collaboration and guidance in research projects and publications. I would also like to thank Dr. Eric Bushong at UCSD's National Center for Microscopy and Imaging Research (NCMIR) facility, who aided with a considerable amount of time and effort in training and assisting in the use of X-ray Computed Tomography for battery research.

I would like to thank my family and friends for giving me their support during my time at UCSD. The effort spent earning this degree provided me with an enhanced perspective on the wonderful values instilled in me growing up. The values my family provided allowed me to earn this degree, and for this, I am incredibly grateful. To my friends, words cannot express my gratitude. You gave me a family more than two thousand miles from my home. Thank you.

I acknowledge the financial support from ZPower LLC, United States and Qualcomm, United States. I also acknowledge the support by the U.S. Department of Energy's Office of Energy Efficiency and Renewable Energy under Solar Energy Technologies Office Agreement Number DE-EE0007751. For use of the MicroCT system, I acknowledge the National Center for Microscopy and Imaging Research (NCMIR) technologies and instrumentation supported by grant R24GM137200 from the National Institute of General Medical Sciences. I also acknowledge the San Diego Nanotechnology Infrastructure (SDNI) of UCSD, NANO3, a member of the National Nanotechnology Coordinated Infrastructure, which is supported by the National Science Foundation (Grant ECCS-1542148

Chapter 1, in full, is a reprint of the material "Quantification of Sodium-Ion Migration in Silicon Nitride by Flatband-Potential Monitoring at Device-Operating Temperatures." Guillaume von Gastrow, Erick Martinez-Loran, Jonathan Scharf, Jacob Clenney, Rico Meier, Prabhakar Bandaru, Mariana I. Bertoni, and David P. Fenning. Physica Status Solidi (a) 217, no. 16 (August

2020): 2000212. The dissertation author was the first author of this paper, all authors contributed to this work.

Chapter 2, in full, is a reprint of the material "High Performance Printed AgO-Zn Rechargeable Battery for Flexible Electronics." Yin, Lu, Jonathan Scharf, Jessica Ma, Jean-Marie Doux, Christopher Redquest, Viet L. Le, Yijie Yin, Jeff Ortega, Xia Wei, Joseph Wang, Ying Shirley Meng, Joule 5, no. 1 (2021): 228-248. The dissertation author was the first author of this paper, all authors contributed to this work.

Chapter 3, in full, has been submitted for publication as “Bridging Nano and Micro-scale X-ray Tomography for Battery Research by Leveraging Artificial Intelligence” as a review article in Nature Nanotechnology. Jonathan Scharf, Mehdi Chouchane, Donal P. Finegan, Bingyu Lu, Christopher Redquest, Min-cheol Kim, Weiliang Yao, Alejandro A. Franco, Dan Gostovic, Zhao Liu, Mark Riccio, František Zelenka, Jean-Marie Doux, Ying Shirley Meng. The dissertation author was the first author of this paper, all authors contributed to this work.

Chapter 4, in full, is to be submitted for publication as “Investigating Failure Modes in Zn-AgO Aqueous Batteries with In-Situ X-Ray Micro Computed Tomography.” in ACS Applied Energy Materials. Jonathan Scharf, Lu Yin, Christopher Redquest, Ruixiao Liu, Jeff Ortega, Xia Wei, Joseph Wang, Jean-Marie Doux, Ying Shirley Meng. The dissertation author was the first author of this paper, all authors contributed to this work.

VITA

2016	Bachelor of Science, Electrical Engineering, University of Massachusetts Amherst
2017	Master of Science, NanoEngineering, University of California San Diego
2021	Doctor of Philosophy, NanoEngineering, University of California San Diego

PUBLICATIONS

(* = authors contributed equally to the work)

1. Jonathan Scharf, Lu Yin, Christopher Redquest, Ruixiao Liu, Jeff Ortega, Xia Wei, Joseph Wang, Jean-Marie Doux, Ying Shirley Meng, "Investigating Failure Modes in Zn-AgO Aqueous Batteries with In-Situ X-Ray Micro Computed Tomography." *Submitted to ACS Applied Energy Materials (2021)*

2. Jonathan Scharf, Mehdi Chouchane, Donal P. Finegan, Bingyu Lu, Christopher Redquest, Min-cheol Kim, Weiliang Yao, et al., "Bridging Nano and Micro-scale X-ray Tomography for Battery Research by Leveraging Artificial Intelligence." *Submitted to Nature Nanotechnology (2021)*

3. Lu Yin*, Jonathan Scharf*, Jessica Ma, Jean-Marie Doux, Christopher Redquest, Viet L. Le, Yijie Yin et al. "High Performance Printed AgO-Zn Rechargeable Battery for Flexible Electronics." Joule 5, no. 1 (2021): 228-248.

4. Guillaume von Gastrow*, Erick Martinez-Loran*, Jonathan Scharf*, Jacob Clenney, Rico Meier, Prabhakar Bandaru, Mariana I. Bertoni, and David P. Fenning. "Quantification of Sodium-Ion Migration in Silicon Nitride by Flatband-Potential Monitoring at Device-Operating Temperatures." physica status solidi (a) 217, no. 16 (2020): 2000212.

5. Darren H. S. Tan, Yu-Ting Chen, Hedi Yang, Wurigumula Bao, Bhagath Sreenarayanan, Jean-Marie Doux, Weikang Li, Bingyu Lu, So-Yeon Ham, Baharak Sayahpour, Jonathan Scharf,

Erik A. Wu, *et al.*, “Carbon Free High Loading Silicon Anodes Enabled by Sulfide SolidElectrolytes for Robust All Solid-State Batteries” *In Review with Science (2021)*

6. Bingyu Lu, Edgar Olivera, Jonathan Scharf, Mehdi Chouchane, Chengcheng Fang, Miguel Ceja, Lisa Pangilinan *et al.* "Quantitatively Designing Porous Copper Current Collectors for Lithium Metal Anode", *In Review with ACS Applied Energy Materials (2021)*

7. Guorui Cai, Yijie Yin, Dawei Xia, Amanda A. Chen, John Holoubek, Jonathan Scharf *et al.*, “Sub-Nanometer Confinement Enables Gas Electrolyte for Extremely Low-Temperature Batteries with Reduced Operation Pressure”, *Accepted to Nature Communications (2020)*

8. Von Gastrow, Guillaume, Jonathan Scharf, Jacob Clenney, Erick Martinez Loran, Rico Meier, Mariana I. Bertoni, and David P. Fenning. "Evaluation of Carrier Trapping in SiN_x Towards Ion Migration Measurements." In 2019 IEEE 46th Photovoltaic Specialists Conference (PVSC), pp. 2017-2020. IEEE, (2019).

ABSTRACT OF THE DISSERTATION

Detection and Visualization of Degradation Mechanisms
in Energy Generation and Storage Devices

by

Jonathan David Scharf

Doctor of Philosophy in NanoEngineering

University of California San Diego, 2021

Professor Shirley Meng, Chair

Energy generation and storage technologies must improve to address the growing energy concerns, mitigate the effects of climate change, and pave the way for emerging high-power technologies. Degradation mechanisms in silicon solar modules limit operational lifetimes and increase the levelized cost of energy of photovoltaic (PV) systems. Recent studies have linked potential-induced-degradation and sodium migration through the module stack as the main degradation mechanism. However, quantifying the rate of the sodium migration through the material layers is challenging because of the presence of electronic traps within the SiN_x antireflection coating. Through the development of a trap-corrected bias-temperature stress method, the sodium migration kinetics through the SiN_x layer are determined in this dissertation, making possible to model and extend solar module lifetimes.

Regarding energy storage, emerging technologies such as 5G, Internet of Things, and wearable electronics require safe and flexible batteries that can withstand high currents densities. While traditional Li-Ion batteries (LIBs) offer excellent energy densities, their safety and power requirements fall short. In contrast, aqueous Zn batteries offer a safe and benign chemistry and outperform LIBs at high current densities thanks to their higher electrolyte ionic mobilities. The second part of this dissertation focuses on the development of high performance flexible and printable Zn-AgO batteries for high-power electronics.

Furthermore, to extend the cycle and shelf life of these devices, a deep dive investigation of the degradation mechanisms is performed using *in-situ* X-ray Microscale Computed Tomography. Combined with detailed electrochemistry, the effects of material corrosion and parasitic reactions are quantified and visualized in 3D tomograms. From these results, the material system is optimized to extend the battery shelf life and perform >300 cycles at a high areal capacity 12.5 mAh/cm^2. In summary, this dissertation focuses on the investigation of key degradation mechanisms in PV and battery systems and the optimization to improve device lifetimes.

Chapter 1. Kinetics of Potential Induced Degradation in Silicon Solar Modules

In this chapter, a trap-corrected bias-temperature stress (TraC-BTS) method is used to quantify the kinetics of ion migration in dielectrics based on capacitance-voltage measurements. The method is based on the extraction of flatband potential (V_{fb}) shifts in metal-insulator-semiconductor test structures an enables the reliability assessment of semiconductor dielectrics and solar cells. This study shows that carrier trapping in the dielectric must be accounted for, as it strongly affects the measurement of flatband potential in silicon-nitride-based capacitors. This effect is corrected by isolating the contribution of trapping on V_{fb} using contamination-free control devices. A specific drift-diffusion model of the ion kinetics presented here allows the extraction of ion diffusivity. An Arrhenius relationship is obtained for sodium diffusivity in silicon nitride in a temperature range from 30°C to 90°C at an electric field of 1 $\mathrm{MV \cdot cm^{-1}}$, yielding a pre-factor $D_0 = 1 \times 10^{-14}\ \mathrm{cm^2 \cdot s^{-1}}$ and an activation energy $E_a = 0.14\mathrm{eV}$, with a 95% confidence interval of [0.07,0.21] eV for the diffusivity. These quantitative kinetics confirm that silicon nitride may be a poor sodium migration barrier under a significant electric field.

1.1 Introduction

The migration of mobile ionic impurities can significantly degrade the performance of semiconductor devices such as solar cells, transistors and metal-insulator-semiconductor (MIS) devices, where ions at the gate dielectric affect electrical parameters[1;2]. Ion migration can also be utilized to purposely introduce charges into a dielectric, allowing for instance the control of optoelectronic device characteristics[3]. Migration kinetics must consequently be quantified in order to rigorously control device performance.

The understanding of sodium ion kinetics in dielectrics is particularly crucial for silicon photovoltaics (PV), as it is believed to be the cause for potential-induced degradation (PID) of the shunting type[4;5], which can result in critical device failure. As solar modules operate, a potential builds up between the grounded frame and the cell, which causes migration of sodium ions eventually through the silicon nitride anti-reflection layer[6]. Evidence suggests that after long times on the order of several years, sodium can sink into the Si and shunt the junction[5;7;8]. Although nitrides like those commonly used in silicon PV have been reported qualitatively to be effective barriers against ion migration[9;10;11], high sodium diffusivities have also been reported at elevated temperature[12]. In particular, Wilson *et al.* reported sodium ionic mobilities under an electric field equivalent to diffusivities between 10^{-14} $cm^2 \cdot s^{-1}$ and 10^{-16} $cm^2 \cdot s^{-1}$ at 70-400°C in plasma-enhanced chemical vapor deposited (PECVD) SiN_x[13]. As literature reports that PID occurs after sodium migration through the SiN_x[12], sodium kinetics in silicon nitride must be known accurately at device-operating temperatures.

In the past, ionic mobilities have been extracted in SiO_2 using transient current measurements[4;14;15;16;17]. However, this method assumes that ions cross the dielectric completely over the duration of a measurement. Consequently, this technique is limited to ions of sufficiently high diffusivities in the material of interest and prohibits studies at low temperatures.[16] In contrast, in the Bias-Temperature-Stress (BTS) method,[2] capacitance-voltage (CV) measurements allow the detection of ion migration in a dielectric at any time through the measurement of flatband voltage (V_{fb}) variation caused by mobile ionic charge. This method can thus be applied to a greater variety of dielectrics in a large temperature range. Snow *et al.* first applied the technique to sodium migration in SiO_2 but did not extract a quantitative diffusivity.[18] Many other studies have applied

BTS and CV measurements of ionic migration to microelectronics, electrets, and solar cell technology.[10;11;17;19;20;21;3]

The standard BTS method however does not consider carrier trapping effects and lacks the associated modelling to quantify ion kinetics. Trapping alters flatband potential measurements in many dielectrics, including SiN_x[19;22;23] and high-*k* dielectrics such as hafnium oxide.[24] This results in incorrect attribution of flatband shifts due to conflation of carrier trapping with mobile ion kinetics, as seen for example in porous SiO_x.[20] Furthermore, oversimplification in modeling the physical processes, *e.g.* such as assuming that all mobile ions instantly reach the dielectric/silicon interface,[21] prevents reliable analysis of the migration kinetics in the dielectric. Here we present a time-resolved capacitance-voltage method which incorporates a kinetics model for extraction of ionic diffusivity in dielectrics. We apply this method to quantify sodium diffusivity in silicon nitride. These sodium ion kinetics advance understanding of ion distribution transients in semiconductor dielectrics and should aid the design of dielectric materials to mitigate potential-induced degradation mechanisms in PV devices.

1.2 Flatband fitting Method

In the BTS method, ion movement is facilitated by stressing the dielectric with an electric potential V_{stress} and heating the layer above room temperature conditions. Detection of ion migration using CV measurements is based on Eqn. (1), which relates a shift in the flatband voltage ΔV_{FB} to the time dependent concentration profile of mobile ionic and electronic charges present in the dielectric layer:[25]

$$\Delta V_{\mathrm{FB}} = -\frac{q_e z_i}{\varepsilon_{\mathrm{ins}}}\int_0^L xC(x,t)dx - \frac{q_e z_{\mathrm{t}}}{\varepsilon_{\mathrm{ins}}}\int_0^L xn_{\mathrm{t}}(x,t)dx, \tag{1}$$

where q_e is the elementary charge, z_i and z_{t} are the valences of the mobile ions and traps, respectively (for Na^+, $z_i = +1$ and $z_{\mathrm{t}} = \pm 1$, depending on the type of the carrier captured in the trap), $\varepsilon_{\mathrm{ins}}$ is the relative permittivity of the dielectric, C and n_{t} are the concentrations of mobile ions and occupied traps, respectively, and x is the depth in the dielectric from the gate ($x = 0$) to the semiconductor ($x = L$). The flatband shift ΔV_{FB} depends on stress time t, temperature, T, and V_{stress}. It is obtained by subtracting the initial V_{FB} of a device prior to stressing from the V_{FB} measurement at time t, eliminating the dependence on work functions and on fixed charges in the dielectric that do not change with time. We isolate the ionic contribution to the flatband voltage shift $\Delta V_{\mathrm{FB}}^{\mathrm{ion}}$ by subtracting the component due to electronic trapping $\Delta V_{\mathrm{FB}}^{\mathrm{traps}}$, measured in devices without intentional ion contamination, *i.e.* $C = 0$ in Eqn. (1), from the total ΔV_{FB} found in ion-contaminated devices:

$$\Delta V_{\mathrm{FB}}^{\mathrm{ion}} = \Delta V_{\mathrm{FB}} - \Delta V_{\mathrm{FB}}^{\mathrm{traps}} \tag{2}$$

Using this trap-corrected BTS (TraC-BTS) equation, we can directly relate the ion concentration to the flatband shift. The mobile ion concentration in the dielectric is given by the solution to the Nernst-Planck equation,

$$\frac{\partial}{\partial t}C\left(x,t\right) = -\nabla \cdot \left[-D\nabla C - \frac{Dz_i q_e}{k_{\mathrm{B}}T}C\nabla\phi\right] \tag{3}$$

where D is the diffusivity of mobile ions in the dielectric, k_B is Boltzmann's constant, φ is the electric potential and T is the absolute temperature. By fitting the measured $\Delta V_{\mathrm{FB}}^{\mathrm{ion}}$ as a function of time across a range of temperatures, an Arrhenius behavior of the mobile ion diffusivity can be observed.

In our analysis, we make the simplifying assumption of a constant electric field $E = V_{\mathrm{stress}}/L$ within the nitride, as we operate in the limit of a low concentration of ionic charge in the dielectric relative to the effective charge from the external potential V_{stress}. This assumption can be written as a condition on the sodium concentration C in the film, obtained from Poisson's equation in the case of constant-source diffusion,

$$C \ll 2\varepsilon_{\mathrm{ins}} V_{\mathrm{stress}}/(q_e L^2) \tag{4}$$

with L the thickness of SiN_x and V_{stress} the applied potential as indicated above. X-ray photoelectron spectroscopy with a 0.1 % sensitivity limit was unable to detect sodium ions in the films used here. This was confirmed by negative SIMS results with a detection limit of 5×10^{18} cm^{-3}. For an 86 nm thick device stressed at 8.6 V (1 MV/cm), and a $\epsilon_r \approx 7$, the right hand side of Eqn. (4) rounds to $\approx 10^{18}$ cm^{-3}, indicating that, indeed, C is low compared to V_{stress}. This allows us to introduce the constant drift velocity $v_d = -\mu(\nabla\varphi)_x = z_i q_e DE/k_B T$. Eqn. (3) can then be transformed into the diffusion equation by introducing the change of variables:[26] $\tilde{x} = x - v_d t$.

We assume a constant source of sodium ions at the surface, C_s, and a zero-flux boundary at the silicon interface. Given these boundary conditions, we can write an analytical solution for Eqn. (3) at short times ($t < \tau_c$, discussed below):

$$C(x,t) = \frac{C_s}{2B}\left[\operatorname{erfc}\left(\frac{x-\mu E t}{2\sqrt{Dt}}\right) + \operatorname{erfc}\left(-\frac{x-2L+\mu E t}{2\sqrt{Dt}}\right)\right] \tag{5}$$

with a normalization constant $B = \mathrm{erfc}(-\mu E t/(2\sqrt{Dt})$. To extract the ionic diffusivity D and surface ion concentration C_s from the experimental flatband shift, we fit the theoretical flatband shift obtained by combining Eqns. (1) and (5) to the experimental flatband shift obtained from Eqn. (2). The fitting is performed using non-linear least-squares and the uncertainty of the fitted parameters is taken as the 95% confidence intervals estimated from the covariance matrix of the fit using the t-student distribution.

1.3 Experimental Details

To demonstrate the TraC-BTS method and quantify sodium ion kinetics in SiN_x we fabricated metal-insulator-semiconductor (MIS) structures on *n*-type silicon (100) wafers with a resistivity of $2.7\Omega \cdot$ cm. The wafers were cleaned with acetone, ethanol and isopropyl alcohol and then cleaned with the RCAI and RCAII procedures followed by a 1% hydrofluoric acid dip. The SiN_x films were grown on the polished side of the wafer by plasma-enhanced chemical vapor deposition (PECVD) using a NH_3/SiH_4 ratio of 7. **This ratio was chosen to obtain a high SiN_x resistivity[27], which ensures that a significant potential spans across the silicon nitride to maintain a reasonable timescale in the experiments.** Additionally, capacitors were made with SiO_2 films grown by dry oxidation at a temperature of 1100°C. The thickness and refractive index of the as-deposited film were mapped using spectroscopic ellipsometry. An average thickness of 86 nm and a refractive index of 1.89 at 600 nm were estimated for the silicon nitride. The dielectric layers were then cleaned with isopropyl alcohol and ethanol to remove surface contaminants and the back surface was swabbed with hydrofluoric acid. Approximately 200 nm of aluminum were deposited by thermal evaporation onto SiN_x to act as a gate electrode. The electrodes were defined by a shadow mask with 1mm diameter circles and a pitch of 2.54 mm. A layer of aluminum was evaporated on the bottom side of the wafer to produce the back contact. In devices with intentional sodium contamination, 25 nm of sodium chloride were thermally evaporated at 800°C onto the surface of SiN_x and metal evaporation followed without breaking vacuum.

In order to perform *in-situ* migration studies, we developed an *in-situ* CV setup with automated BTS capabilities. The system applies a temperature and voltage stress to the MIS capacitors in 1- or 4-hour time increments using a programmable hotplate to heat the devices and a Keithley 2401 sourcemeter to apply a DC bias. It has been reported that an electric field close to 1 $MV \cdot cm^{-1}$ across SiN_x is necessary to observe the PID effect in silicon PV modules, while a voltage divider model for the potential drop across the nitride layer in an operating module predicts a value several orders of magnitude lower. The reason for this discrepancy is unknown[28]. This value of +1 $MV \cdot cm^{-1}$ is consistent with our model as it satisfies equation 4, and this field was thus applied to the MIS devices during sodium migration experiments, in agreement with other studies[13]. After each time increment, a fan cools the devices to room temperature within 15 minutes. Once cooled, CV curves are acquired with a HP4194A impedance analyzer at 1 MHz, to ensure that sodium ions are unaffected by the 100 mV (peak to peak) AC signal. The DC voltage is swept from -8.6 V to +8.6 V and each measurement is averaged 32 times with a dwell time of 5 ms per point. The flatband voltage as a function of BTS time is then extracted from the CV curves using the second-derivative technique[29].

1.4 Results and discussion

Figure 1.1a illustrates how the trapping correction method is necessary to obtain a ΔV_{FB} signal truly representing sodium migration in silicon nitride. The flatband shift in a sodium-free SiN_x capacitor increases as a function of time, which is explained by an increase of negative charge in the dielectric according to Eqn. (1). This originates from substantial electron trapping, as demonstrated in our previous study.[23] Electron trapping can be modelled by first-order kinetics[30] and the corresponding fit is shown as a dashed line, with an extracted trapping time-constant of 2.5 hours. Given that each CV sweep is completed in 2 minutes, we do not expect the DC bias from the CV measurement itself to influence the flatband shift. The raw flatband signal (before trapping correction) in a sodium-contaminated sample, displayed as solid circles in **Figure 1.1a**, includes contributions from electron trapping (negative charging) and sodium migration (positive charging). To account for charge trapping in SiN_x,[19;22;23] we used the ΔV_{FB}^{traps} averaged from four sodium-free devices as the baseline to correct the flatband shift of sodium-contaminated devices according to Eqn. (2). After trapping correction, a negative flatband shift is observed as a function of time. This is the trend expected from the ingress of positive ions into the dielectric, and is well fit by our ion migration model, depicted by the solid lines. Additionally, the increase in flatband shift magnitude with temperature reflects an increase of sodium solubility in silicon nitride. Note that the error bars originate from the variability in the concentration of trapped charged in sodium-free samples used for the baseline. Overall, our TraC-BTS data captures the resulting flatband shift in sodium-contaminated devices across device-relevant temperatures.

To confirm the applicability of the TraC-BTS method for isolating ion migration, additional experiments were performed on thermal silicon oxide capacitors, which are known to exhibit very little to no carrier trapping in the bulk of the dielectric compared to silicon nitride[19;31]. **Figure 1.1b** displays flatband shift measurements in sodium-free and in sodium-contaminated SiO_2 capacitors.

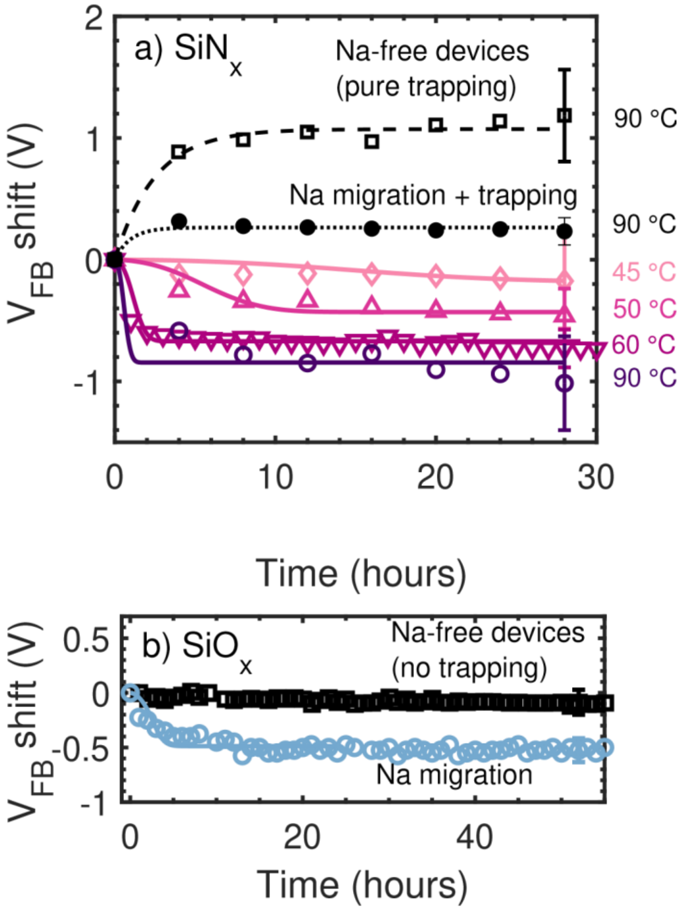

Figure 1.1 | Flatband shift as a function of time and temperature. a) in SiNx capacitors stressed at 1 MV·cm−1. An example of flatband shift solely caused by trapping in Na-free capacitors is shown. The dashed line is a fit with a first-order-kinetics trapping model. An example of raw flatband shift including both Na migration and trapping is shown with a dotted line as a guide to the eye. Flatband shifts in Na-contaminated devices are shown at different temperatures after trapping correction. The fits obtained from the Nernst-Planck ion migration model are depicted by solid lines. b) in SiO2 capacitors without trapping correction (pure ionic shift) in both Na-free and Na-contaminated devices at 0.5 MV·cm−1 and 50°C.

As expected, little to no variation of flatband voltage can be observed in control samples without intentional sodium contamination. In sodium-contaminated SiO_2 capacitors, a flatband shift of approximately -0.5 V is detected without the need for trapping correction. It is also well fit by our ion migration model. Consequently, these results in SiO_2 confirm that our experimental conditions and detection method allow migration of sodium as well as its detection. Overall, these data in SiN_x and SiO_2 indicate that the TraC-BTS method allows the detection of ion migration even in the presence of carrier trapping.

Using the TraC-BTS method, an Arrhenius relationship for sodium ion migration in SiN_x was established by averaging the diffusivities measured in 4-8 devices at each temperature. **Figure 1.2** shows the extracted diffusivities with 95 % confidence intervals.

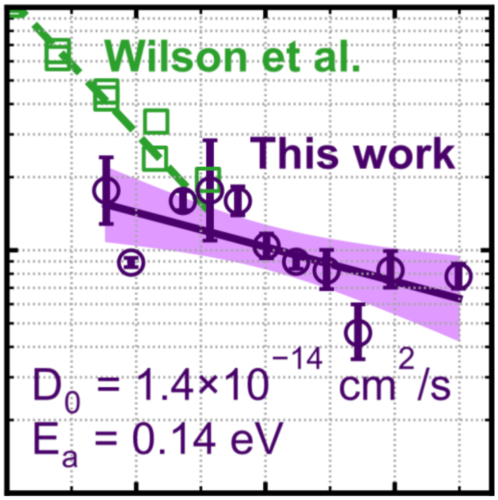

Figure 1.2 | Sodium ion diffusivity in SiNx evaluated by the TraC-BTS method and by Wilson et al.13 using a Kelvin-probe based method. The estimated prefactor for the diffusion coefficient is D0 =1.4 · 10−14 cm2 · s−1 with a 95% confidence interval of [1.2 × 10−15,1.6 × 10−13] cm2 · s−1. The estimated activation energy is Ea = 0.14 eV, with a 95% confidence interval of [0.07,0.21] eV.

Our fit results in a diffusion coefficient pre-factor $D_0 = 1.4 \times 10^{-14}$ cm^2 s^{-1} with a 95 % confidence interval of [1.2×10^{-15},1.6×10^{-13}] cm$^2 \cdot$ s^{-1} and in an activation energy E_a = 0.14eV, with a 95 % confidence interval of [0.07,0.21] eV. The error bars reflect uncertainty due to device-to-device variation and to the variation in electron trapping in the clean devices used for baseline correction. Note that a deviation from the higher-temperature results of Wilson *et al.*[13] is seen due to a large difference of measured activation energy.

To interpret the above results in the context of sodium ion migration in SiNx and PID, we examine how the sodium concentration at the SiNx/silicon interface changes over time. Sodium impurities can act as a source for eventual PID of the shunting type. We consider the characteristic transit time of sodium ions across the dielectric, τ_c, as the solution to the equation $L = 2\sqrt{D\tau_c} + \mu E\tau_c$.

Figure 1.3 shows the characteristic transit time across a typical nitride thickness of 65 nm as a function of temperature and electric field across the nitride in ranges relevant to solar module operation. In these conditions, sodium migration through the nitride bulk can occur relatively quickly, between a few hours and a month depending on the potential drop across the nitride. These times are lower than the observed degradation times after accelerated experiments at high temperature and in the field.[32;33] The characteristic time, however, only reflects transport across the SiN_x and does not represent the actual time to potential-induced degradation in the full device stack. Instead, it illustrates the extent to which temperature and module bias affect PV device reliability.

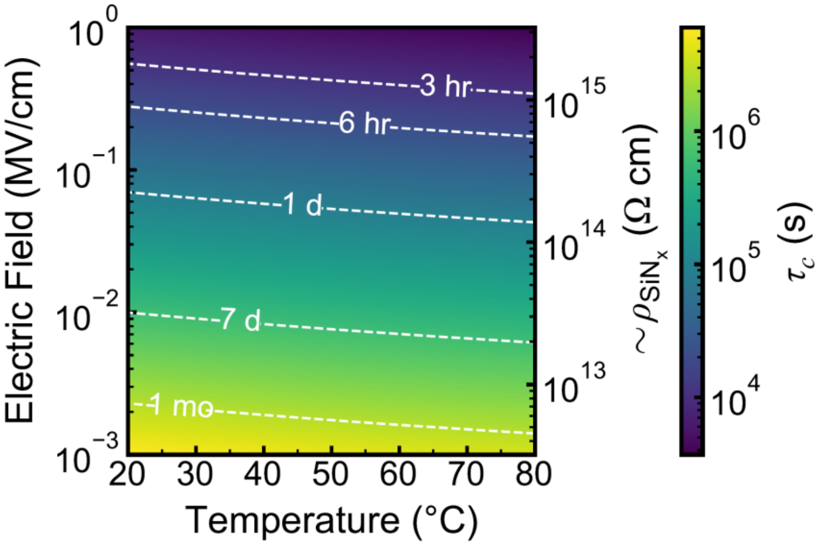

Figure 1.3 | Characteristic sodium transit time in a 65 nm-thick SiNx film as a function of solar module temperature and of the electric field across the dielectric.

The electric field across the SiN_x in a Si PV module is highly dependent on the resistivities of the other module materials, which vary widely.[8;34;35] We use a voltage divider model[36] with a borosilicate glass of resistivity $\rho_{\text{glass}} \approx 3 \times 10^{12}\ \Omega \cdot \text{cm}$,[37] EVA with resistivity $\rho_{\text{EVA}} \approx 5 \times 10^{13}\ \Omega \cdot \text{cm}$, and a voltage differential of +1000V to estimate the nitride resistivity corresponding to the electric field on the left axis. Based on this voltage divider model, the electric field across SiN_x in an operational module would typically range from a few $\text{kV} \cdot \text{cm}^{-1}$,[8] to tens of $\text{kV} \cdot \text{cm}^{-1}$.[34] The range is extended to 1 $\text{MV} \cdot \text{cm}^{-1}$ in **Figure 1.3** for consistency with our experimental conditions.

It is worth considering scenarios in which the assumptions involved in deriving the analytical solution used here no longer hold, namely: (1) Large ion concentrations: $C_s \approx 2\varepsilon_{\text{ins}} V_{\text{stress}}/(q_e L^2)$, where the distribution of mobile ions affects the local potential within the dielectric (2) long stress times: $t > \tau_c$, where the flatband potential becomes sensitive to the accumulation of ions at the dielectric-semiconductor interface or the leaking of ions across it, and (3) source-limited mobile ion migration. In a future work, numerical solution of the Nernst-Planck equation (Eq. (3)) will enable the application of the TraC-BTS method to extract mobile ion kinetics whenever the above assumptions break down, allowing for quantification of kinetics under a broad range of possible experimental test conditions and material systems.

1.5 Conclusion

In conclusion, we quantified sodium ion diffusion kinetics in silicon nitride using a drift-diffusion model to analyze experimental flatband voltage shifts. We developed a capacitance-voltage setup for measurement of capacitors under bias-temperature-stress. Quantification of ion kinetics required correction of non-idealities from charge trapping in the dielectric. This description of a capacitance-voltage-based approach to parameterize ion migration should allow reliable quantification of ion diffusion kinetics broadly in dielectrics. Capacitance-voltage instrumentation is widely available and device preparation is straightforward, which makes this method a promising approach for quantification of ionic migration in many materials and devices. We also presented an analytical solution specific to the bounds of our experiment that describes the migration of sodium through SiN_x. We showed that sodium migration through a PV-relevant, 65 nm-thick SiN_x layer can occur within a few days in field operating conditions. Next, we will extend this study to a variety of SiN_x films with different compositions and electrical properties. Evaluating sodium ion kinetics in SiN_x paves the way for the quantification and mitigation of the role of sodium in potential-induced degradation in silicon photovoltaics.

1.6 Acknowledgements

G.v.G., E.M-L, and J.S. contributed equally to this work. This work was supported by the U.S. Department of Energy's Office of Energy Efficiency and Renewable Energy under Solar Energy Technologies Office Agreement Number DE-EE0007751. The authors thank Stephanie Moffitt for helpful discussion and XPS measurements. E.M.-L. thanks CONACyT and UC MEXUS for his doctoral fellowship.

1.7 References

1. E. S. Schlegel, R. S. Keen, G. L. Schnable, In IEEE, editor, 8th Reliability Physics Symposium.IEEE, ISBN 0735-0791, 1970 9–16.
2. D. K. Schroder, Semiconductor material and device characterization, John Wiley & Sons, 2015.
3. R. S. Bonilla, P. R. Wilshaw, J. Phys. D: Appl. Phys. 2017, 51, 2 025101.
4. J. P. Stagg, Appl. Phys. Lett. 1977, 31, 8 532.
5. S. P. Harvey, J. A. Aguiar, P. Hacke, H. Guthrey, S. Johnston, M. Al-Jassim, IEEE J. Photovolt.2016, 6, 6 1440.
6. W. Luo, Y. S. Khoo, P. Hacke, V. Naumann, D. Lausch, S. P. Harvey, J. P. Singh, J. Chai, Y. Wang, A. G. Aberle, Energy Environ. Sci. 2017, 10, 1 43.
7. D. Lausch, V. Naumann, O. Breitenstein, J. Bauer, A. Graff, J. Bagdahn, C. Hagendorf, IEEE J.Photovolt. 2014, 4, 3 834.
8. V. Naumann, D. Lausch, A. H¨ahnel, J. Bauer, O. Breitenstein, A. Graff, M. Werner, S. Swatek, S. Großer, J. Bagdahn, Sol. Energy Mater. Sol. Cells 2014, 120 383.
9. J. V. Dalton, J. Drobek, J. Electrochem. Soc. 1968, 115, 8 865.
10. B. Yurash, B. E. Deal, J. Electrochem. Soc. 1968, 115, 11 1191.
11. T. E. Burgess, J. C. Baum, F. M. Fowkes, R. Holmstrom, G. A. Shirn, J. Electrochem. Soc. 1969,116, 7 1005.
12. J. W. Osenbach, S. S. Voris, J. Appl. Phys. 1988, 63, 9 4494.
13. M. Wilson, A. Savtchouk, P. Edelman, D. Marinskiy, J. Lagowski, Sol. Energy Mater. Sol. Cells2015, 142 102.
14. P. Kohn, K. Schro¨ter, T. Thurn-Albrecht, Phys. Rev. Lett. 2007, 99, 8 086104.
15. R. J. Kriegler, T. F. Devenyi, Thin Solid Films 1976, 36, 2 435.
16. G. Greeuw, J. F. Verwey, J. Appl. Phys. 1984, 56, 8 2218.
17. E. Yon, W. H. Ko, A. B. Kuper, IEEE Trans. Electron Devices 1966, ED-13, 2 276.
18. E. H. Snow, A. S. Grove, B. E. Deal, C. T. Sah, J. Appl. Phys. 1965, 36, 5 1664.
19. B. E. Deal, P. J. Fleming, P. L. Castro, J. Electrochem. Soc. 1968, 115, 3 300.
20. F. Lanckmans, K. Maex, Microelectron. Eng. 2002, 60, 1-2 125.

21. A. L. S. Loke, C. Ryu, C. P. Yue, J. S. H. Cho, S. S. Wong, IEEE Electron Device Lett. 1996, 17,12 549.

22. K. J. Weber, H. Jin, Appl. Phys. Lett. 2009, 94, 6 063509.

23. G. von Gastrow, J. Scharf, J. Clenney, E. Martinez Loran, R. Meier, M. I. Bertoni, D. P. Fenning,In IEEE Photovoltaic Specialists Conference. IEEE, 2019 2017–2020.

24. D. A. Buchanan, D. Felnhofer, In Defects in High-k Gate Dielectric Stacks. Springer Netherlands,ISBN 978-1-4020-4367-3, 2006 41–59.

25. E. H. Nicollian, J. R. Brews, MOS/metal oxide semiconductor/physics and technology, Wiley, 1982.

26. R. Balluffi, S. Allen, C. w. Carter, Kinetics of materials, Wiley, 2009.

27. D. J. DiMaria, in Proceedings ofthe International Topical Conference on the Physics ofSiO2 and Its Interfaces (Ed: S. T. Pantelides). Elsevier, IBM Thomas J. Waston Research Center, Yorktown Heights, New York, 1978 pp. 160–178.

28. T. L. Chu, J. R. Szedon, C. H. Lee, Solid-State Electron. 1967, 10, p. 897.

29. P. Hacke, R. Smith, K. Terwilliger, S. Glick, D. Jordan, S. Johnston, M. Kempe, S. Kurtz, In 2012 IEEE 38th Photovoltaic Specialists Conference (PVSC) PART 2. IEEE, ISBN 146732888X, 20121–8.

30. P. Hacke, S. Spataru, K. Terwilliger, G. Perrin, S. Glick, S. Kurtz, J. Wohlgemuth, IEEE J. Photovolt. 2015, 5, 6 1549.

31. G. J. M. Janssen, M. K. Stodolny, B. B. Van Aken, J. L¨offler, M. W. P. E. Lamers, K. J. J. Tool, I. G. Romijn, IEEE J. Photovolt. 2019, 9, 3 608.

32. H. Nagel, M. Glatthaar, S. W. Glunz, In 31st European PV Solar Energy Conference and Exhibition. 2015 1825–1829.

33. V. Naumann, K. Ilse, C. Hagendorf, In Proceedings of 28th European Photovoltaic Solar EnergyConference and Exhibition, Paris, France. 2013 2994–2997.

34. W. D. Kingery, H. K. Bowen, R. Uhlmann Donald, Introduction to Ceramics, 2nd Edition, journal article 10, 449–468, Wiley, 1976.

35. A. Piccirillo, A. Gobbi, Journal of The Electrochemical Society 1990, 137, 12 3910.

36. M. Jungha¨nel, A. Kux, M. Sch¨adel, M. Scherff, Solar cell, solar cell manufacturing method and testing method, 2011.

37. R. Winter, J. Ahn, P. C. McIntyre, M. Eizenberg, Journal of Vacuum Science & Technology B 2013, 31, 3 030604.

Chapter 2. High Performance Printable and Flexible Zn-AgO Batteries

The rise of flexible electronics calls for cost-effective and scalable batteries with good mechanical and electrochemical performance. In this work, we developed printable, polymer-based AgO-Zn batteries that feature flexibility, rechargeability, high areal-capacity, and low impedance. Using elastomeric substrate and binders, the current collectors, electrodes, and separators can be fabricated via high-throughput, scalable, layer-by-layer screen-printing process and vacuum-sealed in a stacked configuration. The batteries are customizable in sizes and capacities, with the highest obtained areal capacity of 54 mAh/cm^2 for primary applications. Advanced X-ray tomography and impedance spectroscopy were used to characterize the battery, whose mechanical stability was tested with rigorous deformation tests. The all-printed batteries were used to power a flexible E-ink display system that requires a high-current drain and exhibited superior performance than commercial lithium coin-cell batteries under the same pulsed-discharge conditions. The developed battery presents a practical solution for powering a wide range of electronics and holds major implications for the future development of practical and high-performance flexible batteries.

2.1 Introduction

Recent interest in multifunctional flexible electronics for applications in sensing, displays, and wireless communication advocates for the development of complementary flexible energy storage solutions.[1,2] Accordingly, numerous efforts have been made to tackle the challenges of fabricating batteries with robust mechanical resiliency and high electrochemical performance. To do so, several studies focused on adapting novel battery fabrication techniques, such as substrate pre-stretching, textile-embedding, and “island-bridge”, wire/cable, kirigami, and origami structuring to endow structural flexibility and stretchability to batteries.[3–9] Others studies focused on tackling the challenge by the means of material innovation, developing polymer-based current collectors, electrodes, separators, and electrolytes for various intrinsically flexible and stretchable batteries.[10–17] However, due to the exponential growth in the wearable flexible electronics market, manufacturers started to realize the urgent need for scalable, low-cost, and high-performance flexible battery technologies to provide practical energy storage solutions for the tens of millions of devices produced every year. Many flexible batteries rely on fabrication processes that are complex, low throughput, and high cost, and thus have limited practicality which hinders their lab-to-market transformation. Addressing the need for flexibility and scalability while maintaining low cost, printed high-performance batteries are crucial for realizing most of the commercially viable battery technology. Using low-cost thick-film fabrication technologies, flexible battery components can be printed sheet-to-sheet or roll-to-roll using traditional, low-maintenance screen printing or doctor blade casting equipment, thus realizing low-cost mass production of flexible batteries.[18]

Among many commercialized printed flexible batteries, aqueous zinc (Zn)-based conversion cells were successful in developing products with high throughput and low production cost.[19] The Zn anode chemistry has been of special interest for the flexible battery market due to its low material cost, high theoretical capacity (820 mAh/g, 5854 mAh/L), good rechargeability, and safe chemistry.[20,21] In addition, as Zn and the aqueous electrolyte can be readily handled in an ambient environment, the equipment and production costs of Zn-based batteries are often considerably lower compared to lithium-ion batteries. However, commercial Zn-based printed flexible batteries are usually non-rechargeable and feature low capacity and high impedance, thus limiting their application in low-power, disposable electronics only. Addressing these limitations, several studies have reported the development of printable, rechargeable, and high-performance Zn-based batteries.[16,22,23] Among them, the silver oxide-zinc (Ag_2O-Zn) battery has attracted particular attention due to its rechargeable chemistry and its tolerance to high-current discharge.[24,25] The redox reaction relies on the dissolution of zinc ions (Zn^{2+}) and silver ions (Ag^+) in the alkaline electrolyte and their supersaturation-induced precipitation, which takes place rapidly while maintaining a stable voltage at 1.56 V (Equation 1-6). [26,27] All E° potentials are indicated using the standard hydrogen electrode (SHE) as a reference.

Anode:

$$\text{(Dissolution)} \quad Zn\ (s) + 4OH^-\ (aq) \leftrightarrow Zn(OH)_4^{2-}\ (aq) + 2e^- \tag{1}$$

$$\text{(Relaxation)} \quad Zn(OH)_4^{2-}(aq) \leftrightarrow ZnO\ (s) + H_2O\ +\ 2OH^-\ (aq) \tag{2}$$

$$\text{(Overall)} \quad Zn\ (s) + 2OH^-\ (aq) \leftrightarrow ZnO + H_2O + 2e^- \qquad \mathrm{E^o} = -1.22\ \mathrm{V\ vs.\ SHE} \tag{3}$$

Cathode:

$$\text{(Dissolution)} \quad Ag + OH^- \leftrightarrow AgOH(aq) + e^- \tag{4}$$

$$\text{(Relaxation)} \quad 2AgOH(aq) \leftrightarrow Ag_2O(s) +\ H_2O \tag{5}$$

$$\text{(Overall)} \quad Ag_2O(s) +\ H_2O + 2e^- \leftrightarrow 2Ag(s) + 2OH^-(aq) \qquad \mathrm{E^o} = +0.34\ \mathrm{V\ vs.\ SHE} \tag{6}$$

Most of these batteries rely solely on the use of the lower oxidation state of silver to obtain reversible redox reaction, while the higher oxidation state (AgO), with its redox reaction described in Equation 7, has been rarely utilized.

$$2AgO\ (s) + H_2O\ + 2e^- \leftrightarrow Ag_2O\ (s) +\ H_2O\ (l) \qquad \mathrm{E^o} = +0.60\ \mathrm{V\ vs.\ SHE} \tag{7}$$

The underutilization of AgO can be attributed to its instability, namely, its lattice phase change when transitioning into Ag_2O, which may result in irreversible shape changes that impede rechargeability, and its high charging potential responsible of possible electrode gassing due to oxygen evolution reaction.[8,28–31] However, once addressing these issues, it is possible to access a much higher theoretical cathode capacity (from 231 mAh/g for Ag_2O to 432 mAh/g for AgO). So far, printed silver-zinc batteries reported in the literature still have low rechargeability (< 50 cycles), limited capacity (< 12 mAh/cm^2 for primary cell, < 3 mAh/cm^2 for secondary cell), along with high internal resistance ($\sim 10^2\ \Omega$) that results in large voltage drop during operation.[10,29,32–34] Such limitations are hindering the adaptation of silver-zinc printed batteries in flexible electronics.

Herein, we present a novel fabrication process of all-printed, flexible, and rechargeable AgO-Zn batteries with ultra-high areal capacity, low impedance, and good rechargeability as a practical energy storage solution for flexible electronics. The fabrication of the cell relies on low-cost, high-throughput, layer-by-layer printing of formulated powder-elastomer composite inks to form the current collectors, Zn anode, AgO cathode, and their corresponding separators. The battery adopts a low-footprint stacked configuration, with potassium hydroxide (KOH) - poly(vinyl alcohol) (PVA) hydrogel as a low impedance electrolyte sandwiched between the two fully printed electrodes. Using the thermoplastic styrene-ethyl-butylene-styrene block copolymer (SEBS) elastomer-based substrate, the assembled battery can be directly heat- and vacuum-sealed to preserve the electrolyte and ensure appropriate cell pressure during operation. This fabrication and assembly process can be applied to different cell sizes with adjustable areal capacity, allowing customizable battery form factors that are tailored for specific applications. Fully utilizing the higher oxidation state of the AgO, the as-printed cells were able to reach a high areal capacity of > 54 mAh/cm^2 while maintaining a low internal resistance ($\sim 10\ \Omega$) for primary applications.

Furthermore, utilizing an optimized cycling profile, the printed cells were recharged for over 80 cycles, sustaining 0.2 C – 1 C discharges without exhibiting significant capacity loss, while maintaining low impedance throughout each cycle. Moreover, the fabricated cells displayed outstanding robustness against repeated bending and twisting deformations. To demonstrate their performance in powering typical flexible electronics, the fabricated batteries were successfully implemented in a flexible E-ink display system with an integrated microcontroller unit (MCU) and Bluetooth modules that require pulsed high-current discharge. Leveraging a low-cost scalable production process, polymer-based flexible architecture, and customized ink formulations, the all-printed AgO-Zn battery, with its desirable mechanical and electrochemical performance, presents a practical solution for powering the next-generation flexible electronics, and sets a new benchmark for the further development of printable flexible batteries.

2.2 Results

2.2.1 All-printed Polymer-based Fabrication

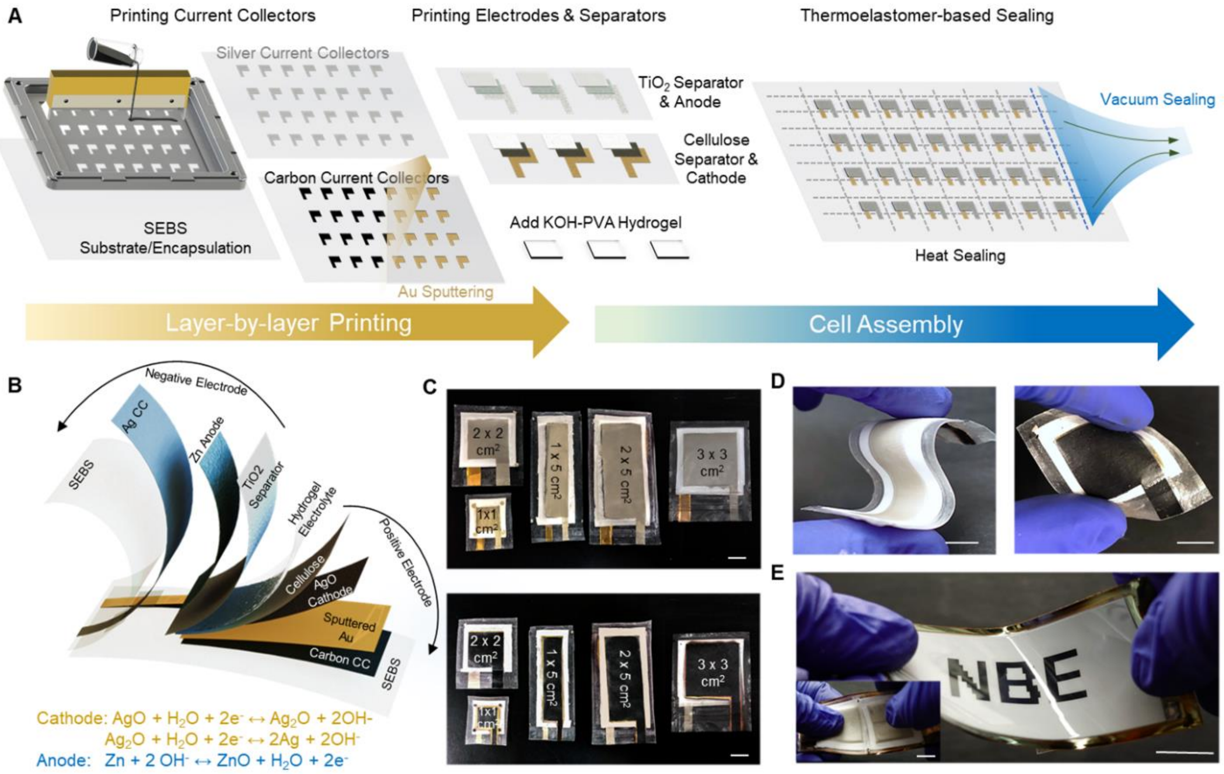

Figure 2.1 | All-printed fabrication of the flexible, rechargeable, and high-capacity AgO-Zn battery. (a) Illustration of the layer-by-layer printing and vacuum sealing assembly processes. (b) Illustration of the AgO-Zn battery cell structure. The cell is composed of a hydrogel electrolyte sandwiched between the 2 electrodes, with each side composed of a heat-sealable SEBS substrate, current collectors, active material electrodes, and corresponding separators. (c) Photo images of the assembled cells in different customized sizes. (d) Photo images demonstrating the flexibility of the printed batteries. (e) Photo images of a flexible E-ink display system powered by the flexible AgO-Zn batteries. Scale bar, 1 cm.

The all-printed fabrication of the flexible AgO-Zn battery was designed based on the careful selection of elastomers for the substrate, sealing, and ink binders based on their mechanical properties, chemical stabilities, and processabilities. SEBS was selected as the substrate material for its good solvent processability, chemical stability under high pH, outstanding elasticity, as well as its appropriate melting point (~200 °C), allowing it to be easily cast into films that are chemically stable, flexible, and heat-sealable to support and seal the battery.[35] Screen-printing, a low-cost high-throughput thick-film technique was used for ink deposition, as it allows the efficient fabrication of the current collectors, electrodes, and separators into their preferred shapes and thicknesses.[18] The screen-printing of the batteries relies on the customized formulation of 6 inks corresponding to the current collectors, electrodes, and the separators for both the anode and cathode. Conductive and flexible silver ink and carbon ink were printed as the anode and cathode current collectors respectively. Both inks use SEBS as the elastomer binder and toluene as the solvent to allow the ink to firmly bond to the toluene-soluble SEBS substrate. The anode ink was composed of Zn particles with bismuth oxide (Bi_2O_3) as an additive to reduce dendrite formation and suppress H_2 gassing, while the cathode ink was mainly composed of AgO powder with a small amount of lead oxide coating to enhance the electrochemical stability and carbon black added to enhance the electronic conductivity of the electrode.[29] A high-pH stable, elastomeric fluorocopolymer was used as the binder for both electrodes for its solubility in lower ketones which is less prone to oxidation by the highly oxidative AgO. Cellulose powder was used to form the porous cathode separator that mimics the use of cellophane to capture and reduce dissolved silver ions and prevent material crossover.[8,19] A titanium dioxide (TiO_2)-based ink was formulated for the anode separator, acting as a physical barrier to Zn dendrite growth. The inclusion of TiO_2 also aids the recrystallization of zincate, hence preventing the Zn from traveling towards the cathode. Lastly, a solid-phase polyvinyl alcohol (PVA) hydrogel crosslinked with potassium hydroxide (KOH) was prepared as the electrolyte, which complements the cell flexibility without the risk of leaking. Lithium hydroxide (LiOH) and calcium hydroxide ($Ca(OH)_2$) were used as additives in the electrolyte to maintain electrolyte chemical stability and minimize Zn dissolution, which in turn prevent the uncontrolled recrystallization of Zn during charging that leads to dendrite growth.[36,37]

The fabrication of the batteries begins with the preparation of the substrates, where a resin of SEBS dissolved in toluene was cast onto wax papers using film casters and dried in the oven to form a transparent elastic film. The layer-by-layer printing process is illustrated in **Figure 2.1a**. Firstly, the Ag and the carbon inks were printed onto the SEBS substrate as current collectors, with a 400 nm layer of gold sputtered onto the carbon current collectors to enhance their conductivity and chemical stability. Then, the Zn and the TiO_2 inks, and the AgO and the cellulose inks were printed onto their corresponding current collectors. To complete the cells, the KOH-PVA hydrogel electrolyte was cut to size and sandwiched between the two electrodes. Lastly, the sheet of batteries was heat and vacuum sealed and separated into individual cells, finalizing the scalable sheet-by-sheet fabrication of multiple cells in one sitting. The flexible, vacuum-sealed AgO-Zn batteries comprised of 9 layers of composite materials, can thus be easily fabricated using layer-by-layer screen-printing (**Figure 2.1b**). The major advantage of the stencil printing technique is the customizable dimension of the cells that can be tailored for different applications with specific form factor and capacity requirements. As examples, cells in different sizes were fabricated using the same fabrication process (**Figure 2.1c**), and could be integrated with different sizes of flexible electronic devices. Regardless of the shapes and sizes, the assembled cells are highly flexible and durable under repeated mechanical deformations (**Figure 2.1d**), making them highly suitable for powering wearable and flexible electronics that require high resiliency to various deformations. Furthermore, the superior electrochemical performance of the fabricated AgO-Zn battery greatly expands the application of flexible printed batteries in electronics with high power demands. This capability was demonstrated by powering a flexible display system with microcontroller and Bluetooth modules (**Figure 2.1E**), as discussed in the later section.

2.2.2 Microstructural and Electrochemical Characterization

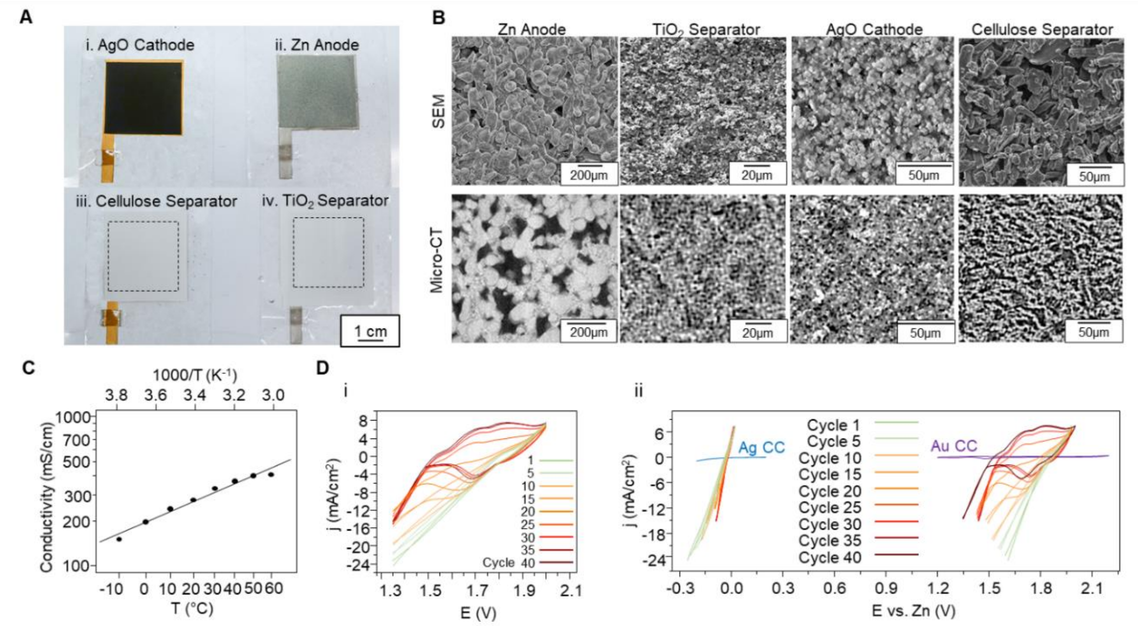

Figure 2.2 | Morphological and electrochemical characterization of the printed battery. (A) Photo images of the printed 3 × 3 cm2 cell with the (i) AgO electrode, (ii) Zn electrode, (iii) Cellulose separator, and (iv) TiO2 separator layers. (B) Microscopic images of corresponding layers of the cell taken via SEM and Micro-CT. (C) The conductivity of the gel electrolyte as a function of temperature. (D) 40 cycles of CV between 2 V and 1.35 V of the (i) full cell and (ii) corresponding potential shifts in the anode (left) and the cathode (right) using a 3-electrode cell with a Zn metal pseudo-reference electrode. The CVs of the current collectors within the corresponding voltage windows (anode -0.3 V – 0.3 V, cathode 1.2 V – 2.2 V) under the electrolyte environment are overlaid onto the electrode CVs. Scan rate: 10 mV/s.

The printed electrodes and separators (**Figure 2.2a**) were characterized by scanning electron microscopy (SEM), as well as non-intrusive, *in-situ* micrometer-scale X-ray computed tomography (micro-CT). The introduction of micro-CT enables the capability of non-destructive inspection of the battery, which can be highly beneficial to characterize the devices under deformation without the need to disassemble the cells. As shown in **Figure 2.2b**, the micro-CT images show a morphology which in agreement with the SEM images of the pristine anode, cathode, cellulose separator, and TiO_2 separator. Accordingly, the 3-dimensional (3D) imaging of these films shown in **Figure S2.21** offers gives a more comprehensive understanding of the material structures. The loosely packed Zn anode used in this work is made of large particles, with sizes in the range of 50 - 100 µm, which hence reduces the surface passivation induced by the spontaneous reaction with the electrolyte. Energy Dispersive X-Ray Analysis (EDX) further shows the homogeneous coverage of the Bi_2O_3 and the fluoropolymer binders on the surfaces of the Zn particles (**Figure S2.5**). As the dissolved zincate ion preferably redeposits on to the Bi surface during charge, this homogeneous coverage of the Bi_2O_3 particles can reduce the possible formation of Zn dendrite. The TiO_2 separator contains much smaller particles to form a dense and homogenous film, thus can effectively reduce the dendrite growth by providing a field of nucleation sites for dissolved zincate ions to precipitate on to next to the anode (**Figure S2.7**). In comparison, the AgO electrode uses 1 - 20 µm particles to produce a porous electrode, which was paired with a separator with similar particle sizes to capture the dissolved Ag species (**Figure S2.6** and S8). Overall, with good wetting, the porous electrodes facilitate permeation of the electrolyte, thus allowing the fabrication of cells with thicker electrodes to increase areal capacity. The conductivity of the PVA-based electrolyte (**Figure 2.2c**) is in the 10^2 mS/cm order in a wide range of temperatures (-10 °C to 60 °C), similar to that of other gel electrolytes reported in the literature.[15,38] The solid-phase hydrogel holds the ability to properly wet the electrodes which allows higher current cycling, while serving as a leak-free electrolyte barrier blocking dendrite growth. The hydroxide concentration was shown to have little effect on the electrolyte conductivity (**Figure S2.9**), but had a significant impact to the cycle life of the battery (**Figure S2.13**), and was thus optimized to be 36.5% by weight.

Figure S2.10 displays 3-electrode cells, using a Zn foil as a pseudo-reference electrode, that was used for cyclic voltammetry (CV) analysis. The AgO-Zn battery is designed to charge and discharge within the window of 1.35 V to 2 V which is used as the CV scanning range. As shown in the full cell CV in **Figure 2d-i**, within the scanning rate of 10 mV/s, the cell can undergo a high current density of up to 20 mA/cm^2, proving the cell's ability to discharge at high current. It is worth noting that the CV scan in the initial cycles are discharging the battery, hence leading to a shift in the voltammogram, which eventually stabilizes as the charging and discharging current reached equilibrium in each cycle. Using the external Zn reference, the full cell CV can be used to gauge the potential shifts of each electrode separately. As shown in **Figure 2.2d-ii**, the relative anode potential (left) does not shift significantly during the sweep, whereas the cathode potential (right) contributes to the majority of the potential change in the cell, suggesting that the AgO cathode is being the rate-limiting electrode in the charge-discharge process. The CV of the current collectors in the corresponding voltage window (**Figure S2.11**) is overlaid in **Figure 2.2d-ii**, demonstrating the electrochemical stability of the current collectors within the expected potential range. It is worth noting that the current density of the Ag current collector increases towards the negative potential direction, which corresponds to the possible hydrogen evolution reaction taken place on the anode during the charging process. Such undesirable reaction is generally avoided as lower current density is used in the normal charging processes, corresponding to lower anode polarization (**Figure S2.18**).

2.2.3 AgO-Zn Battery as A High Areal Capacity Primary Cell

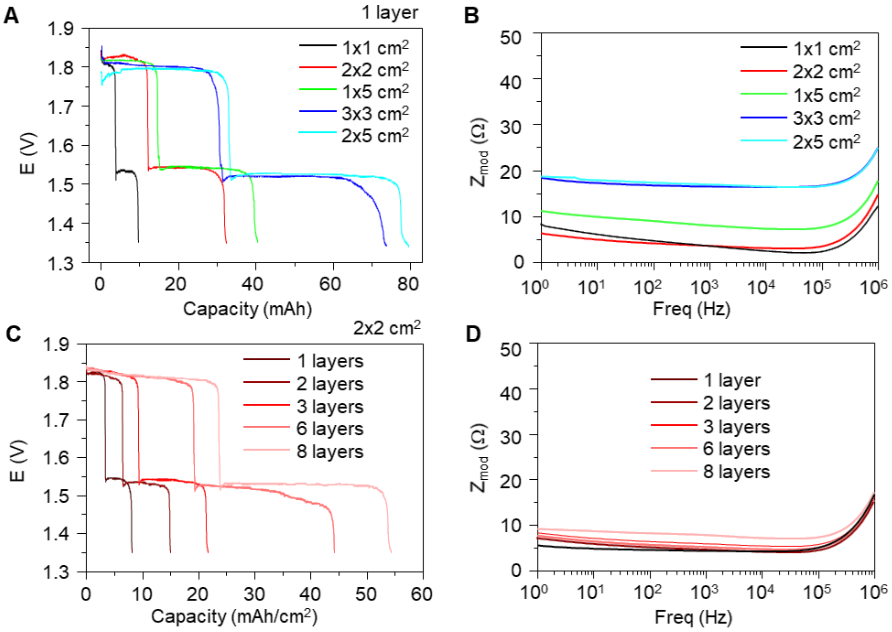

Figure 2.3 | Electrochemical performance of the AgO-Zn cells as primary batteries. (a) The obtainable capacity of various sizes of cells that were printed with 1 layer of active materials, discharged at a current of 1 mA. (b) Bode plot reflecting the corresponding impedance of cells of different sizes. (c) The obtainable capacity of the 2 × 2 cm2 cells with active material loading from 1 layer to 8 layers. (d) Bode plot reflecting the corresponding impedance of the 2 × 2 cm2 cells with different areal loading.

The ability of the cell design to adapt to different cell sizes and areal loadings was evaluated. Cells with the same electrode thickness but different form factors, by varying the electrode designs, as well as the cells with the same form factors and different thicknesses by varying the number of layers of active material printed, were fabricated and discharged at a constant 1 mA current. As shown in **Figure 2.3a**, cells with 1-layer (anode ~ 120 µm, ~ 45 mg/cm^2, cathode ~ 75 µm, ~ 26 mg/cm^2) of electrode thickness with the sizes of 1 × 1 cm^2, 2 × 2 cm^2, 1 × 5 cm^2, 2 × 5 cm^2 and 3 × 3 cm^2 were prepared, and the capacity increases proportionally to the cell area, with an average areal capacity of 8 mAh/cm^2. Two distinct plateaus observed in the discharge voltage curves correspond to the transition of AgO to Ag_2O (~1.8 V) in the beginning of the discharge and the transition of Ag_2O to Ag (~1.5 V) as the higher-oxidation-state AgO depletes in the cathodes. The impedance of these cells was measured via 2 electrodes EIS, presented in **Figure 2.3b**. The overall increase in impedance throughout the high frequency and low-frequency domain suggests an increase in cell contact resistance, caused by the increase in resistance of the current collector as the cell size increases. Cells with a size of 2 × 2 cm^2 were also characterized with increasing areal loadings by printing 1, 2, 3, 6, and 8 layers of electrodes. As demonstrated in **Figure 2.3c**, as the areal loading of active material increases, the areal capacity of the cell increases proportionally, reaching as high as 54 mAh/cm^2 with 8 layers of electrodes (anode ~ 800 µm, ~ 310 mg/cm^2, cathode ~500 µm, ~ 180 mg/cm^2). The EIS on the cells with different thicknesses also showed no significant impedance increase as the thickness increases: only a minor increase in impedance in the low-frequency domain suggests a slight increase in the diffusion resistance due to thicker electrodes (**Figure 2.3d**). This negligible increase can be attributed to the large pore sizes in both the anode and the cathode relative to the size of the hydroxide ions (OH^-), which applies negligible hinderance to the OH- ion mass transfer when diffusing through the electrodes. Overall, the printed AgO-Zn cell was able to uphold superior performance in a wide range of sizes and areal loading, thus proven its customizability as a primary battery to power various electronics with appropriate sizes and capacity. A comparison between this and other flexible batteries is shown in **Table S2.1** and **Figure S2.1**, showing the obtained areal capacity of 54 mAh/cm^2 being the highest among all printed batteries.

2.2.4 AgO-Zn Battery as High-performance Secondary Cell

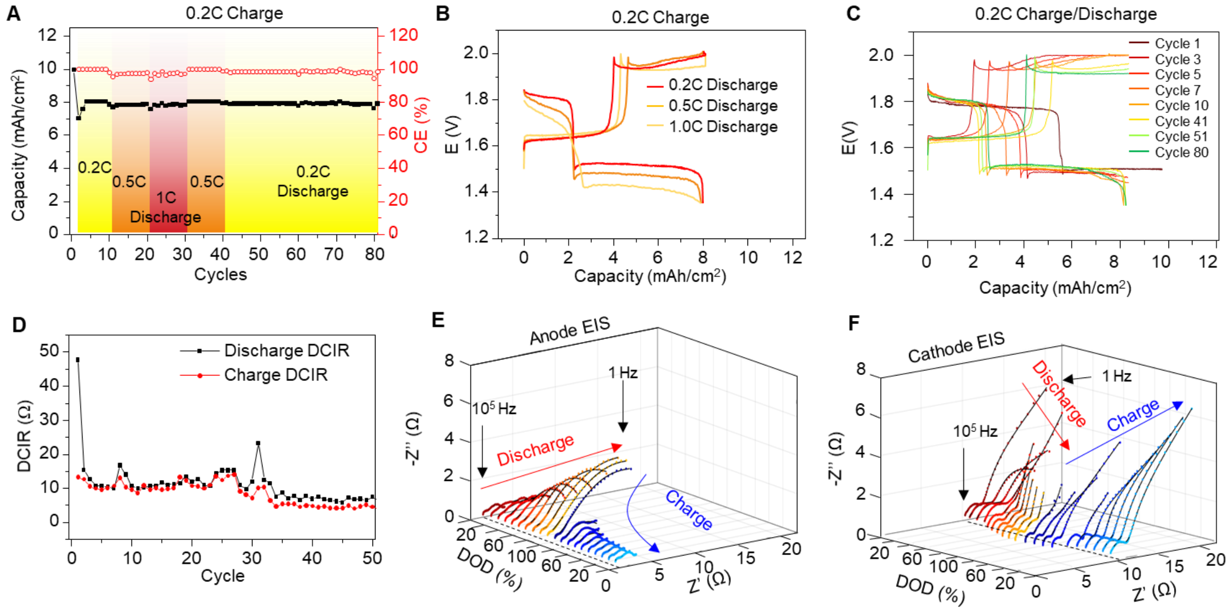

Figure 2.4 | Electrochemical performance of the AgO-Zn cells operating as rechargeable batteries. (a) The cycling performance of the printed battery with a charging C-rate of 0.2C and varying discharge rate of 0.2C, 0.5C, and 1C. (b) The voltage-capacity plot of the battery under different discharging C-rates. (c) The voltage-capacity plot of the AgO-Zn battery at different number of cycles showing the stabilization of the charge-discharge profile. (d) The DCIR of the AgO-Zn within 50 cycles cycled at the C-rate of 0.2C. The EIS profile of the (e) Zn anode and (f) AgO cathode within 1 complete discharge-charge cycle on a 3-electrode cell with a Zn metal pseudo-reference electrode.

Beyond the application as a primary battery, the electrochemical performance of the flexible AgO-Zn battery as a secondary cell was also characterized. As a cell operating with conversion-type chemistry, it is crucial to avoid over-oxidation of the anode materials or over-reduction of the cathode material that would lead to irreversible particle shape change. Previous studies report that the loss of capacity in this system is due to the increased thickness of the ZnO layer that passivates the anode surface, as well as the coarsening of the AgO/Ag_2O particles leading to a decrease in cathode surface area.[8,36] Such behavior can be effectively mitigated by accurately controlling the degree of charge and discharge to limit the occurrence of irreversible electrode shape changes. The optimized charge-discharge algorithm was determined to cycle the cell between 40% and 90% of its maximum capacity, with larger ranges resulting in lower cycle life as shown in **Figure S2.12**. **Figure 2.4a** demonstrates the cycling of a cell with 2-layer electrodes with a maximum capacity of ~ 16 mAh/cm^2. A formation cycle is firstly performed, discharging 10 mAh/cm^2 (60% of max. areal capacity) at the rate of 0.1C, allowing the electrode to slowly relax into its preferred morphology with increased surface area and reduced impedance. Then, the batteries were charged at 0.2 C rate until reaching 2 V and charged at constant voltage until the C-rate dropped to below 0.04 C or the capacity reached 8 mAh/cm^2 (50% of max. areal capacity). The battery was then discharged at 0.2 C until reaching a columbic efficiency of 100% or a voltage of 1.35V. The entire charge-discharge process is accurately controlled by capacity in the initial cycles, ensuring the cell is cycled between 40% to 90% of its maximum capacity. As shown in **Figure 2.4c**, after a few cycles at the rate of 0.2 C, the cell slowly relaxed from capacity-controlled discharge to voltage-controlled discharge, with the higher plateau to lower plateau ratio resembling the behavior of the primary cells. Using such charge-discharge algorithm, the cycle life of the unstable AgO oxidation state could be controlled, and a significantly increased cycle life can be obtained compared to previous studies.[10,29,39] Due to the supersaturation-precipitation reaction mechanism of both the anode and the cathode during discharge, the cell can be discharged at a high C-rate of up to 1 C without any loss in capacity and columbic efficiency, as shown in **Figure 2.4a-b**. Recharging at a higher C-rate is also possible, as shown in **Figure S2.14**, although this would require a higher capping voltage, reducing the rechargeability and increasing and the risk of oxygen evolution on the cathode, thus was not preferred.

Impedance measurements of the flexible batteries showed relatively low impedances throughout cycling. The impedances of the batteries were either determined during cycling of the full-cell using direct current internal resistance (DCIR) method, or during cycling of the separated anode and cathode half-cells using a 3-electrode configuration with a Zn foil serving as the reference. The DCIR analysis offers a straightforward and simple way to gauge the change in the internal resistance of the battery. As shown in **Figure 2.4d**, 2-electrode DCIR analysis with both charging and discharging current was performed before each charge and discharge for a battery cycling at 0.2 C, and the battery was able to maintain low internal resistance throughout the cycles, suggesting no formation of high-impedance passivating layers on the surface of the electrode throughout cycling. To obtain detailed information on the change in the impedance of each electrode during each cycle, multiple 3-electrode EIS analyses were performed on the battery while cycling at 0.2 C, and is plotted against the degree of discharge (DOD) of the battery. As presented in **Figure 2.4e**, the anode half-cell started at a low impedance of 1 – 4 **Ω**, with 2 depressed semicircles attributed to the high-speed charge transfer at the Zn particle interface and the lower speed hydroxide ions (OH-) diffusion in the porous network.[38] With discharging the low-frequency semicircle slowly expands due to the formation and growth of the ZnO species that impedes the OH^- transport and increases the double-layer capacitance. During charging, the oxygen species are liberated from the reactions in Equations 1-3 to form OH^- ions that diffuse readily out of the anode. This results in the fast mass transport of OH^- ions out of the anode and a rapid drop in the impedance at the onset of charging that eventually recovers to the initial level, thus showing the reversibility of stripping and depositing of Zn on the anode. For the cathode half-cell EIS showed in **Figure 2.4f**, at the start of the discharge (0% DOD), a single semi-circle corresponding to the mass transfer resistance and capacitance of the Ag_2O formation is observed with a low-frequency impedance tail at an angle of approximately 45° suggesting standard Warburg diffusion of OH^-. As the cell is discharged, the overall impedance decreases with a second semicircle emerging near the low-frequency domain that can be attributed to the charge transfer resistance and capacitance of Ag formation from Ag_2O. During charging, this second low-frequency semicircle disappears as all the Ag oxidizes to form Ag_2O and eventually AgO.

Overall, the 3-electrode impedance results provide a deeper insight into the reaction and possible routes in improving the battery's cycle-life and performance. These data indicate that the impedance of the AgO cathode is responsible for the majority of the cell impedance. Therefore, a beneficial next step will be to incorporate additives that can increase the cathode electrical conductivity to improve the performance in high-current applications. For the anode, the monitoring of ZnO formation via EIS can be paired with topological characterization methods to better control the conversion of Zn electrodes towards extended cycle life and is expected to be extremely useful for future analysis. More data and discussion of 3-electrode EIS can be found in the supplementary section and **Figures S2.15-2.17**.

2.2.5 Mechanical Stability of The Flexible AgO-Zn Battery

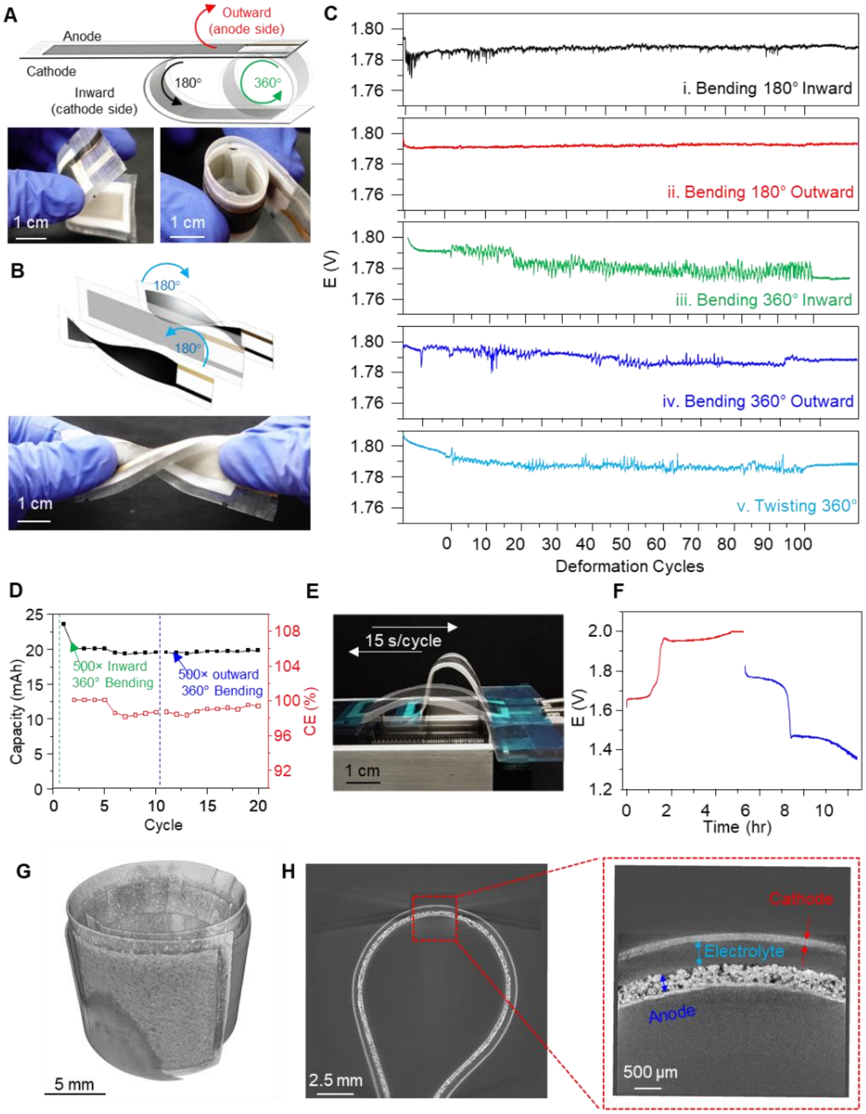

Figure 2.5 | Performance of the AgO-Zn cell under various mechanical deformations. (a) Illustrations and corresponding photo images of a 2-layer loading, 1 × 5 cm^2 battery undergoing (a) 180° and 360° bending deformations and (b) 360° twisting deformation. (c) The corresponding voltage profile of the battery during 1 mA discharge while undergoing 100 cycles of (i) 180° outward bending, (ii) 180° inward bending, (iii) 360° inward bending, (iv) 360° outward bending with a bending diameter of 1 cm, and (v) 360° head-to-end twisting. (d) Assessing the effect of bending to the capacity of the battery. A 2-layer loading, 1 × 5 cm^2 battery undergoing 500 cycles of inward 360º bending and 500 cycles of similar 500 cycles of outward bending demonstrated no drop in battery capacity nor coulombic efficiency. (e) Photo illustration of a battery under repeated 180° bending cycles controlled by a linear stage at the speed of 15 s/cycle, and (f) the corresponding voltage-time plot of the charging (red) and discharging (blue) of the battery during ~2500 repetitions of bending. (g) The micro-CT image of the entire 1 × 5 cm^2 cell after repeated bending and twisting cycles rolled in a diameter of 1 cm, and (h) the cross-section of it bent in a diameter of 1cm (left) and a zoomed-in view (right) of the electrodes, demonstrating no structural damage or delamination of the cell after repeated mechanical deformations.

Compared to coin-cell, cylindrical or prismatic cells, the printed flexible batteries have the unique advantage of allowing bending, flexing, and twisting without causing sudden structural failure. To endow such mechanical resiliency, the printed AgO-Zn batteries are composed of flexible and stretchable polymer-particle composite layers containing highly elastic binders that can accommodate for the applied strain while maintaining the overall structural integrity. During bending, this flexibility and stretchability allow the layers to elongate on the outer rim of the arc to react to the tensile strain, thus allowing the battery to avoid delamination between layers even when very thick electrodes are used. After vacuum sealing, the atmospheric pressure is exerted to the cell and ensure intimate contact between the different layers, further avoiding possible delamination. To test the performance of the batteries under small-radius, large angle deformation, a 2-layer 1 × 5 cm^2 cell was fabricated and discharged at a current of 1 mA while undergoing repeated bending and twisting deformations. As illustrated in **Figure 2.5a-b**, the cell was tested manually with 180° and 360° bending towards anode (outward) and towards cathode (inward) around a cylinder with a radius of 0.5 cm, as well as 180° twisted in both directions from head to end. The corresponding voltage change during 100 cycles (1 s per cycle) of deformation was recorded, as shown in **Figure 2.5c**. In general, the cell exhibited stable performance during bending and twisting in both directions, with negligible fluctuation in voltage during the 180° bending cycles, and roughly 10 mV fluctuation during the 180° bending and twisting cycles. The inward bending in general shows slightly more variations, which is suspected to be caused by the softer Ag current collector on the anode size undergoing more stretching on the outside during bending. More data of the cell under 10% stretching deformation can be found in **Figure S2.20**. The effect of bending to the capacity of the cell was also analyzed via a small-radius repeated bending experiment. A 1 × 5 cm^2 battery was first bent inward 360º for 500 times with a bending radius of

0.5 cm and was then charged and discharged for 10 cycles. Thereafter, the battery was similarly bent outward 360º for 500 times and charged and discharged for 10 more cycles. As shown on **Figure 2.5d**, no significant drop in capacity nor coulombic efficiency was observed after the bending cycles, hence demonstrating the stable mechanical performance of the battery as a flexible, rechargeable cell. The rechargeability of the cell was also not interrupted by the repeated deformation during cycling, as shown in **Figure 2.5e-f** and **Video S2.1**, where the battery can be normally charged and discharged while undergoing ~2500 cycles of 180° bending cycles. To ensure the mechanical stability of the cell, micro-CT was used to characterize the cell after the repeated deformation. As shown in **Figure 2.5g-h**, the entire cell can be scanned at a high resolution to obtain a 3-dimensional (3D) image reflecting the microscopic structure of the cell under deformation after repeated bending and twisting. The zoom-in view of the cross-section of the battery further shows no cracks or delamination after the repeated bending cycles, reflecting the robust mechanical resiliency of the battery against such deformation. More 3D visualizations of the battery under bending deformation can be found in **Figure S2.21**. Overall, pairing the superior electrochemical and mechanical performance, the printed AgO-Zn battery is proven to be **well-suited to reliably and sustainably power various wearable and flexible electronics.**

2.2.6 Powering Flexible Electronics

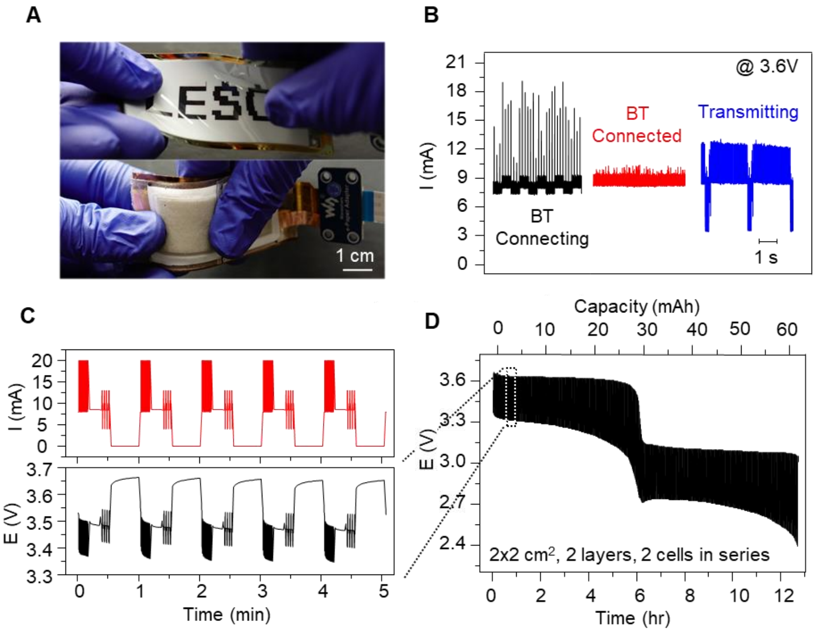

Figure 2.6 | The powering of a flexible E-ink display system by the flexible AgO-Zn batteries. (a) Photo images of the flexible E-ink display and the placement of two 2-layer loading, 2 × 2 cm^2 batteries connected in series on the back of the display. (b) The power consumption of the E-ink display system with integrated BT and MCU modules during BT connection (black), after establishing the connection (red), and during active data transmission (blue). (c) Simulated discharge current profile with varying pulses and baselines (red) and the corresponding voltage response of the battery (black). (d) The complete discharge profile of the two cells connected in series implementing the simulation discharge profile.

To demonstrate the performance of the battery powering typical flexible electronics, we designed a flexible E-ink display system controlled by an Arduino-type microcontroller unit with added Bluetooth (BT) communication module, which resembles many prototypes of IoT, wearable and flexible devices (**Figure 2.6a and S2.22**). The system is powered by two 2 × 2 cm^2 batteries with 2-layer electrodes connected in series, which can supply enough voltage (>3 V) to boot the system. A mobile device can connect and transmit data and commands to the BT module, which is processed by the microcontroller that refreshes the E-ink display. First, the energy consumption of the system under different operation modes operating at 3.6 V was measured. **Figure 2.6b** displays the current draw when (1) the system is broadcasting to seek for connection, which contains short bursts of current peaks around 20 mA (in black); (2) the system is connected to a mobile device, with an average current of 9 mA (in red); and (3) the system is actively transmitting data between the cellphone and the display, with the current alternating between a higher baseline of 8.5 mA with peaks of 13 mA, and a lower baseline of 4 mA with peaks of 10 mA (in blue). The batteries are thus discharged using a script simulating the power consumption of the flexible E-ink display system working in repeated discrete sessions, with 10 s of BT broadcasting, 10 s of idle after establishing the connection, 10 s of active data transmission, followed by 30 s of resting (powered off) (**Figure 2.6c and S2.24**). As illustrated in **Figure 2.6d**, the two batteries in series were able to sustain the pulsed, high-current discharge in the 3.6 V – 2.4 V window to deliver power to the system constantly for over 12 hours, and is able to maintain its capacity of ~60 mAh, similar to the capacity obtained from the constant low-current 1 mA discharge. By pairing with the high-areal capacity flexible AgO-Zn battery, the flexible E-ink display was able to operate while undergoing bending deformations, which is demonstrated in **Video S2.2**. In comparison, commercial lithium coin cells with similar rated capacity were not able to sustain the high current pulsed discharge, resulting in a significant loss in capacity when discharged using the same script (**Figure S2.24**). The low-impedance and high-energy-density battery is therefore proven to have both outstanding electrochemical and mechanical performance for powering of a typical prototype of a flexible electronic system. With their performance even surpassing its non-flexible commercial coin cell counterpart, such all-printed battery can be considered extremely attractive due to its customizability, and flexibility towards real-life applications. A typical application of using the battery to illuminate an LED bulb while applying various mechanical deformations were also tested, where the light intensity does not change as the battery is bent, folded, twisted, and stretched (**Video S2.3**).

2.3 Discussion

In this work, we have demonstrated a flexible and high-performance AgO-Zn battery based on the rechargeable conversion chemistry. Using specially formulated ink with stretchable elastomeric binders and thermoplastic elastomeric substrates, the batteries can be printed layer-by-layer using low-cost, high-throughput screen-printing techniques and assembled with a heat and vacuum sealing processes. To obtain a low device footprint while maintaining easy processability, printable and flexible separators and solid-phase KOH-PVA hydrogel were developed to allow a stacked sandwich configuration. The printable battery is compatible with various cell sizes and areal loading, leading to a high areal capacity of 54 mAh/cm^2 in connection to repeated multilayer printing for primary applications. The battery is also rechargeable upon implementing the capacity-controlled cycling algorithm, with high cycle life beyond 70 cycles with varying discharge C-rates without loss in capacity and coulombic efficiency. The battery exhibited low impedance within each discharge-charge cycle, while maintaining low internal resistance throughout multiple cycles, suggesting stable and reversible electrode morphological change during electrode redox reactions. As a flexible energy storage unit for powering various flexible, wearable electronics, the performance of the battery was evaluated under rigorous mechanical testing, demonstrating that the battery offers remarkable resiliency against repeated large deformation bending and twisting cycles. The fabricated batteries were used in the powering of a customized flexible E-ink display system with BT connectivity and delivered an outstanding performance that surpassed commercial coin cells under the high-current pulsed discharge regime required by the electronics. Future work leveraging advanced electrochemical and topological characterization on this promising battery chemistry will be conducted to further improve its performance and cycle life. This will involve further optimization of the fabrication process, the ink composition, and the layer thicknesses and porosities should lead to a practical, commercially viable product with higher cycle life, lower impedance, smaller device footprint, and lower production cost. Overall, this work demonstrates the scalable fabrication of flexible AgO-Zn batteries with highly desirable electrochemical and mechanical performance and tremendous implications towards the development of novel energy storage devices for the powering of next-generation electronics.

2.4 Experimental Procedures

2.4.1 Chemicals

Bi_2O_3, $Ca(OH)_2$, KOH (pellets, ≥85%), LiOH, methyl isobutyl ketone (MIBK), toluene, cellulose (microcrystalline powder, 20 µm), Triton-X 114, Poly(ethylene oxide) (PEO) (MW 600,000), and PVA (MW = 89000 – 98000, 99+% Hydrolyzed) were purchased from Sigma Aldrich (St. Louis, MO, USA). Zn (Grillo-Werke AG, Germany), AgO (Ames Goldsmith, South Glens Falls, NY, USA), and TiO_2 (CR-470, Tronox Holdings plc, New York, NY, USA) were obtained from Zpower LLC (Camarillo, CA, USA). The fluorocopolymer (GBR-6005, poly(vinylfluoride-co-2,3,3,3-tetrafluoropropylene)) was obtained from Daikin US Corporation (New York, NY, USA). SEBS (G1645) was obtained from Kraton (Houston, TX, USA). Graphite powder was purchased from Acros Organics (USA). Super-P carbon black was purchased from MTI Corporation (Richmond, CA, USA). All reagents were used without further purification.

2.4.2 Cell Fabrication

2.4.2.1 Formulation of The Flexible Inks

The electrode resin was prepared by adding 5 g of the fluorine rubber in 10 g of MIBK solvent and left on a shake table overnight, until the mixture was homogeneous. The SEBS resin was prepared by adding 40 g of the SEBS into 100 mL of toluene and left on a shake table until the mixture was homogeneous.

The silver current collector ink was formulated by combining Ag flakes, SEBS resin, and toluene in 4: 2: 1 weight ratio and mixing in a planetary mixer (Flaktak Speedmixer^{TM} DAC 150.1 FV) at 1800 rotations per minute (RPM) for 5 min.[40] The carbon current collector ink was formulated by firstly mixing graphite, Super-P, and PTFE powder in 84: 14: 2 weight ratio with a set of pestle and mortar. The mixed powder was mixed with the SEBS resin and toluene in a 10: 12: 3 weight ratio using the mixer at 2250 RPM for 10 min to obtain a printable ink.[10]

The Zn anode ink was formulated by firstly mixing the Zn and Bi_2O_3 powders in a 9:1 weight ratio with a set of pestle and mortar until the Zn particles are evenly coated with the Bi_2O_3 powder. The evenly mixed powder was then mixed with the electrode resin and MIBK in a 20: 4: 1 weight ratio using the mixer at 1800 RPM for 5 min to obtain a printable ink. The AgO cathode ink was formulated by firstly mixing the AgO and Super-P powders in a 95: 5 weight ratio using a set of pestle and mortar until homogeneous. The powder was then mixed with the electrode resin and MIBK in 5: 5: 2 weight ratio using the mixer at 2250 RPM for 5 min to obtain a printable ink.

The TiO_2 separator ink was prepared by firstly mixing TiO_2 and cellulose powder in a 2: 1 weight ratio using a set of pestle and mortar. The mixed powder was then added with the SEBS resin, toluene and Triton-X in 50: 55: 75: 3 weight ratio and mixed with the mixer at 2250 RPM for 10 min to obtain a printable ink. The addition of Triton-X surfactant in the anode separator ensures the proper wetting of the thick Zn anode, hence increase the effective electrochemical surface area of the anode and avoid high local current density that would lead to dendrite growth. The cellulose separator ink was prepared by firstly mixing TiO_2 and cellulose powder in a 26: 9 weight ratio using a set of pestle and mortar. The mixed powder was then added with the electrode resin, MIBK in an 8: 7: 4 weight ratio and mixed with the mixer at 2250 RPM for 10 min to obtain a printable ink.

All inks above were formulated empirically to obtain a screen-printable consistency, which was adjusted with various amounts of solvent to achieve good printing quality. The particle size distribution of the powders used in this work is summarized in **Table S2.3**.

2.4.2.2 Preparation of The SEBS Substrate

SEBS was dissolved in toluene with a weight ratio of 6 to 8.7 and was left on a linear shaker (Scilogex, SK-L180-E) overnight or until the mixture became transparent and homogeneous. Wax paper was used as the temporary casting substrate, and a film caster with the clearance of 1000 um was used to cast the SEBS resin onto the wax paper. The cast resin was firstly dried in the ambient environment for 1 h, followed by curing in a conventional oven at 80 °C for 1 h to remove the excess solvent. The transparent, uniform SEBS film, which can be readily peeled off from the wax paper after curing, was used as the substrate for subsequent battery printing.

2.4.2.3 Printing of The Electrodes

Stencils for printing the current collectors, electrodes, and separators were designed using AutoCAD software (Autodesk, San Rafael, CA, USA) and produced by Metal Etch Services (San Marcos, CA), with dimensions of 12 in × 12 in. The stencils used in this work were stainless steel cut-out stencils without meshes. The thickness of the stencils was designed to be 100 µm for the carbon and silver current collectors, 300 µm for the TiO_2 separator and the Zn anode, and 500 µm for the cellulose separator and the AgO cathode. The printing of the following layers was performed using a semi-automatic MPM-SPM printer (Speedline Technologies, Franklin, MA, USA) with an 8-inch metal blade squeegee. The stencil and squeegee pressure were optimized for each stencil, correspondingly. To print the anode, the silver ink was first printed onto the SEBS substrate and cured in a conventional oven at 80 °C for 10 min. The Zn ink was then printed onto the silver current collectors and cured at 80 °C for 30 min. The TiO_2 ink was lastly printed onto the anode and cured at 80 °C for 10 min. To print the cathode, the carbon ink was firstly printed onto the SEBS substrate and cured at 80 °C for 10 min. PET sheets were cut using a computer-controlled cutting machine (Cricut Maker®, Cricut, Inc., South Jordan, UT, USA) into a mask exposing the printed carbon electrodes, and the masked carbon current collector was sputtered with ~ 400 nm of Au and adhesion interlayer of Cr at a DC power of 100W and 200W respectively and an Ar gas flow rate of 16 SCCM using a Denton Discovery 635 Sputter System (Denton Discovery 635 Sputter System, Denton Vacuum, LLC, Moorestown, NJ, USA). The AgO ink was then printed onto the sputtered current collectors and cured at 50 °C for 60 min. Lastly, the cellulose ink was printed onto the cathode and cured at 50 °C for 60 min. To print multiple layers of electrodes or the separators, the stencil was offset by an additional 65 µm for each layer of AgO and 100 µm for each layer of Zn to compensate for the electrode thickness. See **Figure S2.2** for the step-by-step printing and assembly process of the batteries and **Figure S2.3** for the thickness calibration for the printing of anode and cathode.

2.4.2.4 Synthesis of The Electrolyte Hydrogel

The hydrogel is synthesized by mixing the PVA solution and the hydroxide solution into a gel precursor and dried in a desiccator until the desired weight is reached. For synthesizing the 36.5% hydroxide gel used in this study, the following formulations were used. A hydroxide solution was prepared by dissolving 9.426 g KOH and 0.342 g LiOH into 50 mL deionized (DI) water. 0.5g $Ca(OH)_2$ was then added into the solution and stirred in a closed container under room temperature for 1 h to saturate the solution with $Ca(OH)_2$, and the excess $Ca(OH)_2$ was then removed from the solution. A PVA solution was prepared by dissolving 4.033 g PVA and 0.056 g PEO into 50 mL DI water heated to 90 °C. The precursor solution was prepared by mixing the hydroxide solution and the PVA solution in the weight ratio of 13.677: 10 and poured into a flat petri dish with the weight of 0.2 g/cm^2. The precursor was left to dry in a vacuum desiccator until the weight decreased to 26.12% of precursor weight to obtain a soft, translucent hydrogel with its caustic material taking 36.5% of the sum of caustic material and the water content. Additional weight and conductivity information for different hydroxide concentrations can be found in **Table S2.2**. The hydrogel can ben then cut into desired sizes and directly used or stored in a hydroxide solution with the same weight ratio of hydroxide without PVA. The storage solution for the 36.5% KOH-PVA gel was prepared similar to the hydroxide solution, where 10.777 g KOH, 0.391 g LiOH, and 0.5g $Ca(OH)_2$ were dissolved into 15 mL DI water and the excess $Ca(OH)_2$ was removed. More images of the fabrication of the hydrogel are shown in **Figure S2.4**.

2.4.3 Microstructural Characterization

Morphological analyses of the current collectors, separators, and active material electrodes were performed with SEM and micro-CT. SEM images were taken using an FEI Quanta FEG 250 instrument with an electron beam energy of 15 keV, a spot size of 3, and a dwell time of 10 µs. Micro-CT experiments were conducted using a ZEISS Xradia 510 Versa. For individual film analysis, micro-CT samples were prepared by punching 2 mm radii disks and stacking them in a PTFE cylindrical tube with alternating PTFE films to provide separation between neighboring film disks. For the Micro-CT of full and sealed cell bending, a 1 × 5 cm^2 Zn-AgO battery was bent or rolled around a polyethylene (PE) cylindrical tube with a diameter of 1cm.

For the micro-CT active material electrodes, the heavier metals, such as Zn and Ag, warranted higher X-Ray energies than the printed polymer separator films. Accordingly, scans at 140 keV and a current of 71.26 µA were performed with high energy filters and a magnification of 4X on the Zn and AgO films with voxel sizes of 2.5 µm and 0.75 µm and exposure times of 2 s and 18 s respectively. For the polymer separators, 80 keV scans with an 87.63 µA current were used with low energy filters at a magnification of 4X with voxel resolutions of 0.75 µm and 1.1 µm and exposure times of 8 s and 1 s for the printed anode and cathode separators respectively. For scans of the full cell bending, a voltage of 140 keV and a current of 71.26 µA with a 4X magnification was performed with the following voxel resolutions and exposure times for the respective cases: 18.35 µm and 2 s for low resolution bending scan, 3.54 µm and 5 s for higher resolution bending scan, and 7.55 µm and 2 s for rolled cell scan. For all micro-CT scans conducted, 1801 projections were taken for a full 360˚ rotation with beam hardening and center shift constants implemented during the data reconstruction. Post measurement imaging and analysis were performed by Amira-Avizo using the Despeckle, Deblur, Median Filter, Non-local Means Filter, Unsharp Mask, and Delineate modules for data sharpening and filtration provided by the software. The animated micro-CT scan of the battery can be found in **Video S2.4-S2.5**.

2.4.4 Electrochemical Characterization

2.4.4.1 Cyclic Voltammetry

The 3-electrode half-cell CV characterization was performed on a cell assembled with the printed electrodes as the working electrode, a platinum foil as the counter electrode, Zn metal foil as the reference electrode, and 2 pieces of KOH-PVA hydrogel as the electrolyte. The 3-electrode full-cell CV characterization was performed between 1.35 V to 2 V on a cell assembled similar to the typical battery architecture but with an extra Zn metal foil as the reference electrode. The structures of both cells are illustrated in **Figure S2.10**. The CV was performed using an Autolab PGSTAT128N potentiostat/galvanostat with an additional pX-1000 module. In the 3-electrode full-cell CV, the AgO cathode was connected to the working electrode probe, the Zn anode was connected to the counter and reference electrode probes, and the pX-1000 module was used to monitor the potential between the cathode and the reference Zn foil. The potential of the anode vs. Zn was obtained by subtracting the cathode vs. Zn potential from the full cell potential. A scan rate of 10 mV/s was used for all CV tests.

2.4.4.2 Discharging and Cycling Protocol

The constant current complete discharge of the battery for primary applications was performed with the following procedure. Firstly, the assembled and vacuum-sealed battery was left idle for 1 hr to allow the electrolyte to fully permeate through the electrodes. Then, the battery was discharged using a battery test system (Landt Instruments CT2001A) at the desired current, until reaching the lower cut-off voltage of 1.35 V.

To enable the secondary application of the battery, cycling protocols were established that rely on the accurate control of the potential and DOD of the battery. To perform charge-discharge cycling on a fabricated battery, 50% of its maximum capacity, which was estimated by the low-current complete discharges, was first determined as the cyclable capacity and the basis to determine C-rates of the protocol. The battery was firstly discharged at the C-rate of 0.1 C from 100% to 40% DOD. Then, the battery was recharged at the C-rate of 0.2 C until reaching 2V, and then at 2 V until reaching 90% DOD or C-rate of 0.05C. The battery could be then discharged and recharged at the desired C-rates between 1.35 V and 2 V, with the DOD maintained between 40% and 90% of its maximum value. Unless specified otherwise, all cycling data were performed using cells with 1 × 1 cm^2 form factor with 2 layers of active electrode materials. More cycling data for two cells with 8-layer electrode thickness connected in series is shown in **Figure S2.15**.

The pulsed discharge protocol was designed to simulate the battery's performance in powering a typical MCU-controlled wearable device with integrated BT functionality. The battery was discharged using an Autolab PGSTAT128N potentiostat/galvanostat implementing fast chrono methods. See **Figure S2.25** for the detailed discharging script.

2.4.4.3 Electrochemical Impedance Spectroscopy

Electrochemical Impedance Spectroscopy (EIS) measurements were performed with a Biologic SP-150 in a 3-electrode configuration. The Zn-AgO three electrodes cell was fabricated with a Zn reference wire placed between an extra layer of hydrogel electrolyte and the original electrolyte layer shown in **Figure 2.2b**. The Zn reference wire was then connected to an Au sputtered heat-sealable SEBS-based printed carbon tab that was vacuum sealed to ensure complete cell sealing to hinder electrolyte dehydration. The working electrode (WE) and counter electrode (CE) were connected to the AgO cathode and Zn anode, respectively.

The impedances of the two half cells and the full cell were monitored in-situ during charging and discharging to analyze impedance changes most closely related to practical cycling conditions with a galvanostatic-EIS (GEIS) measurement. Accordingly, the DC base current was set to the current of the charging/discharging step, while the AC amplitude was set to 300 μA, approximately one-fifth of the cycling current. The frequency sweep was between 1 MHz and 1 Hz with 10 points per decade and an average of 8 measures per frequency. The cycling script implemented with GEIS is similar to that of the capacity-limited electrochemical cycling protocol, with the exception that the voltage limits applied were 1.95 V and 1.4 V vs. the reference instead of the anode for the charging and discharging respectfully. For each charge and discharge step, 10 GEIS was measured for 15 complete cycles, resulting in a total of 870 separate Nyquist plots (29 steps × 10 measures × 3 cell configurations). For analysis simplicity, only the 5th cycle's discharge and charge were analyzed.

Both half-cell Nyquist plots for the 5th cycle's discharge and charge steps were fitted to equivalent circuits using a slightly modified version of the Zfit function available as open-source code from Mathworks.[41] Zfit utilizes another Mathworks open source code, fminsearchbnd, to minimize the error of simulated impedances with the experimental values by altering the impedance parameters (i.e. resistance values, constant phase element values, etc.) under realistic parameter boundary conditions.[42] The use of this code allowed for streamline fitting of many successive Nyquist to provide insights in observable trends in the fitted parameters. Additional data of the EIS measurement can be found in **Figure S2.16-2.18**.

2.4.4.4 Electrolyte Conductivity Measurement

The ionic conductivity of the gel electrolyte was measured by a customized two-electrode (Stainless Steel 316L) conductivity cell with an inner impedance at 0.54 Ω. The cell constant is frequently calibrated by using OAKTON standard conductivity solutions at 0.447, 1.5, 15, and 80 $mS\cdot cm^{-1}$ respectively. A constant thickness spacer was positioned between the two electrodes which ensure no distance changes during multiple-time measurements. The electrolytic conductivity value was obtained with a floating AC signal at a frequency determined by the phase angle minima given by Electrochemical Impedance Spectroscopy (EIS) using the following equation: $\sigma = \mathrm{K}R^{-Q}$, where R is the tested impedance (Ω), K is the cell constant (cm^{-1}) and Q is the fitting parameter.[43] All of data acquisition and output were done by LabView Software, which was also used to control an ESPEC BTX-475 programming temperature chamber to maintain the cell at a set temperature in 30 minutes intervals.

2.4.5 Mechanical Deformation Tests

The mechanical testing of the battery was performed on the 1 × 5 cm^2 batteries and was composed of three parts. The first part consisting of the bending and twisting of the cell with controlled bending radius and angles. For the bending tests, the sample was bent around an Eppendorf tube towards the anode (outward) or towards the cathode (inward) with a radius of 0.5 cm, until folded in half (180°) or looped around (360°), at a speed of 1 bending per second. Due to the large deformation with complex movement involved in this test, the bending of the test was conductive manually with the guiding of the tube. Similarly, the twisting of the cell was performed manually, where the 1 × 5 cm^2 sample was twisted 180° clockwise followed by counterclockwise around its longer axis at a speed of 1 twisting per second (**Figure 2.5a-c**). See **Figure S2.19** for the bending control of the battery mechanical tests. Secondly, to quantitatively assess the influence of the bending to the capacity and cycle life of the battery, 500 repetition of 360°, 0.5 cm radius bending was applied to the sample prior to cycling the battery. The battery was then charged/discharged for 10 cycles at a rate of 0.2 C, followed by bending the battery 500 times outward 360° with 0.5 cm radius and cycled for 10 more cycles same rate. The capacity of the battery was monitored to quantitatively measure the influence of bending on the cell (**Figure 2.5d**). The third part of the testing was performed using a linear motor, where the 1 × 5 cm^2 sample was bent freely without angle confinement, from a radius of 3 cm at 40° to the radius of 0.5 cm at 70° repeatedly, while being charge and discharged at 0.2 C. (**Figure 2.5e-f**).

2.4.6 Assembly of Flexible Display Electronics

To demonstrate the battery’s ability to power flexible electronics, a Waveshare 2.9-inch e-Paper flexible display was powered by two Zn-AgO batteries in series. The display module was connected to an Adafruit Feather nRF52 Bluefruit Low Energy (LE) chip and programmed using Arduino and C. The picture of the assembled system is shown in **Figure S2.23**. MATLAB code was used to convert images to hexadecimal format to be uploaded to the board and the display. The BluefruitConnect IOS app was used to connect the Adafruit chip via Bluetooth to change the display. The system diagram of the E-ink display system is shown in **Figure S2.22**. The pulsed current profile needed to power the Bluetooth chip and display was determined using an oscilloscope by measuring the voltage across a 10 Ω resistor connected in series with the circuitry. A model pulsed profile was then extracted to be applied to flexible batteries for further testing.

2.5 Acknowledgements

This work was supported by funding from ZPower LLC, United States and Qualcomm, United States. This work was performedinpartatthe SanDiego Nanotechnology Infrastructure (SDNI) ofUCSD, NANO3, a member of the National Nanotechnology Coordinated Infrastructure, which is supported by the National Science Foundation, United States (grant ECCS-1542148). The authors would also like to acknowledge the National Center for Microscopy and Imaging Research (NCMIR), United States. Technologies and instrumentation are supported by grant R24GM137200 from the National Institute of General Medical Sciences, United States. AgO, Zn, and TiO2 used in this work were provided by ZPower LLC. SEBS used in this work was provided by Kraton, United States.

2.6 Supplementary Section

2.6.1 Supplementary Tables

Table S2.1 | Comparison of areal capacities of various published and commercialized thick-film batteries. The summary is also visualized in Figure S1.

Battery Type	Fabrication	Max. Areal Capacity (mAh/cm^2)	Configuration	Cycle Number	Ref
Zn-Ag_2O	Screen Printing	1.6	In-plane	11	[1]
Zn-Ag_2O	Screen Printing	~3	In-plane	30	[2]
Zn-Ag_2O	Extrusion Printing	~2.8	In-plane	Primary	[3]
Zn-Ag_2O	Screen Printing	1.5	In-plane	13	[4]
Zn-MnO_2	Plotting	~2.2	In-plane	30	[5]
Zn-MnO_2	Doctor Blade	<0.077	Stacked	140	[6]
Zn-Ag_2O	Drop-cast/ Electroplating	0.11	In-Plane	33	[7]
Zn-MnO_2	Screen Printing	5.6	Stacked	Primary	[8]
Zn-Ag_2O	Screen Printing	5.4	Stacked	Primary	[9]
Zn-Ag_2O	3D Printing	2.4	Interdigitated Pillars	7	[10]
Zn-MnO_2	Soaking	3.775	In-plane	Primary	[11]
LTO-LFP	3D Printing	1.5	In plane Interdigitated	30	[12]
Zn-Air	Screen Printing	1.4	Stacked	Primary	[13]
Zn-Ag_2O	Screen Printing	11	Stacked	Primary	[14]
Si/CNT-NMC	Doctor Blade	30	Stacked	50	[15]
Zn-MnO_2	NA	~1	In-plane	Primary	[16]
Zn-MnO_2	NA	~3	NA	Primary	[17]
Zn-MnO_2	NA	~1.5	NA	Primary	[18]
Li-MnO_2	NA	~2.5	Stacked	Primary	[19]
Zn-AgO	Screen Printing	54	Stacked	80	This work

Table S2.2 | KOH-PVA electrolyte information

Caustic Concentration	Removed Precursor Water wt%	σ_0 (mS/cm)	E_a (eV)
26.3%	65.77%	2.037×10^4	0.109
31.8%	70.72%	3.155×10^4	0.115
36.5%	73.88%	6.029×10^4	0.138

Table S2.3 | Particle size distribution from material data sheet of the powder used.

	D10 (μm)	D50 (μm)	D90 (μm)	Avg. Size (μm)
Zn	1.5-2.0	2.5-3.5	5.0-6.0	/
AgO*	/	/	/	/
Cellulose	/	22	53	/
TiO_2	/	/	/	0.2

*: AgO particle distribution: >100 µm = <15%, 100-75 µm = 20-40%, 75-45 µm = 40-60%, <45 µm = <15%

2.6.2 Supplementary Figures

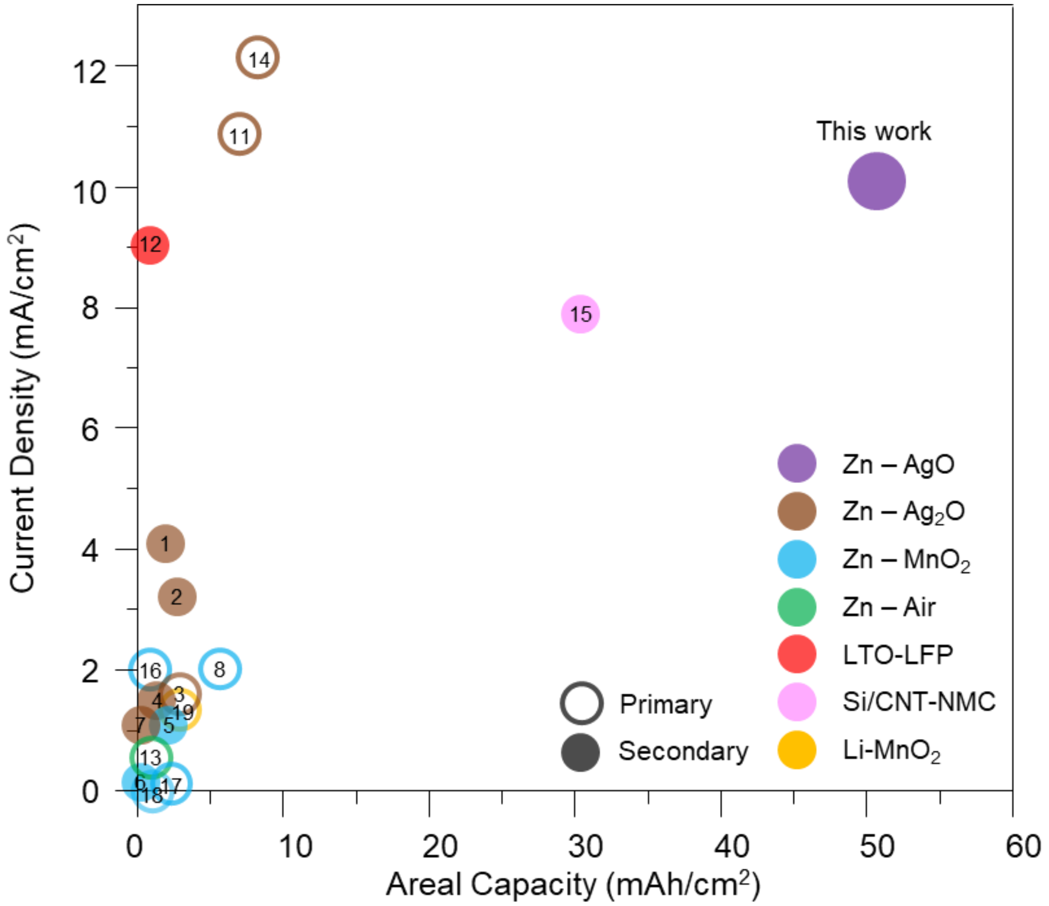

Figure S2.1 | Visualization of Table S2.1 comparing the maximum current densities and areal capacities of various printed batteries.

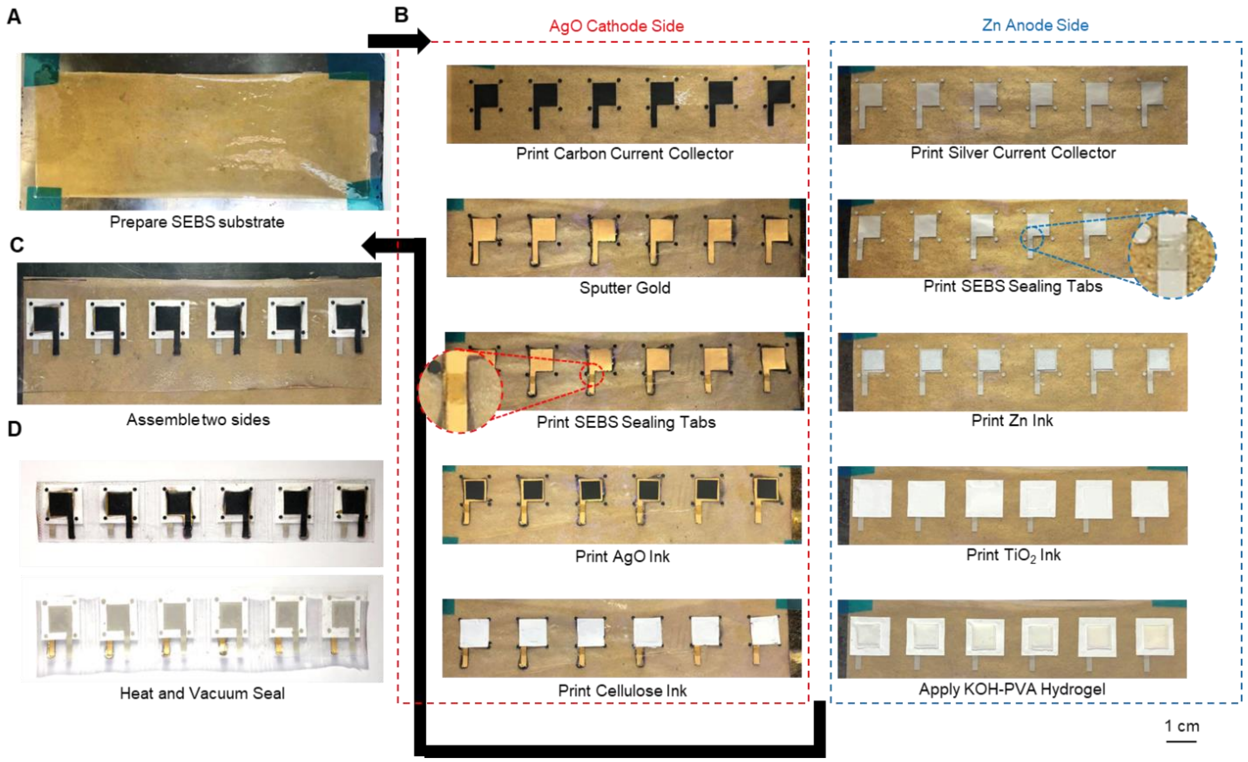

Figure S2.2 | The images of the step-by-step batched fabrication of the printed AgO-Zn batteries. (a) Prepared SEBS substrate. (b) The layer-by-layer printing of the AgO cathode (left) and the Zn anode (right). (c) Placing the cathode side onto the anode side with the hydrogel electrolyte in between. (d) Heat and vacuum sealing of the batteries. Each cell was separated by further heat sealing after the entire batch was vacuum sealed.

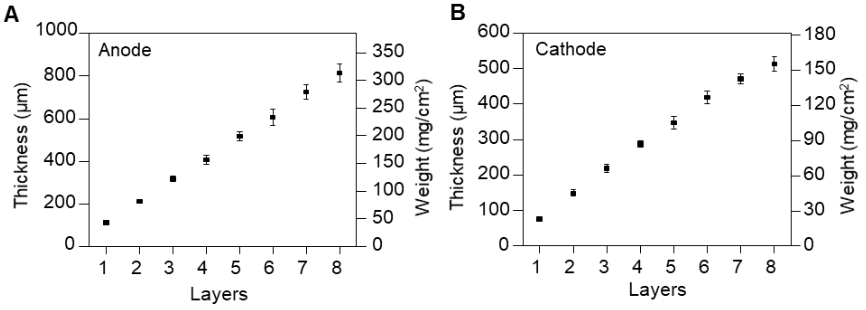

Figure S2.3 | Thickness calibration of the (a) anode and (b) cathode printed using their corresponding stencils. 5 samples were taken to generate the average thicknesses and standard deviations of each data point.

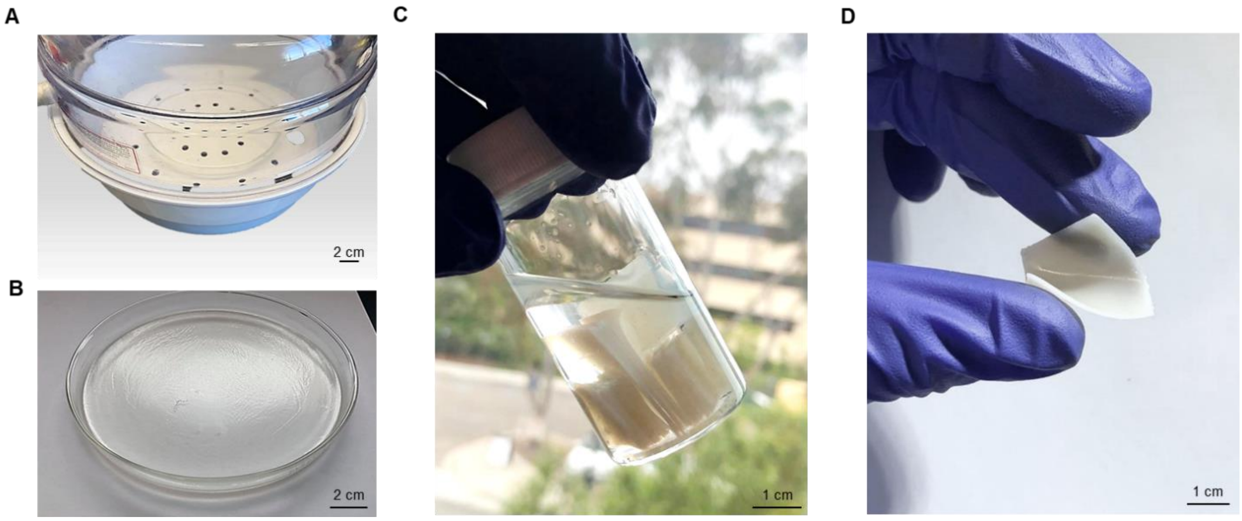

Figure S 2.4 | Images of the fabrication of the KOH-PVA electrolyte gel. (a) Drying of the precursor solution to desired concentration in a vacuum desiccator. (b) The crosslinked 36.5 % hydrogel after drying. (c) Storage of the hydrogel pieces after cutting into desired sizes. (d) A bent 2 × 2 cm^2 hydrogel.

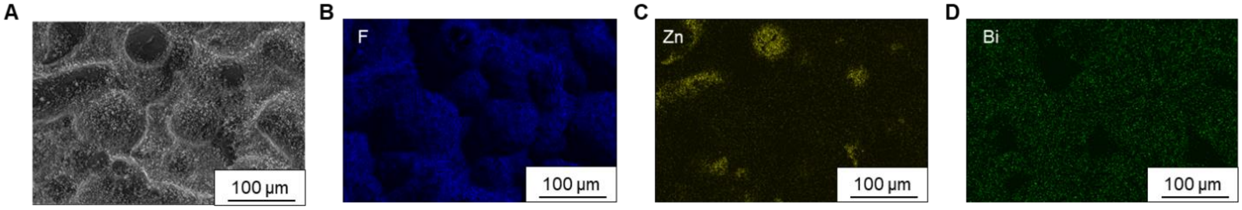

Figure S2.5 | (a) The SEM and corresponding EDX mapping of (b) fluorine (from the binder), (c) Zn, and (d) bismuth of the anode.

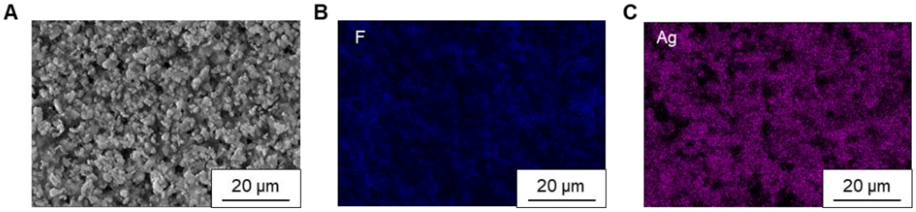

Figure S2.6 | (a) The SEM and corresponding EDX mapping of (b) fluorine (from the binder) and (c) Ag of the cathode

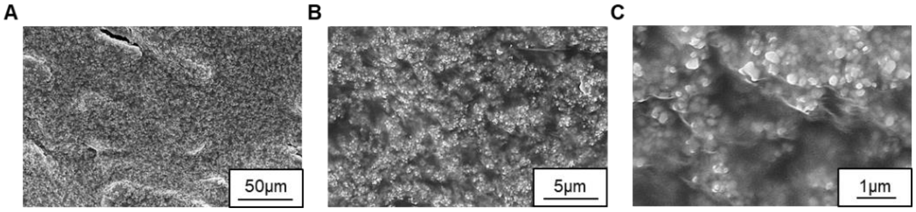

Figure S 2.7 | Additional SEM images of the printed TiO_2 separator with different magnifications.

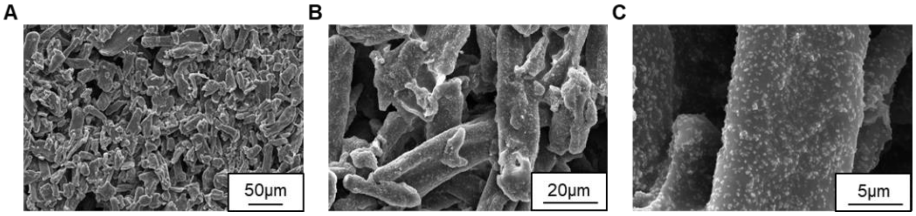

Figure S2.8 | Additional SEM images of the printed cellulose separator with different magnifications.

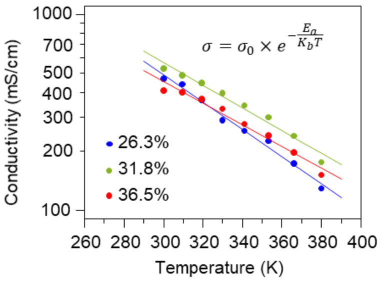

Figure S2.9 The conductivity of the hydrogel with different caustic material concentrations. The linear trendline was fitted using the given equation and listed in Table S2.2.

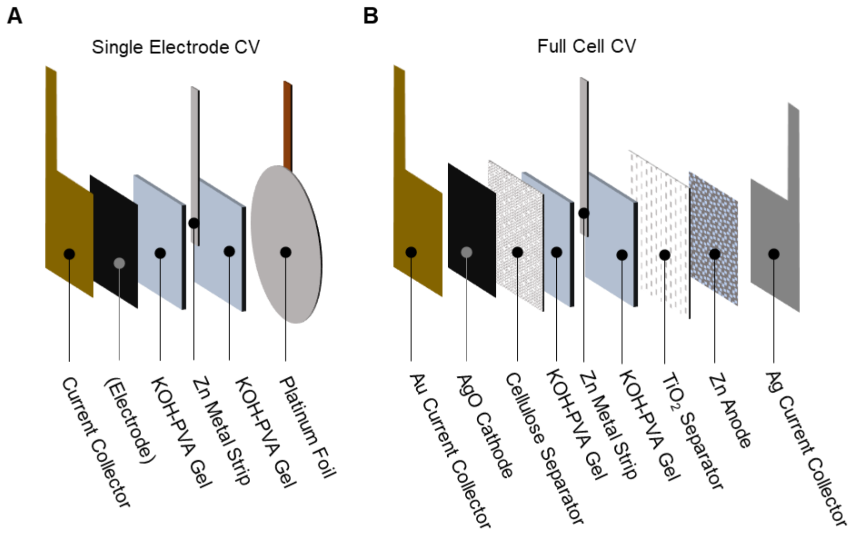

Figure S2.10 | The cell structure used for the CV analysis. (a) The cell structure used for single electrode scanning for testing the current collectors. (b) The cell structure used for full cell scanning with an external Zn metal strip as the reference electrode.

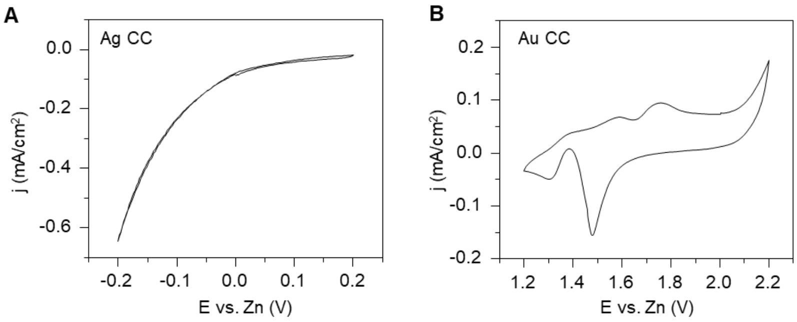

Figure S2.11 | The CV of the printed (A) Ag anode current collector (CC) and the Au-sputtered carbon cathode CC in their corresponding voltage range used in Figure 2.2D-ii. Scan rate: 10 mV/s.

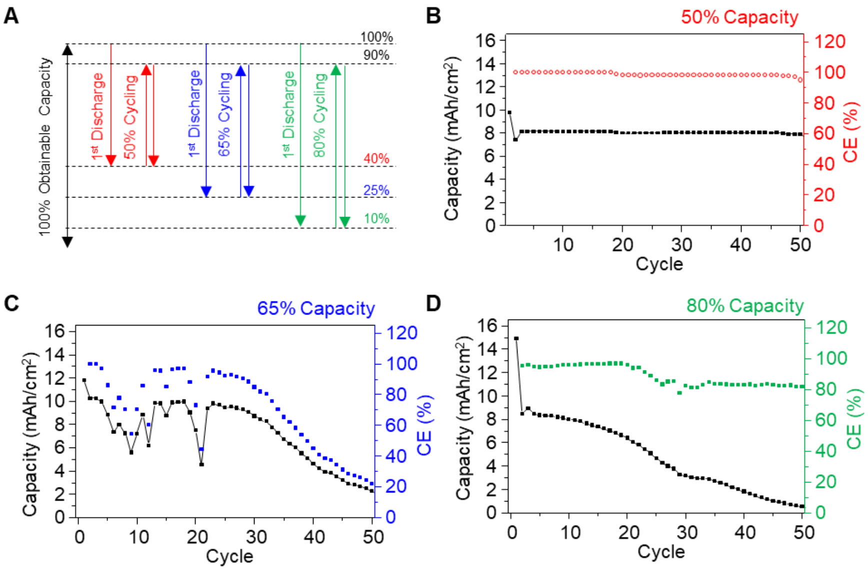

Figure S2.12 | The cycling of the battery at the different capacity range. (a) The illustration comparing 3 different charging and discharging capacity regions. (b) Cycling the battery between 40 % and 90 % state of charge (50 %). (c) Cycling the battery between 25 % and 90 % state of charge (65 %). (d) Cycling the battery between 10 % and 90 % state of charge (80 %). Electrolyte with the concentration of 36.5 % was used, and the cells were cycled at the rate of 0.2 C.

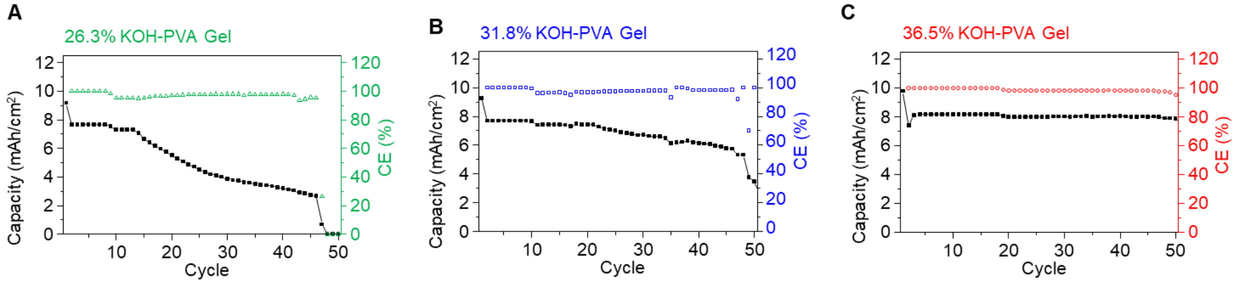

Figure S2.13 | The cycling of the battery with electrolyte concentration of (a) 26.3 %, (b) 31.8 %, and (c) 36.5 %. The 50 % capacity range was used and the cells were cycled at the rate of 0.2 C.

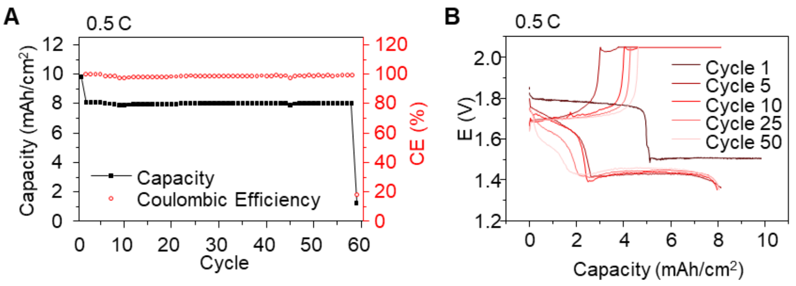

Figure S2.14 The cycling of the battery at the rate of 0.5 C. The electrolyte with the concentration of 36.5% and the capacity range of 50% was used.

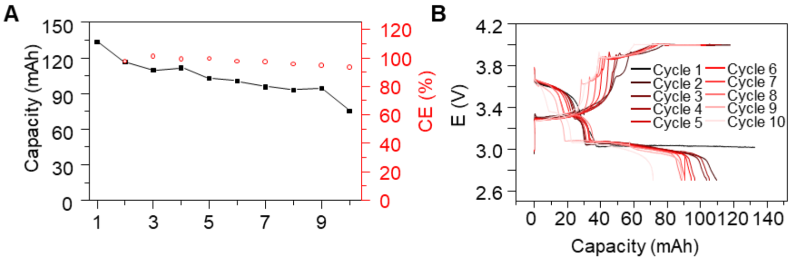

Figure S2.15 | The cycling of two 8-layer 2 × 2 cm^2 battery connected in series at the rate of 0.05 C.

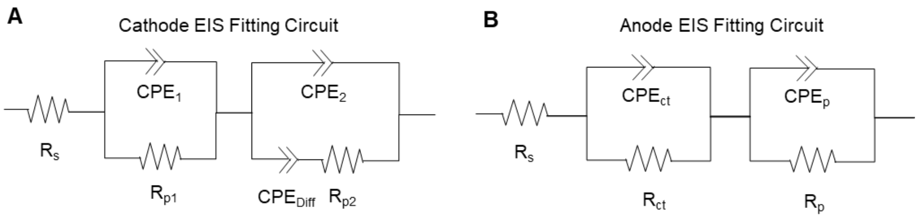

Figure S2.16 | The equivalent circuit used for the (a) cathode and (b) anode EIS fitting.

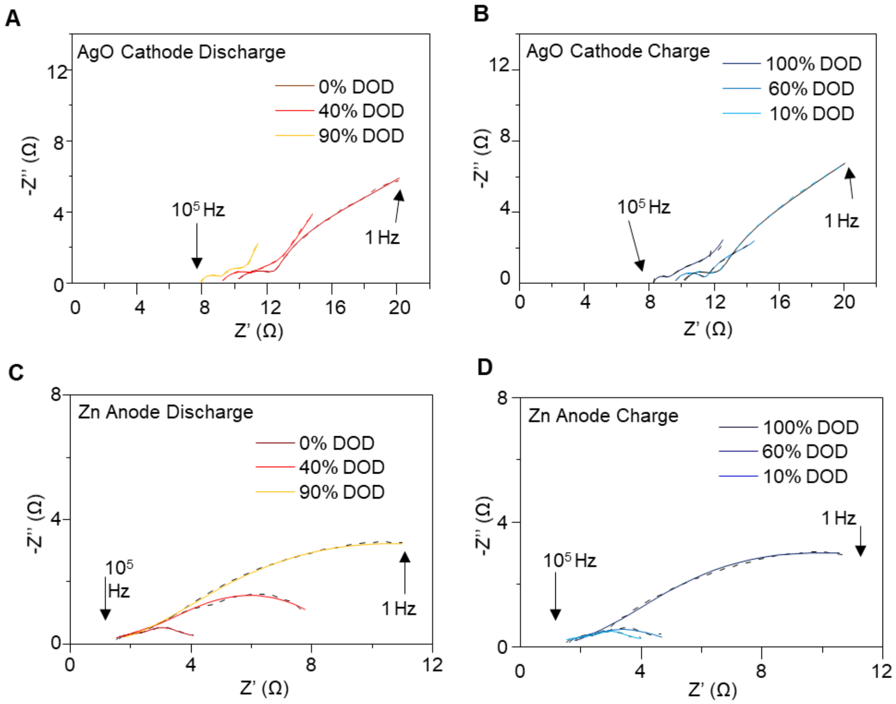

Figure S2.17 | The Nyquist plot and the EIS fitting of the cathode during the 5th cycle (a) discharging and (b) charging, and the corresponding anode (c) charging and (d) discharging.

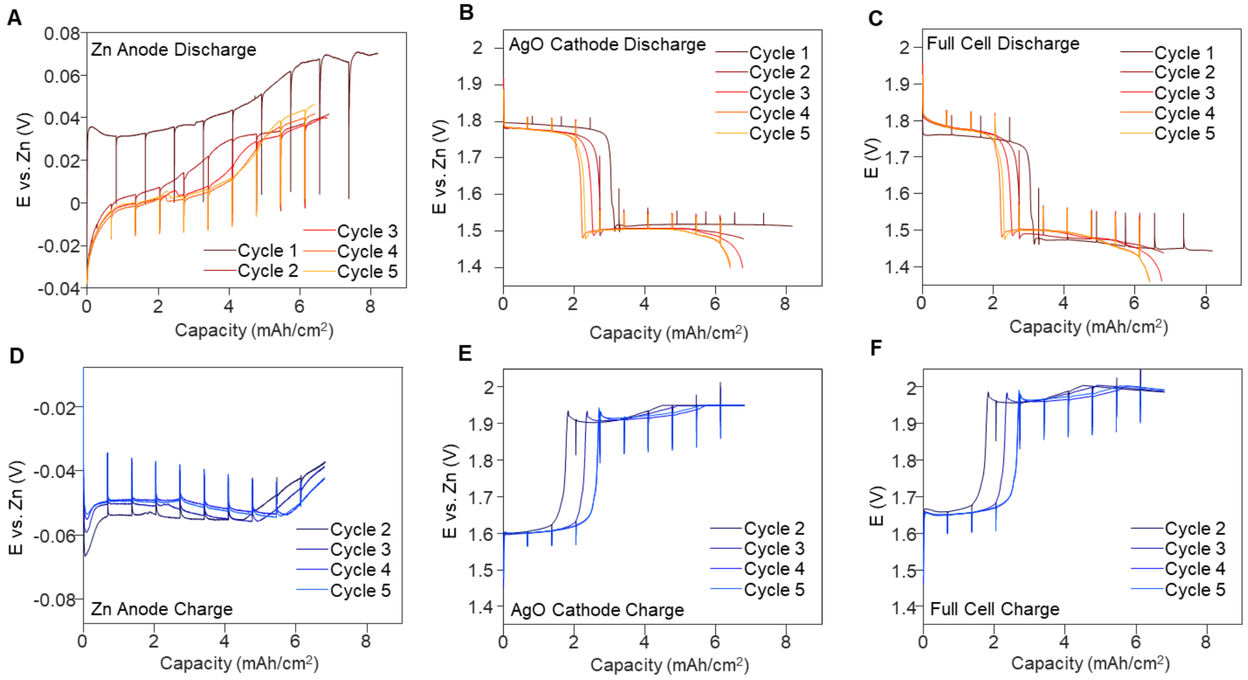

Figure S2.18 | The potential profile of the anode (a,d) and cathode (b,e) vs. Zn reference and the full cell (c, f) within the first 5 cycles of (a-d) discharging and (d-f) corresponding 4 cycles of charging. The vertical lines correspond to the places where an EIS measurements were taken.

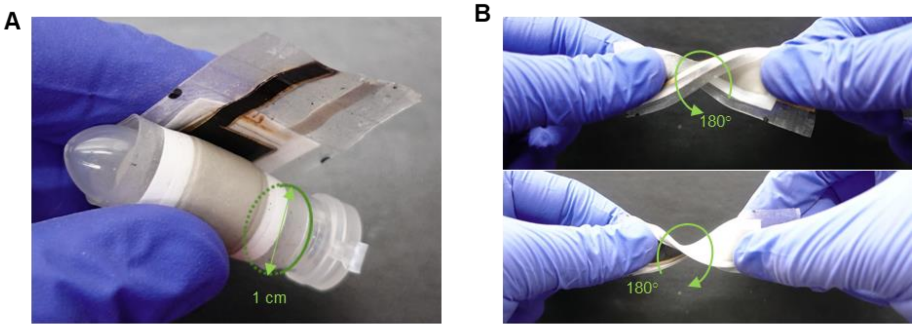

Figure S2.19 | Additional images illustrating the manual bending and twisting of the battery. (a) A tube with diameter of 1 cm was used to bend the battery for half and one entire round. (b) The battery was twisted counterclockwise and clockwise 180° which add up to a total of 360°.

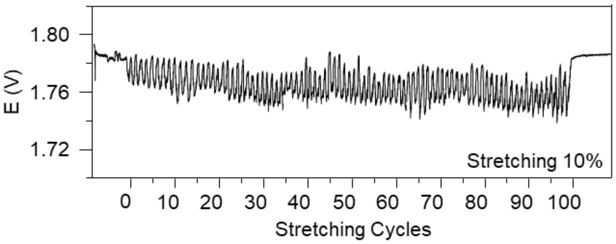

Figure S2.20 | The voltage profile of the 1 × 5 cm^2 battery during 1 mA discharge while undergoing 100 cycles of 10 % lengthwise stretching. Although the battery was not optimized for stretchability, a certain amount of stretchability is required for the battery to endure low-radius bending and accommodate for the outer-layer strain.

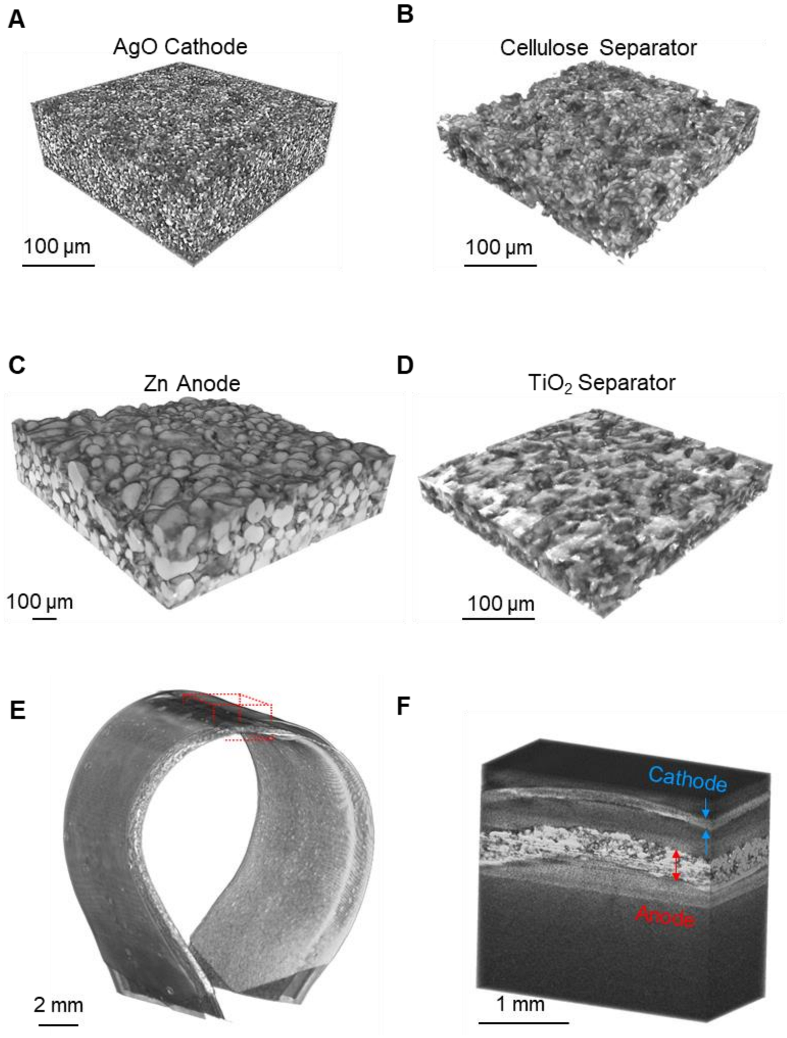

Figure S2.21 | Additional microscopic 3D images of the (A) cathode, (B) cellulose separator, (C) anode, and (D) TiO$_2$ separator generated using the micro-CT. (E) the 3D image of the bent 1 × 5 cm^2 battery in a different angle and (F) the zoomed-in view of the top of the cell showing no cracking nor delamination between the layers.

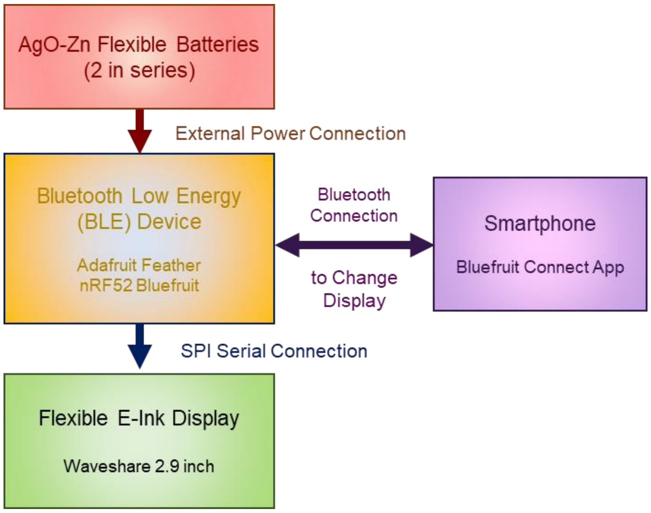

Figure S2.22 | The system diagram of the assembled flexible E-ink display system.

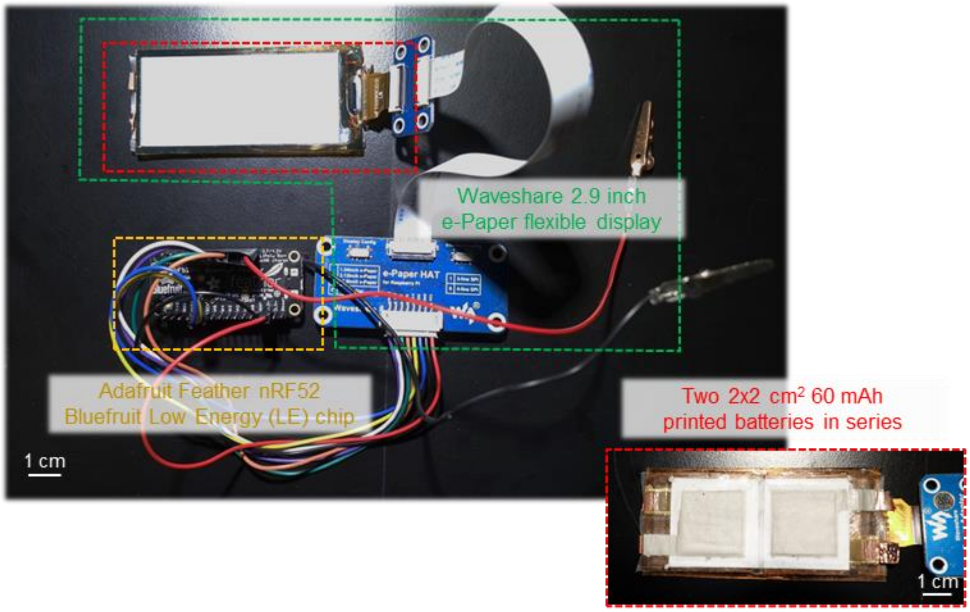

Figure S2.23 | The photo of the assembled flexible E-ink display system with 2 batteries attached to the backside of the display panel.

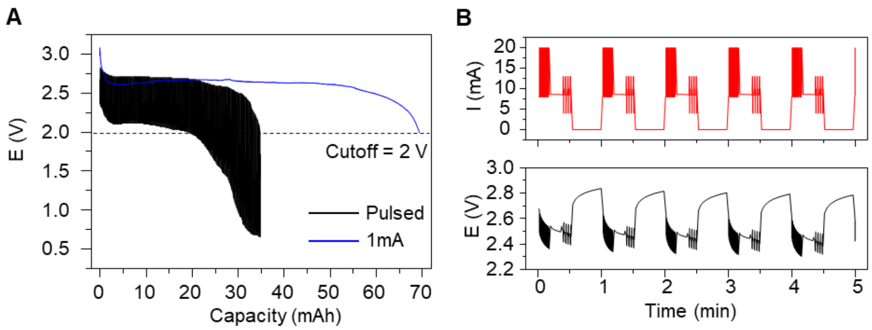

Figure S2.24 | (a) The discharge curve of a CR1620 Lithium coin cell battery rated at 68 mAh nominal capacity under continuous 1 mA discharge and pulsed discharge.[20] Significant capacity fade is observed for the battery with pulsed discharge. (b) Zoomed in view of the current and voltage change of the CR1620 battery.

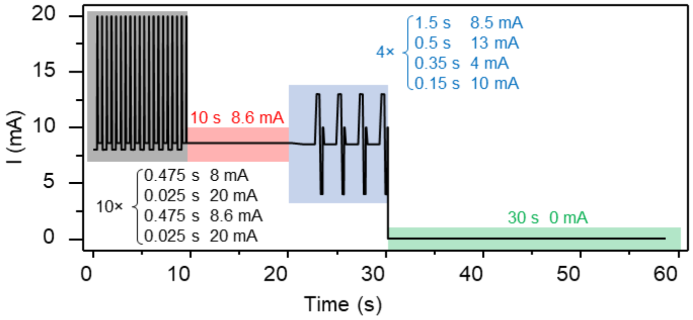

Figure S 2.25 | The detailed breakdown of the pulsed discharge profile.

2.6.3 Supplementary Videos

Video S2.1 | Repeated bending of a 1 × 5 cm^2 printed battery using a linear motor. (5x speed)

Video S2.2 | The powering of the flexible E-ink display system using two printed battery connected in series.

Video S2.3 | The powering of an LED bulb using a 1 × 5 cm^2 battery during various deformations.

Video S2.4 | Low resolution micro-CT scan of the bent 1 × 5 cm^2 battery.

Video S2.5 | High resolution micro-CT scan of a zoomed-in segment of the bent 1 × 5 cm^2 battery.

2.6.4 Supplementary References

1. Wang, S.J., Meng, Y.S., Shin, J., You, J.-M., Lee, J.Z., Kumar, R., Yin, L., Wang, J., and Meng, S. (2016). Deposition of ZnO on bismuth species towards a rechargeable Zn-based aqueous battery. Phys. Chem. Chem. Phys 18, 26376–26382.

2. Kumar, R., Shin, J., Yin, L., You, J.-M., Meng, Y.S., and Wang, J. (2017). All-Printed, Stretchable Zn-Ag2O Rechargeable Battery via Hyperelastic Binder for Self-Powering Wearable Electronics. Advanced Energy Materials 7, 1602096.

3. Braam, K.T., Volkman, S.K., and Subramanian, V. (2012). Characterization and optimization of a printed, primary silver–zinc battery. Journal of Power Sources 199, 367–372.

4. Berchmans, S., Bandodkar, A.J., Jia, W., Ramírez, J., Meng, Y.S., and Wang, J. (2014). An epidermal alkaline rechargeable Ag–Zn printable tattoo battery for wearable electronics. J. Mater. Chem. A 2, 15788–15795.

5. Kettlgruber, G., Kaltenbrunner, M., Siket, C.M., Moser, R., Graz, I.M., Schwödiauer, R., and Bauer, S. (2013). Intrinsically stretchable and rechargeable batteries for self-powered stretchable electronics. J. Mater. Chem. A 1, 5505–5508.

6. Winslow, R., Wu, C.H., Wang, Z., Kim, B., Keif, M., Evans, J., and Wright, P. (2013). Development and manufacture of printable next-generation gel polymer ionic liquid electrolyte for Zn/MnO2batteries. J. Phys.: Conf. Ser. 476, 012085.

7. Yan, C., Wang, X., Cui, M., Wang, J., Kang, W., Foo, C.Y., and Lee, P.S. (2014). Stretchable Silver-Zinc Batteries Based on Embedded Nanowire Elastic Conductors. Advanced Energy Materials 4, 1301396.

8. Gaikwad, A.M., Whiting, G.L., Steingart, D.A., and Arias, A.C. (2011). Highly Flexible, Printed Alkaline Batteries Based on Mesh-Embedded Electrodes. Advanced Materials 23, 3251–3255.

9. Braam, K., and Subramanian, V. (2015). A Stencil Printed, High Energy Density Silver Oxide Battery Using a Novel Photopolymerizable Poly(acrylic acid) Separator. Advanced Materials 27, 689–694.

10. Ho, C.C., Murata, K., Steingart, D.A., Evans, J.W., and Wright, P.K. (2009). A super ink jet printed zinc–silver 3D microbattery. J. Micromech. Microeng. 19, 094013.

11. Gaikwad, A.M., Zamarayeva, A.M., Rousseau, J., Chu, H., Derin, I., and Steingart, D.A. (2012). Highly Stretchable Alkaline Batteries Based on an Embedded Conductive Fabric. Advanced Materials 24, 5071–5076.

12. Sun, K., Wei, T.-S., Ahn, B.Y., Seo, J.Y., Dillon, S.J., and Lewis, J.A. (2013). 3D Printing of Interdigitated Li-Ion Microbattery Architectures. Advanced Materials 25, 4539–4543.

13. Hilder, M., Winther-Jensen, B., and Clark, N.B. (2009). Paper-based, printed zinc–air battery. Journal of Power Sources 194, 1135–1141.

14. Kumar, R., Johnson, K.M., Williams, N.X., and Subramanian, V. (2019). Scaling Printable Zn–Ag2O Batteries for Integrated Electronics. Advanced Energy Materials 9, 1803645.

15. Park, S.-H., King, P.J., Tian, R., Boland, C.S., Coelho, J., Zhang, C. (John), McBean, P., McEvoy, N., Kremer, M.P., Daly, D., et al. (2019). High areal capacity battery electrodes enabled by segregated nanotube networks. Nature Energy 4, 560–567.

16. Blue Spark Battery Products https://www.bluesparktechnologies.com/index.php/products-and-services/battery-products/ultra-thin-series.

17. Enfucell Soft Battery Data Sheet https://asiakas.kotisivukone.com/files/enfucell.kotisivukone.com/Dokumentit/Enfucell_SoftBattery_specifications_2019-05-15.pdf.

18. Imprint Energy ZincPoly 8349 Battery Specification https://www.imprintenergy.com/s/Imprint-Energy-ZincPoly-8349-Battery-Datasheet-Rev22.pdf.

19. BrightVolt 452229-14XT Data SHeet https://www.brightvolt.com/wp-content/uploads/2018/06/452229-14XT.pdf.

20. Renata CR1620 Li Battery Data Sheet https://www.renata.com/fileadmin/downloads/productsheets/lithium/3V_lithium/CR1620.pdf

2.7 References

1. Gong, S., and Cheng, W. (2017). Toward Soft Skin-Like Wearable and Implantable Energy Devices. Advanced Energy Materials 7, 1700648.

2. Ray, T.R., Choi, J., Bandodkar, A.J., Krishnan, S., Gutruf, P., Tian, L., Ghaffari, R., and Rogers, J.A. (2019). Bio-Integrated Wearable Systems: A Comprehensive Review. Chem. Rev. 119, 5461–5533.

3. Yin, L., Seo, J.K., Kurniawan, J., Kumar, R., Lv, J., Xie, L., Liu, X., Xu, S., Meng, Y.S., and Wang, J. (2018). Highly Stable Battery Pack via Insulated, Reinforced, Buckling-Enabled Interconnect Array. Small 14, 1800938.

4. Xu, S., Zhang, Y., Cho, J., Lee, J., Huang, X., Jia, L., Fan, J.A., Su, Y., Su, J., Zhang, H., et al. (2013). Stretchable batteries with self-similar serpentine interconnects and integrated wireless recharging systems. Nature Communications 4, 1543.

5. Weng, W., Sun, Q., Zhang, Y., He, S., Wu, Q., Deng, J., Fang, X., Guan, G., Ren, J., and Peng, H. (2015). A Gum-Like Lithium-Ion Battery Based on a Novel Arched Structure. Advanced Materials 27, 1363–1369.

6. Huang, Y., Ip, W.S., Lau, Y.Y., Sun, J., Zeng, J., Yeung, N.S.S., Ng, W.S., Li, H., Pei, Z., Xue, Q., et al. (2017). Weavable, Conductive Yarn-Based NiCo//Zn Textile Battery with High Energy Density and Rate Capability. ACS Nano 11, 8953–8961.

7. Gaikwad, A.M., Zamarayeva, A.M., Rousseau, J., Chu, H., Derin, I., and Steingart, D.A. (2012). Highly Stretchable Alkaline Batteries Based on an Embedded Conductive Fabric. Advanced Materials 24, 5071–5076.

8. Zamarayeva, A.M., Gaikwad, A.M., Deckman, I., Wang, M., Khau, B., Steingart, D.A., and Arias, A.C. (2016). Fabrication of a High-Performance Flexible Silver–Zinc Wire Battery. Advanced Electronic Materials 2, 1500296.

9. Li, H., Liu, Z., Liang, G., Huang, Y., Huang, Y., Zhu, M., Pei, Z., Xue, Q., Tang, Z., Wang, Y., et al. (2018). Waterproof and Tailorable Elastic Rechargeable Yarn Zinc Ion Batteries by a Cross-Linked Polyacrylamide Electrolyte. ACS Nano 12, 3140–3148.

10. Kumar, R., Shin, J., Yin, L., You, J.M., Meng, Y.S., and Wang, J. (2017). All-Printed, Stretchable Zn-Ag2O Rechargeable Battery via Hyperelastic Binder for Self-Powering Wearable Electronics. Advanced Energy Materials 7, 1602096.

11. Liu, W., Chen, Z., Zhou, G., Sun, Y., Lee, H.R., Liu, C., Yao, H., Bao, Z., and Cui, Y. (2016). 3D Porous Sponge-Inspired Electrode for Stretchable Lithium-Ion Batteries. Advanced Materials 28, 3578–3583.

12. Mackanic, D.G., Yan, X., Zhang, Q., Matsuhisa, N., Yu, Z., Jiang, Y., Manika, T., Lopez, J., Yan, H., Liu, K., et al. (2019). Decoupling of mechanical properties and ionic conductivity in supramolecular lithium ion conductors. Nature Communications 10, 5384.

13. G. Mackanic, D., Chang, T.-H., Huang, Z., Cui, Y., and Bao, Z. (2020). Stretchable electrochemical energy storage devices. Chemical Society Reviews.

14. Kaltenbrunner, M., Kettlgruber, G., Siket, C., Schwödiauer, R., and Bauer, S. (2010). Arrays of Ultracompliant Electrochemical Dry Gel Cells for Stretchable Electronics. Advanced Materials 22, 2065–2067.

15. Li, H., Han, C., Huang, Y., Huang, Y., Zhu, M., Pei, Z., Xue, Q., Wang, Z., Liu, Z., Tang, Z., et al. (2018). An extremely safe and wearable solid-state zinc ion battery based on a hierarchical structured polymer electrolyte. Energy & Environmental Science 11, 941–951.

16. Song, W.-J., Lee, S., Song, G., and Park, S. (2019). Stretchable Aqueous Batteries: Progress and Prospects. ACS Energy Letters 4, 177–186.

17. Ma, L., Chen, S., Wang, D., Yang, Q., Mo, F., Liang, G., Li, N., Zhang, H., Zapien, J.A., and Zhi, C. (2019). Super-Stretchable Zinc–Air Batteries Based on an Alkaline-Tolerant Dual-Network Hydrogel Electrolyte. Advanced Energy Materials 9, 1803046.

18. Kim, J., Kumar, R., Bandodkar, A.J., and Wang, J. (2017). Advanced Materials for Printed Wearable Electrochemical Devices: A Review. Advanced Electronic Materials 3, 1600260.

19. Lanceros-Méndez, S., and Costa, C.M. (2018). Printed Batteries: Materials, Technologies and Applications (John Wiley & Sons).

20. Pan, H., Shao, Y., Yan, P., Cheng, Y., Han, K.S., Nie, Z., Wang, C., Yang, J., Li, X., Bhattacharya, P., et al. (2016). Reversible aqueous zinc/manganese oxide energy storage from conversion reactions. Nature Energy 1, 16039.

21. Lee, J.-S., Tai Kim, S., Cao, R., Choi, N.-S., Liu, M., Lee, K.T., and Cho, J. (2011). Metal-Air Batteries with High Energy Density: Li-Air versus Zn-Air. Advanced Energy Materials 1, 34–50.

22. Zeng, Y., Zhang, X., Meng, Y., Yu, M., Yi, J., Wu, Y., Lu, X., and Tong, Y. (2017). Achieving Ultrahigh Energy Density and Long Durability in a Flexible Rechargeable Quasi-Solid-State Zn–MnO2 Battery. Advanced Materials 29.

23. Li, Y., Fu, J., Zhong, C., Wu, T., Chen, Z., Hu, W., Amine, K., and Lu, J. (2019). Recent Advances in Flexible Zinc-Based Rechargeable Batteries. Advanced Energy Materials 9, 1802605.

24. Yan, C., Wang, X., Cui, M., Wang, J., Kang, W., Foo, C.Y., and Lee, P.S. (2014). Stretchable Silver-Zinc Batteries Based on Embedded Nanowire Elastic Conductors. Advanced Energy Materials 4, 1301396.

25. Venkatraman, M., and Van Zee, J.W. (2007). A model for the silver–zinc battery during high rates of discharge. Journal of Power Sources 166, 537–548.

26. Bonk, J.F., and Garrett, A.B. (1959). A Study of the Silver (I) Oxide-Silver (II) Oxide Electrode. J. Electrochem. Soc. 106, 612.

27. Takeda, K., and Hattori, T. (1999). Optimal Process for Fabricating AgO Cathode for AgO/Zn Cells Improved in High Drain Pulse Performance at Low Temperatures. J. Electrochem. Soc. 146, 3190.

28. Parkhurst, W.A. (1984). Thermogravimetry-Evolved Gas Analysis of Silver Oxide Cathode Material. Journal of The Electrochemical Society 131, 1739.

29. Wang, S.J., Meng, Y.S., Shin, J., You, J.-M., Lee, J.Z., Kumar, R., Yin, L., Wang, J., and Meng, S. (2016). Deposition of ZnO on bismuth species towards a rechargeable Zn-based aqueous battery. Phys. Chem. Chem. Phys 18, 26376–26382.

30. Xu, W., Wang, S.Q., Zhang, Q.Y., Ma, C.Y., Wang, Q., Wen, D.H., and Li, X.N. (2019). Hierarchically structured AgO films with nano-porosity for photocatalyst and all solid-state thin film battery. Journal of Alloys and Compounds 802, 210–216.

31. McMillan, J.A. (1962). Higher Oxidation States of Silver. Chem. Rev. 62, 65–80.

32. Kumar, R., Johnson, K.M., Williams, N.X., and Subramanian, V. (2019). Scaling Printable Zn–Ag2O Batteries for Integrated Electronics. Advanced Energy Materials 9, 1803645.

33. Braam, K., and Subramanian, V. (2015). A Stencil Printed, High Energy Density Silver Oxide Battery Using a Novel Photopolymerizable Poly(acrylic acid) Separator. Advanced Materials 27, 689–694.

34. Choi, K.H., Ahn, D.B., and Lee, S.Y. (2018). Current Status and Challenges in Printed Batteries: Toward Form Factor-Free, Monolithic Integrated Power Sources. ACS Energy Letters 3.

35. Entezam, M., Poormadadkar, H., Khonakdar, H.A., and Jafari, S.H. (2020). Melt rheology and interfacial properties of binary and ternary blends of PS, EOC, and SEBS. Journal of Applied Polymer Science 137, 48791.

36. Turney, D.E., Gallaway, J.W., Yadav, G.G., Ramirez, R., Nyce, M., Banerjee, S., Chen-Wiegart, Y.C.K., Wang, J., D'Ambrose, M.J., Kolhekar, S., et al. (2017). Rechargeable Zinc Alkaline Anodes for Long-Cycle Energy Storage. Chemistry of Materials 29.

37. Mainar, A.R., Leonet, O., Bengoechea, M., Boyano, I., Meatza, I. de, Kvasha, A., Guerfi, A., and Blázquez, J.A. (2016). Alkaline aqueous electrolytes for secondary zinc–air batteries: an overview. International Journal of Energy Research 40, 1032–1049.

38. Braam, K.T., Volkman, S.K., and Subramanian, V. (2012). Characterization and optimization of a printed, primary silver–zinc battery. Journal of Power Sources 199, 367–372.

39. Bandodkar, A.J., Hung, V.W.S., Jia, W., Valdés-Ramírez, G., Windmiller, J.R., Martinez, A.G., Ramírez, J., Chan, G., Kerman, K., and Wang, J. (2013). Tattoo-based potentiometric ion-selective sensors for epidermal pH monitoring. Analyst 138, 123–128.

40. Yin, L., Kumar, R., Karajic, A., Xie, L., You, J., Joshuia, D., Lopez, C.S., Miller, J., and Wang, J. (2018). From All-Printed 2D Patterns to Free-Standing 3D Structures: Controlled Buckling and Selective Bonding. Advanced Materials Technologies 3, 1800013.

41. Dellis, J.-L. Zfit. https://www.mathworks.com/matlabcentral/fileexchange/19460-zfit.

42. D'Errico, J. fminsearchbnd, fminsearchcon. https://www.mathworks.com/matlabcentral/fileexchange/8277-fminsearchbnd-fminsearchcon.

43. Rustomji, C.S., Mac, J., Choi, C., Kim, T.K., Choi, D., Meng, Y.S., and Jin, S. (2016). Thin-film electrochemical sensor electrode for rapid evaluation of electrolytic conductivity, cyclic voltammetry, and temperature measurements. J Appl Electrochem 46, 59–67.

Chapter 3. Nano and Micro-scale X-ray Tomography for Battery Research

X-ray Computed Tomography (X-Ray CT) is a well-known non-destructive imaging technique where contrast originates from the materials' absorption coefficients. Novel battery characterization studies on increasingly challenging samples have been enabled by the rapid development of both synchrotron and laboratory-scale imaging systems as well as innovative analysis techniques. Furthermore, the recent development of the laboratory nano-scale CT (NanoCT) system has pushed the limits of battery material imaging towards voxel sizes previously achievable only using synchrotron facilities. Such systems are now able to reach spatial resolutions down to 50 nm. Given the non-destructive nature of CT, *in-situ* and *operando* studies have emerged as powerful methods to quantify morphological parameters, such as the tortuosity factor, porosity, surface area, and volume expansion during battery operation or cycling. Combined with powerful Artificial Intelligence (AI)/Machine Learning (ML) analysis techniques, extracted 3D tomograms and battery-specific morphological parameters enable the development of predictive physics-based models that can provide valuable insights for battery engineering. Such models can predict the impact of the electrode microstructure on cell performances or analyze the influence of material heterogeneities on electrochemical responses. In this work, we review the increasing role of X-ray CT experimentation in the battery field, discuss the incorporation of AI/ML in analysis, and provide a perspective on how the combination of multi-scale CT imaging techniques can expand the development of predictive multiscale battery behavioral models.

3.6 A Brief History of X-Ray Computed Tomography

3.6.1 Introduction

X-ray Computed Tomography (X-ray CT) is well known in the medical and scientific research communities as a non-destructive imaging technique where contrast originates from the materials' absorption coefficients[1]. The attenuated X-Ray beam due to the sample interaction is collected, converted, and reconstructed with sophisticated algorithms to produce cross-sectional and 3-dimensional images. The resultant data provides valuable non-invasive information about a sample's morphology and internal structure. In the medical field, CT has led to countless discoveries and treatments that have greatly impacted the health of populations[2]. In the past 2 decades, the impact of CT has expanded outside the medical field to general metrology [3,4], and has considerably impacted the development of battery systems and other electrochemical devices[5,6]. With CT technology rapidly improving, commercial lab-based systems are now able to achieve similar resolutions to high brilliance synchrotron beamlines.

However, with the increasing resolutions and applications of CT in electrochemical fields, more complex datasets are being explored, motivating the need for advanced analysis techniques to fully harness detailed insights about samples. This led to the recent leveraging of Artificial Intelligence (AI) and Machine Learning (ML) to assist the segmentation of complex datasets, or to act as a bridge between experimental data and multi-physics/multi-scale modeling[7–9]. As such, AI and ML have proved to be valuable tools to significantly reduce the time necessary to process large CT datasets while precisely labelling features of interest. In this review, we explore the larger outlook of X-ray CT in the battery field and discuss how AI and ML can impact data analysis, simulation, and modeling.

3.6.2 Development of X-Ray Computed Tomography

The mathematical principles of computed tomography (CT) were first developed in 1917 by Johann Radon[10] only a few decades after the discovery of the X-ray[11,12]. Due to the complexity of the equations, it wasn't until 1963 that Allan Cormack leveraged Fourier transforms to allow for practical applications[13]. Less than a decade later in 1971, Sir Godfrey Hounsfield performed the first patient brain CT scan[14–16]. Since then, CT has evolved from a technique primarily used in the medical community to a tool widely used across multiple disciplines in the scientific and engineering world[5,17]. To track the development of CT, **Figure 3.1** showcases the year of publication vs. the reported voxel size for works in the medical and electrochemical storage fields[18–20]. Here, a voxel is a 3D representation of a 2D pixel and corresponds to the smallest cube of information obtained from a scan. The spatial resolution is often thought of as at least two to three times the voxel size and can be larger due to blurring and imaging artifacts that impede the distinction of fine features.

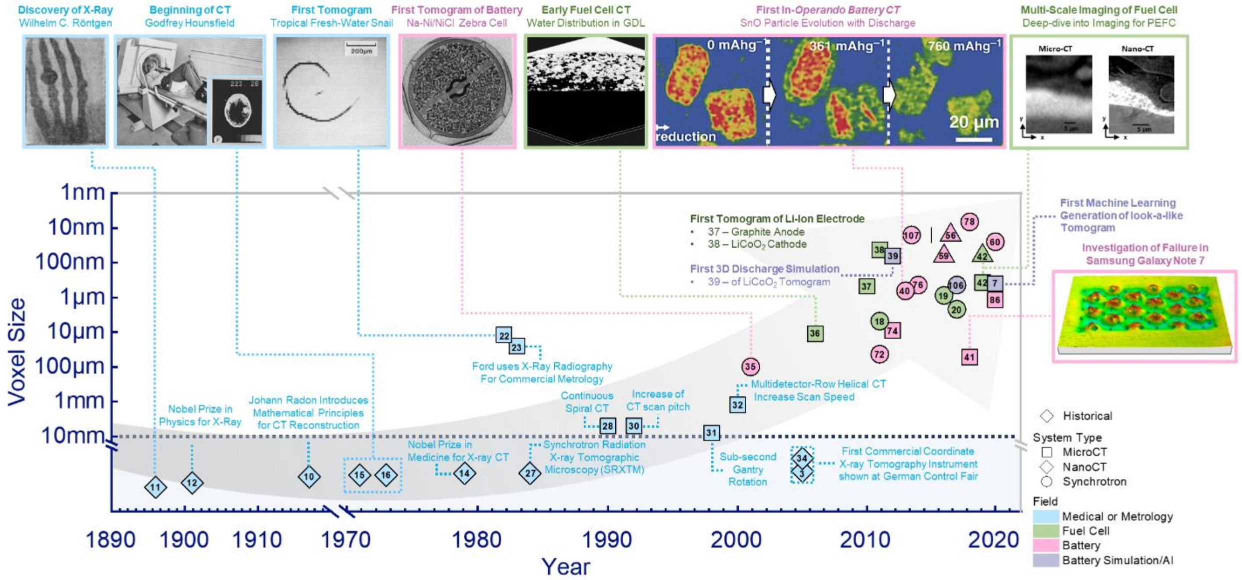

Figure 3.1 | History and trends of computed tomography. Notable advancements in X-ray CT showing the trend of decreasing tomogram voxel size with time. Colors represent the various fields works are related to: Medical (blue), Fuel Cell (Green), Battery (Pink), and Battery Simulation (Purple). Marker shapes indicate historical advancements (♦) and works pertaining to MicroCT (■), synchrotron (●), and NanoCT (▲) systems. Markers below the dotted line are notable CT-related events or works where voxel sizes are not reported.

In the early 1980s, CT started to gain traction outside the medical field in the broader scientific and industry community, and in 1982, the first *micro*-tomogram was taken of a freshwater snail with a 12 μm voxel size[21,22]. In 1983, Ford reported the first industry application of an in-house built microscale CT (MicroCT) system where they distinguished features of ceramic fixtures with a spatial resolution of 25 μm[17,23]. In the same year Grodzins *et al.*[24–26] proposed the theoretical principles of utilizing *synchrotron-sourced* radiation to provide enhanced contrast and resolution for CT, and in 1984, Thomson *et al.* reported the first synchrotron radiation X-ray tomographic microscopy (SRXTM) measurement[27].

Meanwhile, the biomedical community was less focused on achieving higher resolutions but working on imaging large organs and tissues of patients with increased speed and accuracy. Through the 1980s, measurements were taken with a slow step-and-shoot approach, where the gantry (containing the x-ray tube, collimators, and detectors) rotates 360° around a stationary examination table and then incrementally shifts to the next acquisition region[2]. It wasn't until the early 1990s that continuous gantry rotation and spiral or helical CT made quicker scan times possible[2,28]. In this case, the gantry moves helically and continuously around the patient and the moving table. With this method, CT achieved acquisition speeds sufficient to scan an entire abdomen in a single breath[29]. The focus was then shifted to increasing the gantry rotation speed and scan pitch (table feed speed per beam width)[30], with sub-second gantry rotation achieved in the late 1990s[31]. Following this development, multidetector rows were implemented to increase the area of acquisition for a single rotation, decreasing the scan time further[32]. The number of detectors kept increasing throughout the years with present-day medical CT systems typically having more than 2000 detectors in each row[33].

3.6.3 CT Deployment in Electrochemical Device Characterization

CT systems used in metrology benefited greatly from the improvements in speed and detection developed by medical CT. However, it wasn't until 2005 that the first CT machine dedicated to metrology and industrial applications was introduced[3,34]; the first micro-tomograms of a battery[5,35] and fuel cell[6,36] were reported in the literature in 2001 and 2006 respectively. As shown in **Figure 3.1**, numerous CT works in the electrochemical field began to emerge shortly after the commercialization of this tool. In the early 2010s, the first tomograms of a Li-ion battery positive and negative electrode were reported, illustrating the capability of distinguishing the active material ($LiCoO_2$) from an inactive phase[37,38]. The first 3D discharge simulation based on tomography images quickly followed in 2012[39].

Further development allowed for novel and more creative studies to be performed: in 2013, Ebner *et al.* performed the first *operando* battery CT experiment to visualize and quantify the electrochemical and mechanical evolution of SnO particles in a Li-ion battery electrode[5,40]. In 2018, Loveridge *et al*. used X-ray CT to identify the failure mechanism in the Galaxy Note 7 which were recalled due to battery explosions[41]. The reconstructed tomograms in this work revealed defects in the positive tab welding area that resulted in electrical shorts, leading to a thermal runaway. This example illustrates the usefulness of CT and the incentive of the recent efforts toward multi-scale imaging by the electrochemical community[42]. Finally, an increasing number of works are now leveraging AI and ML, for instance for imitating *in silico* electrode tomograms similar to experimental CT[7].

3.6.4 Present Day Capabilities: Lab-based and Synchrotron Sources

For research in material science, both lab-based and synchrotron facilities have made great advancements over the past decade. In 2014, Maire and Withers wrote a review[43] on quantitative X-ray tomography where they outlined how X-ray CT data was no longer only used for qualitative insights but increasingly for quantitative analysis of material properties. This transition from qualitative to quantitative only accelerated since 2014, as imaging capabilities facilitate greater spatial and temporal resolutions. Lab-based X-ray CT systems now routinely achieve 1 µm or less resolutions, with specialized systems able to achieve resolutions as low as 10’s of nm[44]. This multi-length scale capability for lab-based systems allows for ex-situ imaging of structural properties from 10’s of nm to mm[44,45].

Recently, laboratory CT systems have enabled dual or tri-energy imaging via multiple quasi-monochromatic beam energies[46]. Software packages have been developed to extract the best detail from images taken at the different energies. For example, images taken with lower energies may have enhanced resolution and sharpness for materials consisting of low atomic mass elements. This software framework that combines images taken at multiple energies follows the trajectory of advancing correlative workflows between different microscopy methods. The strengths of individual techniques are leveraged in combined datasets that provide heighted resolution or larger sample sizes. The temporal resolution of laboratory sources has also shown tremendous progress over the past decade but remains insufficient for many *operando* and *in-situ* analyses of structural dynamics in the range of minutes to hours. Synchrotron sources are also rapidly evolving, with major synchrotrons, such as the National Synchrotron Light Source (NSLS) II, Advanced Photon Source (APS), and the European Synchrotron Radiation Facility (ESRF) having completed or planned upgrades for increased photon flux density and coherence for faster imaging and greater sensitivity. For example, the ESRF's Extremely Brilliant Source (EBS) is expected to present 100 times its previous brilliance and coherence, facilitating new opportunities for high energy and high spatial- and temporal resolution imaging[47]. Synchrotron sources are now achieving tomograms with voxel sizes of 20 to 50 nm in under 1 hour[48,49]. This evolution of both laboratory- and synchrotron-based capabilities has continued to present new opportunities for understanding the highly dynamic behavior of electrochemical energy devices. For consistency, in the following we refer to 3D tomographic data collected at synchrotron facilities by scanning transmission X-ray microscopy (STXM) or transmission X-ray tomography (TXM) as synchrotron radiation X-ray tomographic microscopy (SRXTM)[48,49].

3.7 X-Ray CT in the Battery Field

While several tools are already routinely used to characterize the morphology of electrochemical devices, X-ray CT present significant advantages compared to these. Indeed, Focused Ion Beam-Scanning Electron Microscopy (FIB-SEM), Transmission Electron Microscopy (TEM), and Secondary Ion Mass Spectrometry (SIMS) all require a vacuum, making *in-situ* and *operando* studies difficult if not impossible for most battery systems. Moreover, 3D reconstruction requires destructive milling of samples. A more detailed explanation of the information that can be gathered using these tools is presented in the supplementary materials (Section 1.1). In comparison, X-ray CT is non-destructive and does not require a vacuum for high resolution imaging, making it ideal for evaluating morphological changes *in-situ* or *operando* in practical battery systems. CT can also be used to distinguish and segment species based on the varying X-ray absorption, thus allowing for select materials to be studied dynamically.

3.7.1 Materials CT Parameters

To understand the usefulness of CT in battery research, it is important to know the information and morphological parameters that it can provide. Reconstructed volumes can showcase device architecture, such as by Yin and Scharf *et al.*, who demonstrated uniform electrode contact when flexing a printed Zn-AgO battery[50]. Moreover, many morphological parameters can also be extracted, providing powerful insights into electrode structure and performance. Surface area and volume information are commonly used in battery research to analyze electrodes and are the most intuitive to observe and quantify from reconstructed volumes. Surface area measurements can showcase electrode wettability, while volumetric analysis can determine the thickness variation and expansion during battery operation. In the first *operando* battery CT study, Ebner *et al.* showcased the volume expansion of a SnO electrode as it was lithiated[40]. During reduction, the repeated measurements using SRXTM revealed a 250% volume expansion due to lithiation that was only partially recovered during oxidation. The thickness and the position of the solid-electrolyte interface was also quantified and observed increasing as a function of lithiation.

CT volume extraction has also proven particularly useful for silicon anode batteries[51–53] in the detection of volume expansion due to lithiation (up to 280% for $Li_{15}Si_4$)[54], which is one of the main limitations hindering cycle lifetimes. In a 2019 study, *in-situ* SRXTM was used to track the expansion and contraction dynamics of Si electrodes during electrochemical cycling[54]. The thickness variation and changes in the delaminated area were studied, and the micro-sized crack volume fraction was quantified to reveal the failure mechanism in non-maturated electrodes.

Particle analysis can also be performed using CT: through segmentation (See Box 1), particles can be separated, and their individual volumes can be analyzed to provide valuable information about their size and distribution. This type of analysis can be especially useful for *in-situ* or *operando* studies, where the morphological evolution of active material particles can be tracked and analyzed dynamically. For instance, Gent *et al.* studied the heterogeneity of lithiation in secondary particles in causing accelerated capacity fade[55].

Additionally, using NanoCT and Zernlike phase contrast (ZPC), three phases (*e.g.* active material, binder, and pore) can be distinguished in LIB electrodes[56,57]. With a high spatial resolution of 50 nm, Babu *et al.* characterized the particle contact area variation with additives to illustrate the influence on the electrode contact resistance. This can be particularly valuable in quality assurance to study the influence of manufacturing and synthesis conditions on particle morphology. For instance, Heenan *et al.* showed how 5-min long scans with a NanoCT system was sufficient to fully resolve cathode particles and directly quantify the variation in the particle's asymmetry, sphericity, and local surface roughness[58]. This study also quantified the internal voids within individual particles which should be minimized to maximize volumetric energy density.

Similarly, pores and void spaces in battery electrodes can be visualized and quantified with CT. For instance, Frisco *et al*. quantitatively extracted the pore distributions in commercial Li-Ion cells, revealing a collapse of the anode pore structure during cycling in the first investigation of SEI build up using NanoCT[59]. They showed a decrease of more than half the pore volume with cycling, and qualitatively demonstrated with 3D tomograms the SEI build up resulting in increased cell impedance[59]. Similarly, Su *et al.* used *operando* SRXTM to perform the first characterization of Li-O_2 battery cathodes with 3D tomography and extracted the pore distribution using an interconnected pore model for the scanned Li_2O_2 electrode[60]. By using ZPC, they were able to image and distinguish the void spaces from the lighter species like carbon and Li_2O_2 discharge products, successfully extracting nano-sized pores on the order of 100 nm.

CT can also measure the tortuosity or tortuosity factor (square of tortuosity), which can quantify how tortuous an electrode is by analyzing the connection of pores within a structure (See Supporting Section 2.1 for more information on tortuosity). Tortuosity in CT has gained considerable attention in the last decade[7,61,62] and is especially impactful for understanding the transport of electrolyte ions through battery electrodes. For instance, Ebner *et al.* used SRXTM to study the tortuosity anisotropy of three common Li-Ion electrodes with varying porosities to represent various particles shapes, (spherical, triaxial ellipsoidal, and platelet-shaped). They showed that increased geometric tortuosity factor in the plane perpendicular to the current collection can impact the achievable LIB power density and cycling performance and predicted a factor of 4 improvement in the battery discharge rate with platelet-shaped particles in graphite electrodes[63].

3.7.2 Experimental Trends in Battery X-Ray CT

Since the first battery micro-tomogram in 2001[5,35], CT has developed into a versatile technique with various CT system types offering different benefits. Laboratory-scale MicroCT is the most common CT system used in metrology and battery research, due to its large FOV (~130 cm^2 in the XZ direction for large scans), ease of access and use, and relatively high spatial resolution of up to ~500 nm[64–66]. However, even with submicron resolution, MicroCT systems fall short in studying nano-scale phenomena. For this reason, battery researchers turn to SRXTM, with spatial resolutions reported in battery studies reaching as low as 50 nm[67,68]. The main compromises are the beamline time cost, increased sample preparation complexity, and limited FOV. To circumvent this, laboratory-scale NanoCT offers spatial resolutions of up to 50 nm[69], rivaling SRXTM without the necessity of high brilliance synchrotron radiation. However, there are still tradeoffs for each instrument, which should be selected carefully with the experimental goals in mind.

Figure 3.2 shows the trend in FOV, voxel size and scan duration for CT experiments in battery literature[70–83]. As many CT studies do not report the spatial resolution, the FOV was plotted versus the voxel size, since the voxel size scales with and is typically slightly less than half the spatial resolution. As shown, regardless of the battery chemistry, there is a general trend where the FOV decreases with smaller voxel sizes and is dependent on the CT system used. Indeed, in the nano-regime, synchrotron and NanoCT dominates use, while in the micro-regime, MicroCT systems are implemented more often. Additionally, in the nano-regime, NanoCT experiments are *ex-situ* due to the long scan time, and only synchrotron experiments are *in-situ* or *operando*, which illustrates the difficulty in performing dynamic experiments at a limited FOV and long scan times (See **Figure S3.1** for voxel size vs. scan time).

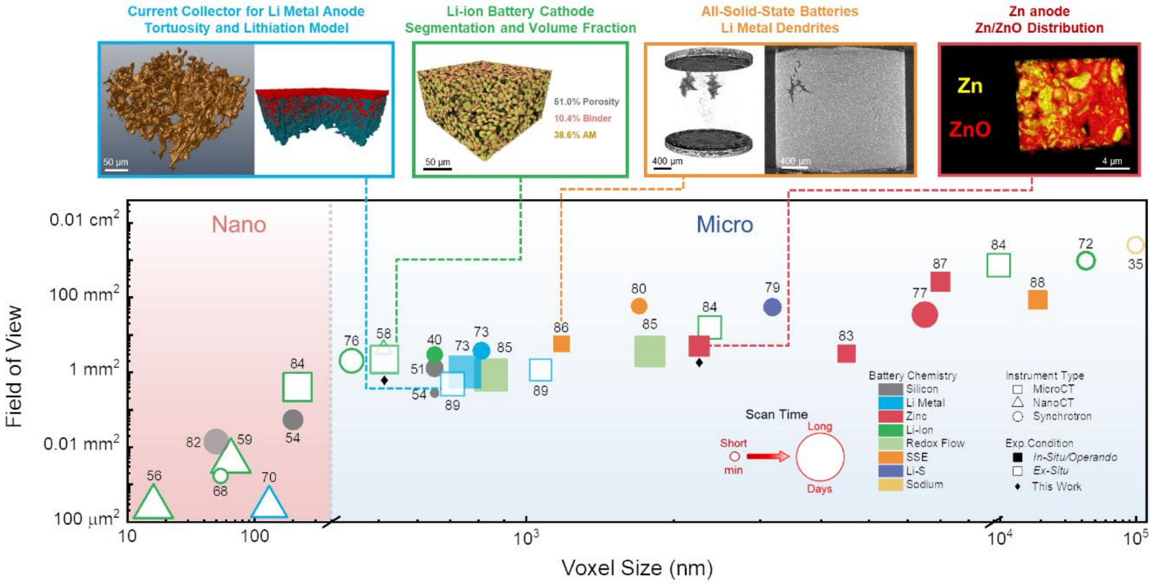

Figure 3.2 | Experimental trends of computed tomography in the battery field. Trend of Field of View (FOV) with Voxel Size and Scan Time for various battery chemistries (colors), CT systems (shape), and experimental conditions (open/filled). Here, the colors represent the battery chemistry, marker size reflects the CT scan time, the filled and hollow markers represent *ex-situ* or *in-situ*/*Operando* experiments respectively, and the marker shapes indicate works pertaining to MicroCT (■), synchrotron (●), and NanoCT (▲) systems.

The battery chemistry of interest also strongly influences the type of instrument used. For instance, since Li is a very light element that weakly interacts with X-rays, it is difficult to image and resolve using traditional MicroCT, which use higher X-ray energies of around 30-160 kV[64,65]. For this reason, Li-Ion battery studies shown with the green markers in **Figure 2.1** in the micro-regime are mainly focused on studying device structures or composite electrodes rather than investigating lithium growth. For instance, Carter *et al.* (84 in **Figure 2.1**) investigated the delamination in a lithium iron phosphate battery and investigated the porosity and the diffusion-based tortuosity factor of the graphite anode structure[84]. They were able to distinguish between graphite, void, and copper, but did not specifically look at Li species. Many studies looking to investigate Li with CT use ZPC with NanoCT or SRXTM systems which can use lower X-ray energies of around 8 keV. However, there are still constraints on the FOV and sample preparation and size for these instruments, which is why Li-ion CT studies, like Frisco *et al.* (59 in **Figure 3.2**)[59] and Kashkooli *et al.* (68 in **Figure 3.2**)[68], tend to be *ex situ*. However, custom *in-situ*/*operando* cells can be developed to help study dynamic phenomena, such as Vanpeene *et al*. (54 in **Figure 3.2**) who used X-ray CT compatible custom Swagelock cells to study volume expansion *in-situ* using SRXTM with a 200 nm voxel size[54].

In the micro-regime, lab-scale MicroCT dominates, and *in-situ* or *operando* experiments are quite common since such experiments tend to elucidate degradation mechanisms and key phenomena in batteries[83,85–88]. For many experiments, micro-sized voxels are small enough to perform novel studies for a variety of battery systems. For instance, shown in the orange in-set of **Figure 3.2**, micro-sized Li-metal dendrites can be resolved in all-solid-state batteries (ASSB)[86]. Micro-sized particles on the scale of 10-100 µm can be easily resolved with MicroCT, such as the case for the Li-ion cathode and Zinc anode in the green and red insets, respectively. Particle analysis can be performed for both chemistries (see **Figure S3.2** and **Figure S3.3**), and *in-situ* studies are even possible as is the case for the Zinc anode. Modeling can also be performed using the reconstructed scans as input. For instance, the blue inset shows a reconstructed porous Cu current collector scanned by MicroCT and a model of the lithiation in the structure, where the porosity and tortuosity can be optimized to maximize cycle life[89].

3.8 CT Analysis, Simulation, and Modelling

Box 1 Artifacts, Filtering, Segmentation, and Workflow

The aim of data analysis in X-ray CT is to obtain the *truest* depiction of the sample or structure analyzed. However, experimental artifacts can distort the X-ray projections, leading to misinterpretations of the resultant data. As such, data containing artifacts can make segmentation challenging, thus disallowing in-depth analysis of complex structures like electrodes. Image noise is one of the most common artifacts and it can be influenced by the exposure rate, beam energy, conical tube diameter, back-projection filter, and magnification[90]. Cupping and streaks or dark bands are two other artifacts that are both due to beam hardening[91–93]. As polychromatic X-rays are used in MicroCT, low energy photons are disproportionately absorbed, and the average energy of the beam increases or *hardens*. This results in cupping where the beam is hardened more through the middle of an object than at the outer edges, and a uniformly dense material will appear non-uniform[91,93]. Streak artifacts or dark bands occur due to differences in material absorption (i.e. heavy elements like Pb, Pt, and Au next to light elements such as Li, C, F), where the beam in one area of the scan is hardened more than in another area[93]. This is especially problematic for LIBs, where light elements such as Li may be near heavier elements, such as Cu. Beam-hardening effects such as these can be partly mitigated experimentally using physical filters that pre-harden the X-ray spectrum to remove low energy photons[91]. More information on other common artifacts such as aliasing and ring artifacts can be found in Section 3.2 of the supporting information.

Most artifact reduction or removal occurs during post-processing, where filtration algorithms can lessen or remove experimental artifacts and smart segmentation methods can be applied to separate out species for further analysis (see supporting Section 3 for pre-processing techniques). Beam hardening can be treated numerically with a low-pass smoothing filter, whereby the smoothed image is used to detect large-scale intensity variations caused by beam hardening, or by a less error-prone iterative approach, which uses sequential histogram-based segmentation with grey value classification to lessen the effects of beam hardening[92,94,95].

Image noise is commonly addressed with a multitude of filtering algorithms[95]. Neighborhood statistical filters consider neighboring voxels grey values and apply a kernel operation, where voxels values are multiplied by a set of weights and then averaged over the sum of the weights to smooth or correct for noisy data[95]. Such filters are differentiated by the type of kernels used, namely mean, median, mode, minimum, maximum and gaussian filters. The median filter, for example, replaces voxel values by the median of a user-defined number of neighboring values. While filters such as these tend to blur the original data, several strategies have been developed to retain particles and pore edges, such as the Non-Local Means (NLM) and Anisotropic Diffusion (AD) filters, and the Unsharp Mask (UM) filter used to improve image contrast. More details on these can be found in Section 3.3 of the supporting information.

In battery electrodes, the three main phases typically observed in an X-ray CT scan are the active material, binder, and pore. A proper segmentation of these is mandatory to ensure the quality of the extracted battery-specific parameters (such as particle size, porosity, and tortuosity). As contrast in X-ray CT is dictated by the material’s X-ray absorption coefficient, the simplest segmentation method is thresholding, differentiating materials based on the numeric grey value distribution[92,96]. With Global Thresholding (GT), the segmentation is performed on the grey-value histogram of an entire 3D dataset. As can be seen in **Figure S3.3**, filtering is a critical step, as it can reveal 3 distinct grey value regions in a Li-ion cathode (corresponding to binder, porosity, and active material), while these were undistinguishable before filtering.

Manual segmentation and GT are nevertheless subject to human error and bias, and therefore a variety of automatic segmentation methods have been developed[92,96]. In contrast to GT, adaptive local segmentation methods account for neighborhood statistics to separate phases in an image. Among the multiple local segmentation methods, Bayesian Markov Random Field, Watershed and Converging Active Contours have been shown to be the most efficient for multiclass segmentation, with tradeoffs specific to each method and sample[92].

Above all, the limiting factor in segmentation is data quality, and it is crucial to have a workflow in which the dataset is optimally acquired and properly filtered to adequately define phases. The workflow can be separated into 3 stages: (1) Preprocessing (artifact removal, filtering, sharpening), (2) Segmentation (global and local thresholding), and (3) Postprocessing (denoising). Denoising algorithms are often used to prepare the dataset for structural analysis. As each stage is interconnected, filters should be chosen with the segmentation method in mind. Moreover, care must be taken as over-filtering can be an issue as well: the mean filter can introduce “unrealistic” values, and filters such as erosion, dilation, and delineation can skew multiclass data[92,97]. Therefore, knowledge of the various filters and segmentation methods is needed to ensure proper extraction of crucial morphological parameters.

3.8.1 Leveraging CT for Computational Modeling

The knowledge and large quantity of information gained from X-ray CT data leads to promising outcomes in the computational modeling of batteries. The Newman's model, a first-generation mathematical model of a lithium-ion battery, was developed in 1993[98,99]. It describes ionic transport in the concentrated electrolyte, lithium transport in the active material, and intercalation electrochemistry at the interface between active material and electrolyte. This model is supported on a 2D cartesian representation of the cell, with an extra polar coordinate dimension for the active material particles (as seen in **Figure 3.3** - Generation I Model) and is therefore also referred to as pseudo-2D (p2D). Since this is a 2D approach, several input parameters are necessary to consider the geometrical features of the electrodes and the cell, such as the separator thicknesses, active material particle size, the active surface area (surface area of contact between active material and electrolyte), the porosity, and tortuosity factor of both electrodes. While some of these morphological parameters (*e.g.* tortuosity factor and active surface area) are challenging to evaluate using experimental techniques[100], the stochastic generation of 3D electrode mesostructures based on the experimental parameters has been shown to be a valuable method.

To stochastically generate an electrode mesostructure, several parameters are needed: electrode composition (active material/carbon/binder volume ratio), particle radius distribution, and porosity and thickness of the electrode. In essence, the active material (typically as spheres) is generated randomly in the simulation box until the desired values are reached. Several observables, such as the amount of overlap between the spheres or the surface area, can be tuned to achieve the desired configuration. Then, the inactive phase can be added by controlling its morphology, *i.e.* as a film around the active phase or as clusters[101,102]. This approach allows access to larger electrode volumes than those experimentally achievable with NanoCT. Some commercial and academic algorithms have been reported for electrode generation[103] and for porous media analysis to extract tortuosity factors[104,105]. An alternative to the extraction of the morphological parameters is the direct use of the generated 3D electrode mesostructures in electrochemical performance models. For that purpose, the inactive phase (carbon/binder) can either be merged with the active material as the solid phase (**Figure 3.3** - Generation II models)[106–110] or be explicitly considered in the 3D model (**Figure 3.3** - Generation III models)[61,101,111,112].

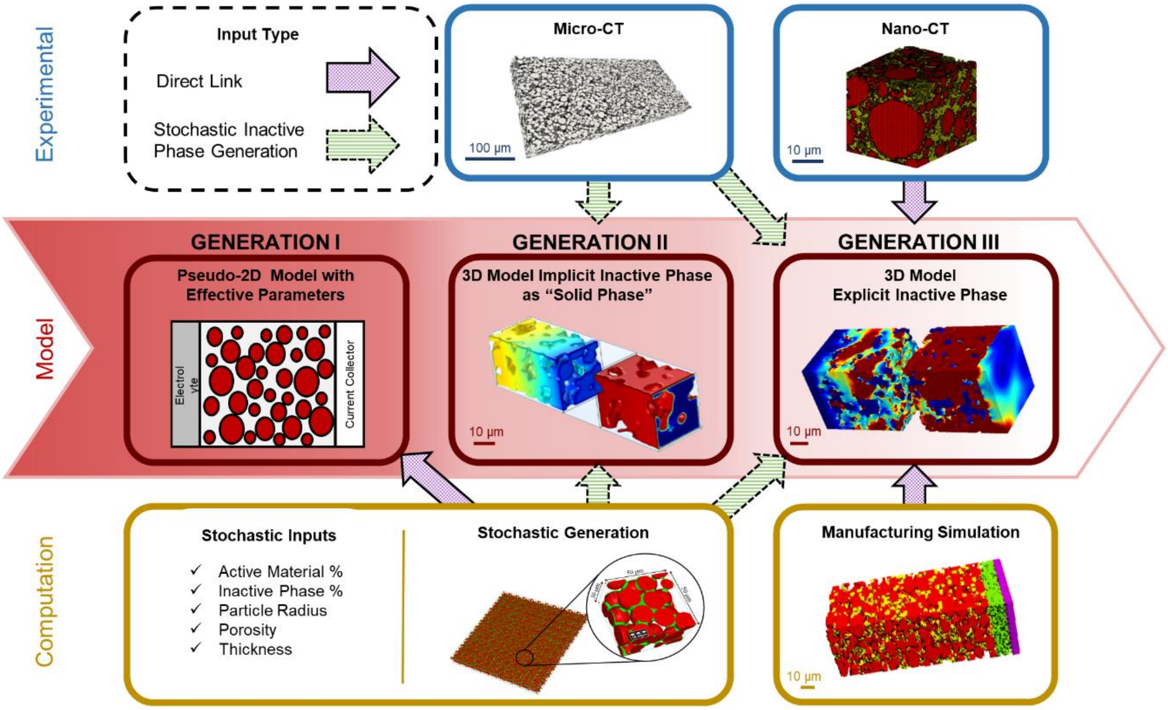

Figure 3.3 | Relation between experimental tomography data, cell model, and computation of electrochemical data in battery systems. To enable 3D models of the battery, tomography data at the micro- and nanoscale can be used either directly (purple arrows) or after stochastic inactive phase generation (green arrows). This allows to compute of the electrochemical performance of the electrode to study the effect of its morphology.

However, even full stochastic electrode mesostructure generation may not be sufficient to replace real battery electrode texture. In that sense, tomography images have been used in the recent years to increase the reliability of 3D battery cell computational models. Electrode mesostructures, reconstructed from MicroCT images, have been used for this purpose by adding the inactive phase stochastically [112,113]. Extracting the carbon and binder additives domains from MicroCT data is indeed challenging due to a too coarse spatial resolution of over ~500 nm. The dataset therefore needs further work to add the binder and carbon to the active material region. The use of MicroCT images allows the models to account for realistic active material shapes and their impact on electrochemical performance[39,114]. For instance, MicroCT has been used in redox-flow battery modeling to capture a representative volume, which is usually much larger than for lithium-ion batteries[115–117]. In this context, it has been used to predict the electrolyte impregnation and the electrochemical response of a redox flow battery using three different electrode mesostructures originating from MicroCT data[118]. However, this technique still has limitations, namely its inability to resolve the spatial location of the inactive phase in the case of lithium-ion batteries. This ability is required to investigate the impact of the arrangement of the active and inactive phases on the electrochemical, transport, and thermomechanical processes within the electrodes. For instance, the ionic transport through the electrolyte is especially impacted by the interconnectivity of pores, which requires the segmentation of the active and inactive phases to extract[119].

In NanoCT, the inactive phase can be distinguished from the active material and the porosity. The extracted structure can be directly used in the Generation III models, without any additional steps. However, the high resolution comes at the cost of a narrower FOV, resulting in a small volume of an imaged electrode. As a result, issues related to the representativeness of the volume have arisen and been addressed in the literature[120,121]. Additionally, such a multi-phase structure can be challenging to import in a finite element/volume method model, especially for numerous interfaces between a large number of phases.

Several tools in recent years have been reported to overcome this challenge[103,122,123]. In 2019, the first Generation III battery cell electrochemical model, with a positive electrode extracted from NanoCT data, was reported with an effective porosity and tortuosity for the inactive phase[124]. Furthermore, in state-of-the-art modeling, efforts have been made to limit as much as possible the use of average geometrical parameters. In 2020, several Generation III model studies have been reported, with resolved structures of the inactive phase and the ability to have no geometrical parameter as a model input[61,125]. This explicit representation of the structure is the key element to capture heterogeneities in the cell. For instance, for the 3D modeling of all solid-state batteries, locating the actual positions of voids in the electrode will be of the utmost importance to understand the device limitations.

Lastly, a new strategy is to achieve representative Generation III models without the need of tomography data: the simulation of the electrode manufacturing process[109,126,127]. By this method, the structure, from the slurry to the final calendered electrode, can be predicted with the inactive phase considered explicitly throughout the process. With the help of experimental inputs (slurry viscosity, porosity of the calendered electrode, etc...) these models are validated at each step. Despite using some geometrical approximations such as spherical particles, this approach yields satisfactory results and links experimental data with modeling, thus paving the way toward predictive digital twins of an entire manufacturing processes and showcasing its impact on battery performances.

3.8.2 Progress and Challenges in *In-Situ* and *Operando* X-ray CT

From the onset of X-ray microtomography, it was recognized that sample preparation and design of *in-situ* environments would be an important challenge for decades to come[128]. Researchers frequently aim to achieve maximum resolution and contrast for samples that are as large as possible to achieve good statistics and representative volume measurements. However, maximizing the contrast and signal-to-noise ratio for a given X-ray energy and specific composition requires limiting the sample to a specific width[129]. This is due to the attenuation of X-rays through the sample thickness, and how there is an optimal extent to which the sample of interest interacts with the incoming beam. There are many different materials used within current and next generation Li-ion batteries, but for simplicity the example of the electrode material $LiNi_{0.8}Co_{0.1}Mn_{0.1}O_2$ (NMC811) will be discussed, while attenuation coefficients for other materials can be determined from open-source databases[130]. For an X-ray energy within the range of 3 to 8 keV (typical range of lab-based NanoCT systems), the optimal thickness of a NMC811 sample is between 10 and 100 µm[129]. Synchrotron sources can tune the X-ray energies to be monochromatic within a wide range from single digit keV to energies approaching 100 keV, thus researchers can weigh the suitability of synchrotrons and beamlines for their specific application. Since most monochromatic or quasi-monochromatic sources operate in the range of 5-30 keV, the optimal width of an NMC811 electrode is between 10 µm and 1000 µm, raising the challenge of designing a small enough Li-ion cell that can achieve relevant *in-situ* or *operando* conditions. For many quantitative measurements of electrode microstructural properties, achieving a representative volume element is critical[131]. Thereafter, building an environment that facilitates *operando* or *in-situ* imaging is needed. Of most interest is electrochemical operation, but some work has focused on mechanical experiments such as *in-situ* compression of electrodes to replicate calendering[132]. Ideally, all environments would be cylindrical, achieving symmetry around the axis of rotation during imaging, which would involve circular discs of electrodes with diameters between 10-1000 µm. Specialized laser-milling has recently been shown to achieve diameters down to 80 µm with little effect on the electrode microstructure[132]. With these conditions in mind, *operando* cell environments have evolved over the past decade[133] but still suffer from design challenges that can jeopardize their performance, reliability, and operational relevance. Common issues include: damaging beam exposure[134], poor control of pressure applied on the cell, stagnant gas that causes poor ionic or electronic contact, and exposure of cell materials to contaminants including air[135]. The high impedance that is often associated with bespoke operando cell designs can limit their ability to achieve high-rate conditions necessitating modifications of well-proven cell designs like coin cells[136]. Current state-of-the-art *operando* cell designs for high-resolution imaging are based on plastic union-fittings with steel rod current collectors that seat electrodes around 1 mm in diameter[52,137,138], but much opportunity remains to improve reliability, rate performance, and ease of assembly. When a functional operational design that is suitable for the X-ray imaging conditions is achieved, further challenges await for minimizing artifacts in reconstructions, systematic errors, and data processing for quantitative analyses, such as those outlined in Box 1.

3.9 Future of Battery X-Ray CT

Box 2 Artificial Intelligence and Machine Learning in CT

Creating a quantitative link between the architecture of porous electrodes in electrochemical devices and their performance is extremely challenging. For instance, battery electrodes have 3D features across multiple length scales from mm to nm requiring multi-modal techniques to fully characterize them. Furthermore, from the beginning of an electrode's time inside a cell, its architecture changes, which poses additional challenges to quantify the evolution of the electrode microstructures throughout its life. As a non-destructive tool that bridges multiple length scale, X-ray CT has emerged as a powerful technique to discern dynamic features that influence the performance of electrodes. However, access to high-resolution data is limited and the ability to measure the wide range of electrode architectures throughout their life infeasible. Machine learning (ML) techniques (within the wider field of Artificial Intelligence) present a plethora of opportunities to elucidate structure-function relationships for porous electrodes images produced by CT and/or multi-physics/multi-scale modeling. In short, ML techniques give to a computer the power to learn and self-correct from data, building "models" (also called *ML models*) in an automatic way. These models can then be used to predict qualitative or quantitative outcomes, allowing for instance to unravel complex parameters interdependencies in multi-dimensional datasets and to automatize processes that would too time-consuming to perform manually. Regarding the latter, segmenting and distinctly labelling complex features in CT-images such as cracks[8] or regions of delamination[9] can be conducted more quickly and accurately with ML techniques. Characterizing features from multiple length scale imaging and applying ML generative methods to artificially create representative electrode microstructures[7] also holds promise for generating 3D-resolved images with greater detail than any single imaging mode could achieve. Critical to the acceleration of this initiative is to make robust multiscale data open-source, which would not only alleviate the limitation of accessing specialized imaging facilities, but also provide a wealth of microstructural information available for ML and multi-physics/multi-scale models. The adoption of ML techniques in these areas are expected to help accelerate diagnostics of microstructural phenomena, as well as identification of favorable particle and electrode architectures for long life and specific operating conditions.

3.9.1 Correlative Workflow Characterization

While X-ray CT is a powerful non-destructive imaging tool, it still suffers from several limitations such as the inability to distinguish chemical species with similar X-ray absorption, or to provide nano-scale information about the sample's morphology. As such, one of the main strategies to overcome these shortcomings is to combine X-ray CT with other tools, i.e., correlative tomography. Several studies have already shown that both low and high-resolution X-ray CT scans can be used to determine a region of interest which is then milled using FIB/SEM. Then, volume reconstruction can be performed, and the data can be aligned to the high-resolution CT scan. Moreover, FIB/SEM benefits from the multiple detectors, such as EDS, EBSD, WDS, Raman, and ToF-SIMS, providing valuable insights correlating chemical and morphological information. As already shown in the literature, a lamella of the region of interest can then be used for STEM analysis, providing nano-scale resolution imaging, combined with crystallographic and spectroscopic information thanks to EELS and electron diffraction. This method was successfully applied in 2014 by Burnett *et al.* to study the corrosion of stainless steel, as EBSD and EDX combined allows to determine both element segregation and grain orientation[139]. Similarly, Slater *et al.* were able to combine MicroCT with NanoCT and STEM/EDS by using Plasma FIB milling, gaining insights on the influence of grain boundaries orientation in cavity formation in Type 316 stainless steel[140].

More recently, Zubiri *et al.* demonstrated that coupling lab-scale Nano CT with electron tomography was an efficient way to combine the higher resolution of electron tomography (ET) with the wider FOV of NanoCT[141]. As such, the ML-assisted segmentation of the pores in zeolite particles from the CT data was improved significantly by using the segmentation of the higher resolution ET data as a training dataset.

In the battery field, a few studies were successful at applying correlated tomography to electrode composites or separators[7,49,142,143]. The combination of high contrast absorption X-ray tomography with ptychographic X-ray CT was shown to be able to provide detailed microstructure of Si composite anodes, distinguishing the Si particles from graphite and the carbon-binder domain, and was even able to resolve the SEI layer[49]. The obtained dataset was then used to model the state of charge distribution of individual Si particles. On the cathode side, FIB cross-sections were used to help segment the NanoCT data of a $LiNi_{0.33}Mn_{0.33}Co_{0.33}O_2$ electrode, allowing the porosity network and carbon-binder domain to be resolved[142]. This information was then successfully combined with a lower resolution MicroCT scan to evaluate the tortuosity factor of the electrode. SEM cross-section views were also combined with X-ray CT data of Li-ion battery separators to stochastically generate fibrils in the porous network. These fibrils, too small to be directly observed by MicroCT, were shown to have a significant influence on the prediction of the effective diffusion coefficient[143].

Correlative tomography, by employing a low-to-high resolution approach, is a flourishing technique that can provide the multi-scale information needed for the future of battery materials research. Combined with tools such as stochastic generation and electrochemical modeling, deep insights onto the underlying limitations of different battery systems can be gained. Nevertheless, some technical considerations still need to be solved before this method can be widely applied to all types of systems. Principally, when working with sensitive materials, all steps of the analysis must be carried out under a protective atmosphere, necessitating careful design of the samples and transfer devices. Moreover, while the possibility to investigate a region of interest with nm-scale resolution makes this a method powerful, reducing the size of the sample sufficiently for high resolution tools (i.e., NanoCT or even TEM) can still be challenging, and tools with higher milling throughput than FIB, such as Plasma FIB (PFIB), laser PFIB, or broad ion beam milling, are often required.

3.9.2 Perspective of CT Data Analysis with AI/ML

It is evident that the future of CT data analysis is strongly correlated with the transformative tools of the emerging Digital Era, including AI/ML and multiscale modeling. AI/ML allows high throughput segmentation of composites containing multiple types of materials, such as lithium-ion battery electrodes which encompass metal oxides, carbon particles, and polymers. Such impressive segmentation capabilities allow electrochemically active, inactive materials, and pores to be distinguished faster than ever before, triggering the emergence of powerful digital twins of real electrode electrochemical operation. Still the challenge remains for CT to distinguish polymeric binders from carbon additives, both materials affecting differently the overall electrode performance.

To enhance the development of robust AI/ML-powered segmentation methodologies, open-source repositories that provide free access to already characterized electrode structures should be deployed. Such repositories should contain not only the actual data but also the metadata allowing to precisely track the conditions on which the characterization was performed, and some initiatives have already emerged[144]. Datasets extracted from these repositories can be used to train a new generation of AI/ML models and generate *in silico* extended volumes. This would be particularly suitable for developing representative electrochemistry simulations from pre-existing tomography data of composite or electrode structures, which some have shown using Generative Adversarial Networks (GANs)[7]. Strategies such as this can be used to predict complex structures for compositions not yet characterized and may open tremendous opportunities to accelerate the prediction of how manufacturing conditions impact composite structures[102].

We also expect the emergence of AI/ML-orchestrated workflows integrating CT characterization, data analysis, and physical model generation at multiple scales (multiscale modeling) (**Figure 3.4**). By coupling existing middleware technologies (*e.g.* UNICORE[145]) to AI/ML scripts, such workflows may not be difficult to develop. Thus, ML can be used to sequentially or iteratively couple different length scale models automatically with varying degrees of fidelity. Moreover, ML can also assist in comparing the modeling outcomes with experimental data. The outputs can then later be used to train AI/ML models to predict synthesis and manufacturing conditions in order to achieve optimal material properties. Such an automated multi-fidelity approach may revolutionize the conception of new composites materials by linking experimental data (CT) with computational simulations.

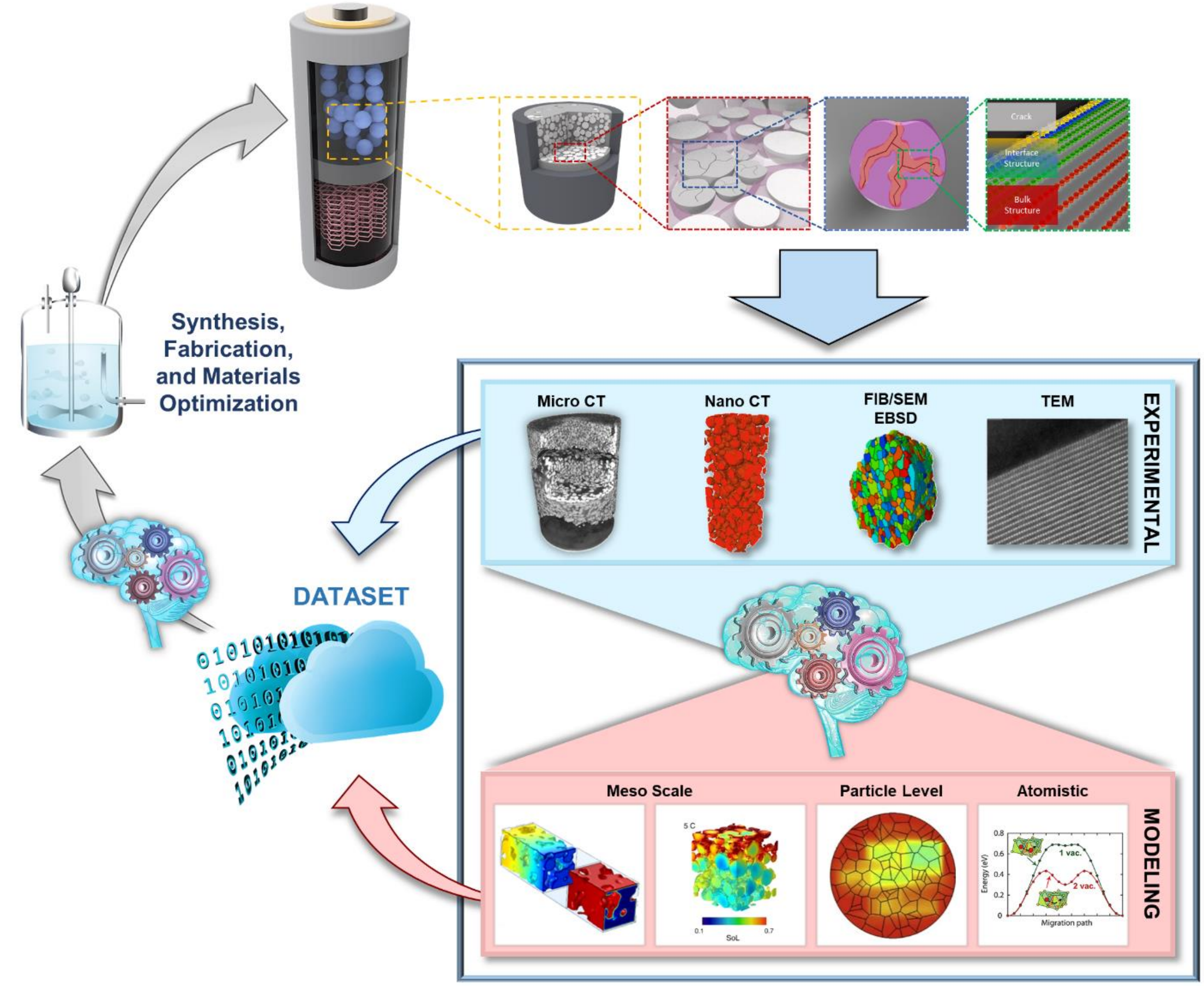

Figure 4 | Correlative workflow analysis and modeling: combining CT and advanced characterization techniques in the development of comprehensive predicative models. Illustrates the connection of experimental characterization data with modeling using AI/ML and the cyclical workflow to improve the synthesis, fabrication, and battery performances using predictive models.

3.10 Conclusion

Since its conception in the 1970s, CT has profoundly impacted the scientific community. In the last two decades, it has extended to greatly influence battery research and development. As a non-destructive tool, CT can perform powerful *in-situ* and *operando* studies in a multitude of battery chemistries. The reconstructed volume and extracted morphological parameters (*e.g.*

particle distribution, porosity, and tortuosity) can be incorporated in predictive models to simulate battery performances. The CT images can also be used to generate large representative volumes using AI/ML techniques, such as Generative Adversarial Networks, which can generate realistic multiphase porous electrode microstructures[7]. The advent of such techniques can drastically reduce the number of required CT characterizations for 3D-resolved electrochemical models, while ensuring representative volumes for simulations.

Lastly, the combination of multiscale 3D morphological characterization techniques (*e.g.* FIB-SEM, TEM, MicroCT, and NanoCT) may pave the way for performance predictive models that can incorporate phenomena at multiple length scales. Characterization data and models can then be consolidated in open-source datasets and repositories, and even incorporated in Virtual Reality (VR) environments and tools to educate a new generation of researchers on electrode structures and geometric parameters[146]. With the tremendous progresses achieved in these last 20 years in CT experimentation, analysis, computational modeling, and AI/ML, there is promise of remarkable achievements and discoveries in the years to come.

3.11 Acknowledgements

The authors gratefully acknowledge funding support from the US Department of Energy, Office of Basic Energy Sciences, under award number DE-SC0002357 (program manager Dr. Jane Zhu). A.A.F. and M.C. acknowledge the European Union's Horizon 2020 research and innovation program for the funding support through the European Research Council (grant agreement 772873, "ARTISTIC" project). A.A.F. acknowledges the Institut Universitaire de France for the support. This work was authored in part by the National Renewable Energy Laboratory, operated by Alliance for Sustainable Energy, LLC, for the U.S. Department of Energy (DOE) under Contract

No. DEAC36-08GO28308. Funding was provided by the U.S. DOE Office of Vehicle Technology Extreme Fast Charge Program, program manager Samuel Gillard. The views expressed in the article do not necessarily represent the views of the DOE or the U.S. Government. The authors would also like to acknowledge the support of Mira Scharf in design and figure art. For the collection of the Zinc battery CT data, the authors would like to acknowledge the National Center for Microscopy and Imaging Research (NCMIR) technologies and instrumentation are supported by grant R24GM137200 from the National Institute of General Medical Sciences. AgO and Zn used in this work were provided by ZPower LLC, and $LiNi_{0.5}Mn_{1.5}O_4$ (LNMO) used in this work was supplied by Haldor Topsoe. The authors would also like to acknowledge the support of LNMO electrode fabrication by Ningbo Institute of Materials Technology and Engineering (NIMTE) in China. This work was performed in part at the San Diego Nanotechnology Infrastructure (SDNI) of UCSD, NANO3, a member of the National Nanotechnology Coordinated Infrastructure, which is supported by the National Science Foundation (Grant ECCS-1542148).

3.12 Supplementary Information

3.12.1 Supplementary Section 1

3.12.1.1 Common Non-CT Battery 3D Morphological Characterization Tools

Characterization techniques used in the battery field provide valuable insights into a wide range of material parameters, such as elemental composition, chemical bonding, and morphology. In this section, we isolate the focus toward techniques that provide 3D morphological information, and touch upon the elemental or chemical information that the method may additionally offer. For instance, scanning Electron Microscopy (SEM) is one of the most widely used morphological techniques in the battery field, and typically couples Energy-Dispersive X-Ray Spectroscopy (EDX) to provide elemental composition information (either point, line, or 2D mapping). With its high resolution (~ 1 nm), wide field of view (FOV), and relatively easy sample preparation, nearly all battery studies incorporate SEM in their work. Similar to XRCT, SEM can also generate 3D reconstructions when coupled with focused-ion beam (FIB) milling to collect a stack of 2D slice-by-slice images of the milled thickness[147,148]. However, due to the lengthy process of milling successive slices, typically only a few tens of microns in each direction can be reconstructed, limiting the use of the technique to small regions of interest (ROI). Plasma FIB (PFIB) can overcome this limitation by using fast milling enabled by a much higher ion beam current and the use of different ions (Xe^+, Ar^+, O^+, Ga^+…), allowing for volumes up to more than a hundred micrometers in each direction[149,150].

Transmission Electron Microscopy (TEM) offers a drastic increase in resolution, with reported resolution values as high as 0.5Å[151]. However, sample preparation is more challenging since samples need to be thinned to a lamella to allow for electron transmission. Recent attention in the battery field has been directed to low temperature, cryogenic TEM (cryo-TEM) with cryo-FIB milling[152], since the milling and electron beam can often distort low Z materials (such as Li) due to thermal heating. This has been especially notable for 3D imaging Li-metal anodes, with reports in the literature of 3D microstructure of electrodeposited Li and quantification of the total packing density, surface area, and volume[153]. Electron Energy Loss Spectroscopy can also (EELS) be used in conjunction with TEM to provide chemical and bonding information. Because of its high energy resolution (~1 eV), EELS can distinguish the different chemical environments of an element. Furthermore, EELS also has the added benefit of being sensitive to light elements such as Li, which is usually challenging to characterize with other techniques such as SEM-EDS. With these advantages, EELS together with TEM have been used to study the Li metal electrode interfaces with solid state electrolyte, reporting both structural and chemical information[154]. Also, since electrons radiated out can destructively and constructively interfere with each other to form a diffraction pattern, Selected Area Electron Diffraction (SAED) can be employed to uncover the structural properties of a sample. Because SAED can provide a diffraction pattern from a certain area of the sample, it can be used to study the nano-crystal structures and examine crystal defects in samples like cathode particles[155].

Secondary Ion Mass Spectrometry (SIMS) is another widely used technique in the battery field to study composition as a function of thickness. SIMS uses a focused primary ion beam to perturb a sample, and distinguish based on mass, the secondary atomic and molecular ions emitted from the sample. Dynamic SIMS uses a high ion current to mill through the sample and obtain a depth 1D profile. Time of Flight SIMS (ToF-SIMS) uses a much lower dose of (~10^{12} to 10^{13} ions/cm^2) so only the top-most monolayer is perturbed, and surface contamination is negligeable[156]. In ToF-SIMS, the secondary ions are analyzed based on the mass dependent flight time and can be used to resolve 2D maps. When combined with milling, TOF-SIMS can produce 3D tomograms with depth resolutions of less than a nm and lateral resolutions down to 50nm[156]. ToF-SIMS can also be used for any element on the periodic table along with molecular species with trace detection in the ppm range. It has been used in numerous electrochemical studies, such as uncovering sodium ion contamination as the main culprit of potential induced degradation in silicon solar modules[157,158]. In the battery field, it has been especially useful for interfacial studies in sodium and Li-Ion batteries (LIB)[159,160], such as the work by Gauthier *et al.*, in which they were able to visualize the 3D structure and composition changes with cycling of LTO and LMO cathodes[161]. Still, ToF-SIMS is semi-quantitative at best, typically requiring a standard to obtain quantitative information, and can suffer from erroneous signals due to ion contamination and sample charging effects[162,163].

3.12.2 Supplementary Section 2

3.12.2.1 Tortuosity

Tortuosity was first introduced by Epstein in 1989[164]. Illustrated by (Eq. 1), geometric tortuosity (τ) is defined as the shortest pathway through a porous structure $\boldsymbol{\Delta l}$ divided by the Euclidean distance between the starting and end point of the pathway $\boldsymbol{\Delta x}$[165]:

$$\boldsymbol{\tau = \frac{\Delta l}{\Delta x}} \tag{1}$$

However, in battery operation, the ion transport through porous electrodes is driven by gradients of chemical and electrostatic potentials and pursues the path of least "transport resistance" rather than the geometric Euclidean distance. For this reason, tortuosity for electrochemical systems can be better described with gradients of potentials (namely, fluxes) rather than purely geometric arguments. To incorporate fluxes, a similar term is introduced, the tortuosity factor ($\boldsymbol{\kappa}$),

$$\boldsymbol{\kappa = \tau^2} \tag{2}$$

which is the square of the tortuosity, and is used to account for both the path length and the change in flux of moving species through a porous medium[164,165]. This term can then be used in (Eq. 3) to model the effective diffusion coefficient ($\boldsymbol{D_{\mathrm{eff}}}$) of ions through a porous media,

$$\boldsymbol{D_{\mathrm{eff}} = \frac{\epsilon}{\kappa} D_{\mathrm{bulk}} = \frac{\epsilon}{\tau^2} D_{\mathrm{bulk}}} \tag{3}$$

with porosity $\boldsymbol{\epsilon}$, and a bulk diffusion coefficient $\boldsymbol{D}_{\mathbf{bulk}}$. However, depending on the system analyzed, equation 3 may not sufficiently account for added effects, such as pore clogging and entropic restrictions of ionic transport[164,165].

In many cases the tortuosity factor is unknown, and the Bruggeman correlation approximation (Eq. 4) is used giving (Eq. 5):

$$\boldsymbol{k} = \frac{\mathbf{1}}{\boldsymbol{\epsilon}^{\mathbf{0.5}}} \tag{4}$$

$$\boldsymbol{D_{eff}} = \boldsymbol{D_{bulk}} \times \boldsymbol{\epsilon}^{\mathbf{1.5}} \tag{5}$$

Even though the applicability of the Bruggeman correlation has been validated for porous electrodes[166], it remains an approximation.

To illustrate the importance of this factor, Lu *et al*. focused on porous Cu current collectors for Li-metal batteries and was able to highlight the impact of pore size and tortuosity on the effectiveness of lithiation and capacity retention[89]. For narrow pores, the tortuosity factor was diverging at a lower capacity than for large pores, indicating that the Li deposited was clogging the pores, hindering a homogeneous use of the current collector. However, large pores structures would suffer from a lower surface area, which led to the conclusion that a medium pore size was optimal for the rate studied.

These techniques based on Fickian diffusion are the most used since they have higher representability of various structures. The Fickian diffusion method is available in several tools commercial and free to use, and among them the most used are: Avizo, Geodict, and TauFactor [104,105,167]. It is noteworthy that even if this method is the most used, its validity is still under debate.

In the diffusion-based approach, the ions migrate from one end of the system to the other, while in an electrode the ions migrate to the surface of the active material. In this sense, a new methodology to improve the accuracy of the tortuosity factor has been recently suggested[104,105,167,168].

3.12.2.2 Pore Network Models (PNM)

Once segmented, an interconnected pore network model (PNM), composed of pores (spheres) and throats connecting them (cylinders) can be extracted, and potentially utilized to the study the mesostructure evolution during fabrication processes like calendering[126]. Torayev *et al.* introduced a 3D-resolved PNM extracted from a CT image of a Li-O_2 battery carbon electrode[119]. The extracted pore network consists of a family of spheres with different sizes connected by cylindrical throats, and the model describes species transport and electrochemical formation of Li_2O_2 precipitates. Thanks to this model, the authors show that pristine electrode samples that have the same average porosity and tortuosity factor, but different pore interconnections, show varying discharge performances. In this case, the Li-O_2 battery cells varied in discharge performances due to the transport and Li_2O_2 precipitation anisotropy in the pore network. This explains the frequent experimental observation where systems offer different capacities while using cathodes with the same materials, electrolyte, average properties, and are discharged at identical conditions. With the same model, they were able to show in a later study how the cathode tortuosity factor evolution depends on the pristine cathode[169]. This matched well with experimental results from Ding *et al.* [170], suggesting that as electrodes are discharged, smaller pores clog, ionic transport paths become more tortuous, and discharge capacities are limited as ions are unable to reach parts of the electrode.

3.12.2.3 Influence on Scan Time

The scan time versus the voxel size is shown in **Figure S3.1** and reveals that smaller voxel sizes tend to require longer experimental scan times. This makes high resolution *in-situ* or *operando* experiments exceedingly difficult, since the scan times can be on the order or larger than the scan times of the desired observable phenomena. The longer scan times are necessitated by the higher exposure times needed to resolve small features. SRTXM uses high brilliance X-rays, which increases the transmitted signal count and decreases the scan time needed, thus making it easier to perform *in-situ* or *operando* studies.

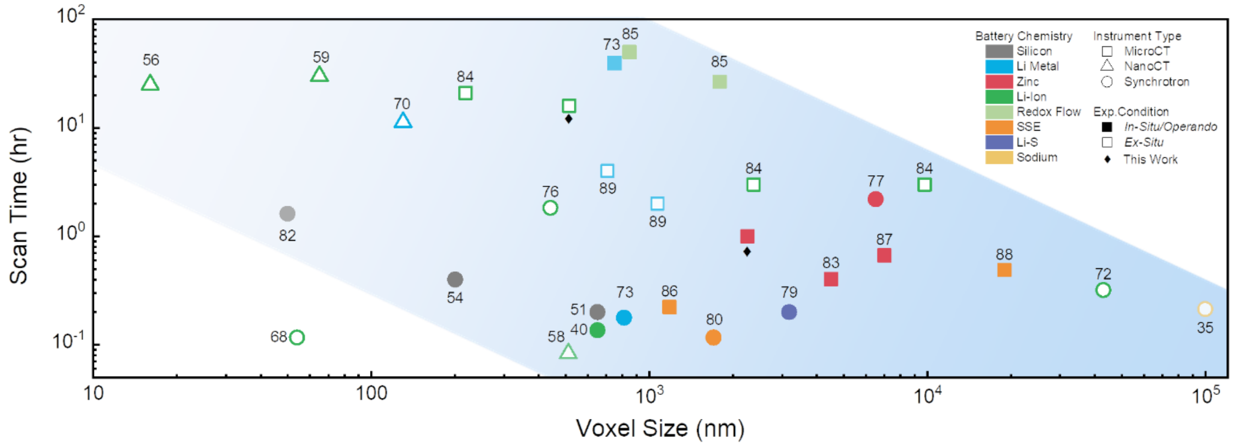

Figure S3.1 | Trends of scan time vs. literature reported voxel size. Reference labels here refer to references in the main text.

3.12.2.4 *In-Situ* CT of Zinc Battery

As a non-destructive instrument, CT is ideal for *in-situ* and *operando* experiments. This is especially true for Zn-based batteries, where the particles are often larger and more X-ray attenuating than in LIBs and it is easier to distinguish phases[75,77,87]. For instance, Franke-Lang *et al.* characterized the Zn particle distribution *in-situ* in a charged and discharged Zn-air battery and showcased the issue of anode shape change and Zn connectivity loss as a function of discharging[87]. Likewise, in **Figure S3.2**, we show data for an *in-situ* characterization study of a Zn-AgO battery. **Figure S3.2a** shows a reference scan of Zn and ZnO powder, where the gray value histogram reveals distinct regions for Zn and ZnO. Using global thresholding of the histogram, the evolution of Zn and ZnO can be monitored in an *In-Situ* cell shown in **Figure 3.2b** for differing greyscale regions.

Figure 3.2c-d shows the evolution of the colorized Zn and ZnO regions in the anode electrode as a function of State-Of-Charge (SOC), where “C1” and “D1” refer to the first charge and discharge respectively. Initially, the anode is comprised of mostly Zn, but as the cell undergoes cycling, ZnO overwhelms the anode until little to no Zn is left in the 5th discharge. As a result, the Zn particles start to shrink, as shown in the distribution of the Zn particle equivalent diameter in **Figure 3.2e**.

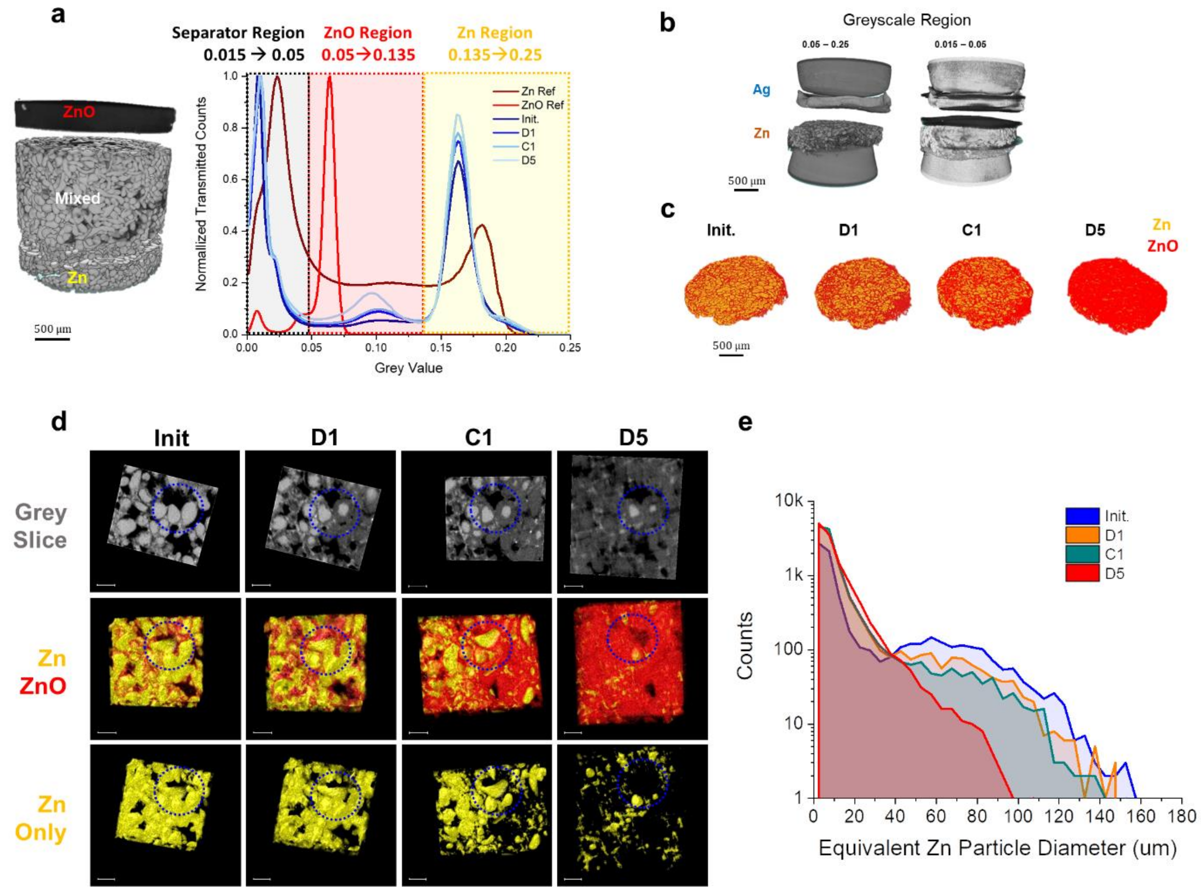

Figure S3.2 | In-Situ CT of Zn-Ag Battery. a) This work, showing grey value histograms of Zn and ZnO reference CT cell and of Zn region in Zn-AgO CT cell at different SOC and cycle number. b) Zn-AgO volume rendering with thresholding at different regions of histogram. c) Colorized 3D volume rendering of segmented Zn anode at different SOC: "Init" is initial uncycled, "D1" and "C1" is after first discharge and charge, and "D5" is after 5th cycle discharge. d) Isolated particle-scale region within Zn anode of cycled Zn-AgO CT cell with grey 2D slice shown at top and colorized volume renderings shown in middle and bottom (yellow is Zn and red is ZnO). Scale bars are 100µm in length. e) Zn particle size distribution histogram, where the Zn particles were segmented and assumed to be spheres.

3.12.2.5 Segmentation of LIB Cathode

In CT of battery electrodes, it is crucial to resolve the 3 main phases typically incorporated: the active material, binder, and pores. **Figure S3.3a** shows layered LNMO LIB battery cathodes alongside the 2D X-ray projection and 2D virtual slice taken using high resolution HeliScan MicroCT to image a large FOV of the entire sample. Through filtering with the Non-Localized Means (NLM) and Unsharp Mask (UM) filters (**Figure S3.3b**), the three phases can be distinguished, and clear distinct regions can be observed in the grey value histogram in **Figure S3.3c**. After filtering, segmentation was performed with the global threshold values (96 and 150) as starting inputs for the watershed-based segmentation. The electrode, colorized with the different phases, is shown in **Figure S3.3d**, where the volume fraction of pores was found to be 51.0%. The results for the volume fraction measurement are depicted in **Table S3.1** and compared to calculated values determined from electrode volume, weight, and density measurements, where the thickness was determined from cross-section images taken from 2D SEM (shown in **Figure S3.4**). While the calculated values are averaged and based on 2D SEM thickness approximations, the results from CT account for the 3D interconnected porosity and are likely more accurate.

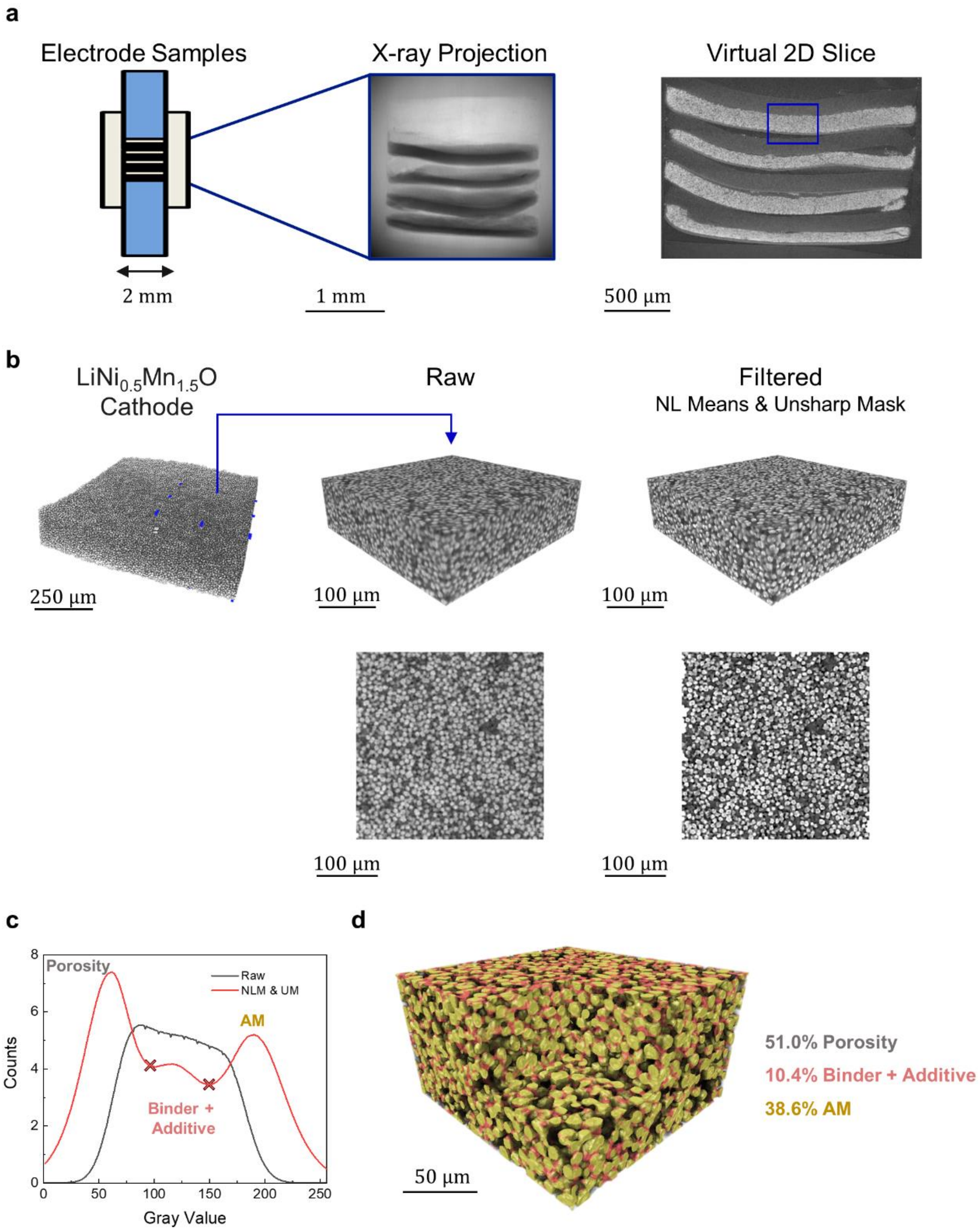

Figure S3.3 | Segmentation of 3 Phases of Li-Ion Battery Cathode using 3D MicroCT. a) CT sample architecture with layered electrodes separated by PTFE films, X-ray projection, and a virtual 2D slice showing full range of the field-of-view. b) Cropped LiNi$_{0.5}$Mn$_{1.5}$O$_4$ cathode dataset before and after Non-Local Means (NLM) and Unsharp Mask filtering (UM). Corresponding XY slices below. c) Grey value histogram of raw data and after applying NLM and UM filters. “X” markers represent threshold regions indicated in watershed-based segmentation. d) Segmented and colorized filtered tomogram with volume fraction percentage of the 3 phases.

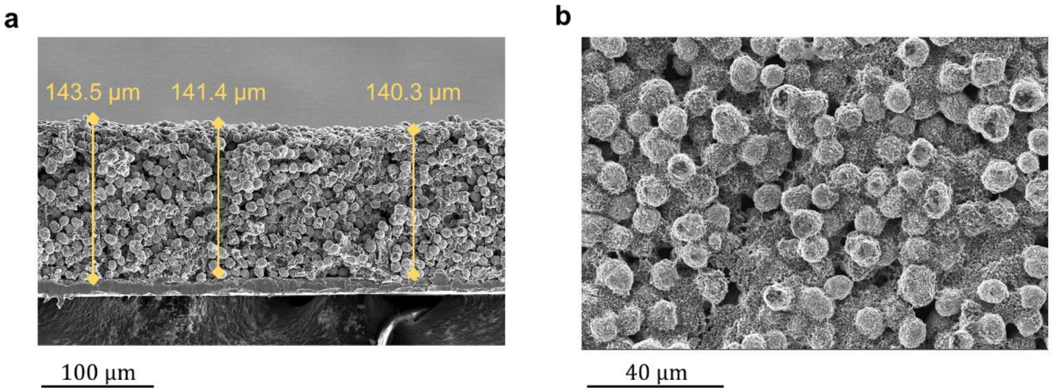

Figure S3.4 | SEM of Li-Ion LNMO Battery Cathode. a) FIB-SEM of LNMO cathode cross-section showing thickness determination from 2D sliced images. b) SEM of LNMO cathode topside

Table S3.1 | Comparison of Volume Percentage Determined by Physical Measurements and 3D MicroCT.

Method	Porosity (%)	Binder + Additives (%)	Active Material (%)
Physical Measurements w/ 2D SEM	46.8 ± 0.9	11.1 ± 0.2	42.1 ± 0.7
3D Segmentation w/ µCT	51.0	10.4	38.6

3.12.2.6 CT Experimental Details

The *in-situ* cells in the Zn study (**Figure S3.2**) were constructed within a Teflon tube with a 2 mm inner diameter. Electrical contact to the Zn and AgO electrodes was made via conductive carbon current collectors and 2 mm diameter Au coated stainless-steel rods. The current collector, electrode, electrolyte, separator composition, and battery architecture all follow from our recently published work by Yin and Scharf *et al.*[50]. The scan was performed by a *ZEISS Xradia 510 Versa* MicroCT instrument, and parameters were kept consistent between each scan at the various SOCs. An X-Ray energy of 140 kV was used with a voxel size of 2.25 µm, a FOV of 2.23 mm x 2.56

mm, a 2.5 hr scan time, a 4X magnification, an exposure time of 2 s, a binning of 2, and 1800 projections. The source to detector-to-detector distance was also kept the same at 13.83 mm to ensure similar grey values between scans.

The cathode material used in the LIB CT study (**Figure S3.3**) was layered in a 2 mm diameter Teflon tube with 2 mm diameter Teflon rods at each end. The active material $LiNi_{0.5}Mn_{1.5}O_4$ (LNMO) (Haldor Topsoe), HSV-900 PVDF (Arkema), and Super C65 (MTI) were mixed in a mass ratio of 90:5:5 in the N-Methyl-2-Pyrrolidone (NMP) solution to give a uniform slurry. Doctor blading was utilized to cast the slurry on the aluminum foil with appropriate gap thickness. The casted slurry was then transferred into a vacuum oven and underwent a 100 ℃ heating to remove the NMP. The scan was performed using a *ThermoFisher Scientific HeliScan Mark II* MicroCT instrument. A mutliscale approach was utilized to collect a scan of the sample to include all layers, as well as a subsequent higher resolution acquisition[66,171]. A helical space filling protocol was used with an X-Ray energy of 100 kV with a voxel size of 0.836 µm, a FOV of 2.3 x 2.3 x 3.05 mm, an exposure of 3 seconds, 6 frames averaging per projection, 2200 projections, and detector binning of 1 resulting in a 12 hr scan time (**Figure S3.3a**). The higher resolution scan with 0.5142 µm voxels used a helical space filling protocol with an X-Ray energy of 60 kV, an exposure of 4 seconds, 7 frame averaging per projection, 1800 projections and detector binning of 1 resulting in a 1.425 mm x 1.425 mm x 1.54 mm FOV and 16 hr scan time (**Figure S3.3b**).

The analysis for both studies were performed with Amira commercial software. The “Non-Local Means” and “Unsharp Masking” modules were applied for data filtering, and the “Watershed Segmentation” and “Separate Object” modules were applied for segmentation.

3.12.3 Supplementary Section 3

3.12.3.1 General CT Description

In CT the X-ray beam is attenuated by the sample by the Beer-Lambert law in equation (6),

$$A = \frac{I_f}{I_0} = e^{-\mu t} \tag{6}$$

where $\boldsymbol{A}$ is the attenuation, $\boldsymbol{I_0}$ is the incident irradiation intensity, $\boldsymbol{I_f}$ is the after transmission, $\boldsymbol{\mu}$ is the material's linear attenuation coefficient, $\boldsymbol{t}$ is the material thickness[5]. Photons are collected using a flat panel or a CCD detector with a scintillator, and depending on the system, additional magnification optics are added to enhance resolution at a larger FOV[65]. MicroCT systems use polychromatic X-rays in which the energy can regulated by the user, NanoCT systems use semi-polychromatic X-rays at a fixed energy, and SRTXM uses monochromatic synchrotron radiation with extremely high intensity. For NanoCT systems, additional optics are often used such as capillary condensers and Fresnel zone plates that help focus the X-rays on a small area and make the beam quasi-monochromatic around the peak emission from the X-ray source. For low-energy and quasi-monochromatic systems, Zernike phase contrast (ZPC) rings can be included, which enhances signal from refracted regions hence improving the detection of sharp features and edges.

3.12.3.2 Artifacts and Reconstruction

3.12.3.2.1 Undersampling and Aliasing

Undersampling of the number of projections needed to reconstruct a sample can cause artifacts known as view and ray aliasing[93]. View aliasing originates from too large an interval between projections, leading to a misregistration of sharp edges and small objects in a scan and resulting fine stripes to appear radiating from the edges. Ray aliasing originates from undersampling within a projection results in fine stripes close to a structure.

3.12.3.2.2 Ring Artifacts

Ring artifacts observed relate to failures in the flat-field detectors. Defective detector elements and damaged scintillator screens or mis-calibrated detector elements can result in white, black or over-/underestimated pixel values and is often observed in as rings in the reconstructed images[91,93]. There are two experimental methods to alleviate detector errors: flat-field correction and detector shifting. Flat-field correction works by calibrating the detectors prior to scanning and to identify flawed elements. Detector shifting shifts the array of detectors during the scan and calculates an average to reduce ring artifacts. However, if flawed elements have a non-linear response, flat field correction does not work and can even introduce artifacts, and detector shifting will not solve heavy artifacts caused by defects in the scintillator or CCD. In this case, we turn to post-processing to address these issues. Likewise, ring artifacts can be lessened by employing a slice-wise filtering algorithm introduced by Sijbers and Postnov[172], however the results will not completely remove the artifacts[92], and it is best to solve the issue directly by looking at the flat panel detectors.

3.12.3.2.3 Reconstruction Algorithms

After a scan, the data undergoes a reconstruction process that converts the XZ projections to a series of XY slices to recreate the 3D structure. Since the 1970s, numerous reconstruction methods came about from early approaches like the algebraic reconstruction technique (ART) and filtered back projection (FBP) algorithm to the presently used iterative reconstruction (IR) methods and the more recent AI/ML techniques being explored[173]. Some artifacts can be lessened or removed by applying algorithms in the reconstruction process[95]. For example, beam hardening artifacts can be lessened using an iterative approach outlined by Hseih *et al.*, where the projection error due to beam hardening is estimated through forward projecting only the high-density objects and is then subtracted from the original projection and reconstructed to produce a tomogram with a beam-hardening correction[174].

3.12.3.3 Filtering

3.12.3.3.1 Non-Local Means Filter

Non-Local Means (NL-Means) algorithm is another popular edge-preserving filter[92,175]. This method sets voxels to a weighted average, where the weight depends on the similarity of a voxel to its neighboring voxels in a specified window. While one of the most robust filtering methods, NL-Means is computationally expensive, requiring high processing power CPUs for analysis on large data.

3.12.3.3.2 Anisotropic Diffusion Filter

The Anisotropic Diffusion (AD) filter is often employed to better protect edges when filtering[92,95]. Perona and Malik were the first to apply this method, where boundaries can be differently smoothed from internal structures based on intensity gradient across edges, $\left(\boldsymbol{\nabla I'} = \frac{\boldsymbol{\partial I'}}{\boldsymbol{\partial x}} + \frac{\boldsymbol{\partial I'}}{\boldsymbol{\partial y}} + \frac{\boldsymbol{\partial I'}}{\boldsymbol{\partial z}}\right)$. The essential idea stems from the understanding that the denoised image, $\hat{\mathbf{I}}(\mathbf{x}, \mathbf{y})$, can be estimated by the convolution ($*$) of the gaussian kernel, $\mathbf{G}(\mathbf{x}, \mathbf{y}; \boldsymbol{\sigma})$, with the observed image, $\mathbf{I}'(\mathbf{x}, \mathbf{y})$, which is equivalent to the isotropic heat diffusion equation:

$$\hat{I}(x,y) = G(x,y;\sigma) * I'(x,y) \tag{5}$$

$$\frac{\partial u(x,t)}{\partial t} = \nabla \cdot [D(u,x)\nabla u(x,t)] \tag{6}$$

$$\frac{\partial \hat{I}(x,t)}{\partial t} = \nabla \cdot [g(|\nabla I'|)\nabla I'(x,t)], \quad I'(0) = I' \tag{7}$$

where $\boldsymbol{u}$ is the density of the diffusion material at position $\mathbf{x}$ and time $\mathbf{t}$, $\mathbf{D}$ is the diffusion coefficient for density $\mathbf{u}$ at position $\mathbf{x}$, and $\boldsymbol{g}$ is the non-linear diffusion coefficient[95,176]. Regulating $\boldsymbol{g}$ alters how edges are smoothed. If $\boldsymbol{g}$ is low, small intensity gradients block conduction across edges, while if $\boldsymbol{g}$ is large, smoothing occurs more evenly across image. When using this filter, it is important to select the right value of the simulated diffusion as to not blur the image too much and lose edges, but still enough to de-noising internal structures.

3.12.3.3.3 Unsharp Mask

The unsharp mask algorithm functions by subtracting an image with the convolution of the image with a smoothing filter, shown by the following equation:

$$\hat{I}_{UM}(x,y) = I'(x,y) - \frac{w\big(G(x,y;\sigma) * I'(x,y)\big)}{1-w} \tag{8}$$

where $\boldsymbol{\sigma}$ should be approximately half the width of the blurred edges and w is a specified weight that determines the degree of sharpening. This method works to enhance the high spatial frequency regions locally by subtracting the smoothed or unsharpened image from the original image and then adding the difference to the original, thereby using the unsharpened image as a mask. Other variations use different smoothing kernels instead of a gaussian, such as a Laplacian kernel which is the 2nd spatial derivative of the image, where convolving with this kernel essentially subtracts a scaled voxel value from its neighbor values, so that edges are non-zero values to be added to original image to sharpen[95,177,178].

3.12.3.4 Grey Scale Value Calibration

For battery XRCT, calibrating to standard units is critical for *in-situ* studies, where grey values should be consistent between scans. Therefore, phantoms and references should be used with consistent scan parameters (X-ray energy, source-to-detector distance, Beam Hardening constant, etc.) in such *in-situ* studies to ensure materials are appropriately identified. To back approximate the attenuation or absorption coefficient from grey values, one can use an imaging phantom, which is an object that is near ideal and produces no error or artifacts during a scan[90,179]. In the medical field, calibration phantoms are used to categorize materials on the Hounsfield scale, which is a transformation of the original linear attenuation scale where Air is -1000 Hounsfield units (HU) and DI water is 0 HU[179].

3.12.3.5 Descriptions of Local Segmentation Methods

The following is a description of commonly used local segmentation methods[92]. Hysteresis implements a growth model where designated voxel intensities serve as seed regions under successive iterations to assign intermediate intensity values. Indicator Kriging uses kriging or a linear combination of weighted neighborhood values to classify phases. BMRF uses a boundary surface minimization function with voxel nearest neighbors separate classes. Watershed uses intensity gradients to spatially separate phases. CAC implements Watershed with a combination of active contours by designating areas for seeding while locally applying gradient-based segmentation until all boundaries converge.

The watershed algorithm is commonly used and is based on a simple concept from nature, where the structure is imagined as a porous soil, the active particles are cavities, and the segmentation is defined as the intersection between the overspilling liquid as the cavities are filled[180]. Watershed is the most efficient when coupled to *operando* imaging. It can gives access to the dynamic evolution of objects such as the individual distribution of lithiation in each particle[55], and can be used to reduce the lithiation heterogeneity of secondary particles that causes accelerated capacity fading.

3.13 References

1. Seeram, E. Computed Tomography: A Technical Review. RADIOLOGIC TECHNOLOGY 89, 27 (2018).

2. Rubin, G. D. Computed Tomography: Revolutionizing the Practice of Medicine for 40 Years. *Radiology* 273, S45–S74 (2014).

3. Christoph, R. & Neumann, H. J. *X-ray tomography in industrial metrology precise, economical and universal*. (2011).

4. Villarraga-Gómez, H., Herazo, E. L. & Smith, S. T. X-ray computed tomography: from medical imaging to dimensional metrology. *Precision Engineering* 60, 544–569 (2019).

5. Pietsch, P. & Wood, V. X-Ray Tomography for Lithium Ion Battery Research: A Practical Guide. *Annu. Rev. Mater. Res.* 47, 451–479 (2017).

6. Heenan, T. M. M., Tan, C., Hack, J., Brett, D. J. L. & Shearing, P. R. Developments in X-ray tomography characterization for electrochemical devices. *Materials Today* 31, 69–85 (2019).

7. Gayon-Lombardo, A., Mosser, L., Brandon, N. P. & Cooper, S. J. Pores for thought: generative adversarial networks for stochastic reconstruction of 3D multi-phase electrode microstructures with periodic boundaries. *npj Comput Mater* 6, 82 (2020).

8. Petrich, L. *et al.* Crack detection in lithium-ion cells using machine learning. *Computational Materials Science* 136, 297–305 (2017).

9. Jiang, Z. *et al.* Machine-learning-revealed statistics of the particle-carbon/binder detachment in lithium-ion battery cathodes. *Nature Communications* 11, 2310 (2020).

10. Radon, J. Über die Bestimmung von Funktionen durch ihre Integralwerte längs gewisser Mannigfaltigkeiten. *Akad. Wiss.* 69, 262–277 (1917).

11. Röntgen, W. C. On a new kind of rays. *Science* 3, 227–231 (1896).

12. Knutsson, F. Röntgen and the Nobel Prize: With Notes from His Correspondence with Svante Arrhenius. *Acta Radiologica. Diagnosis* 8, 449–460 (1969).

13. Cormack, A. M. Representation of a Function by Its Line Integrals, with Some Radiological Applications. *Journal of Applied Physics* 34, 2722–2727 (1963).

14. Chiro, G. D. & Brooks, R. A. The 1979 Nobel Prize in Physiology or Medicine. *Journal of Computer Assisted Tomography* 4, 241–245 (1980).

15. Beckmann, E. C. CT scanning the early days. *The British journal of radiology* 79, 5–8 (2006).

16. Hounsfield, G. N. Computerized transverse axial scanning (tomography): Part 1. Description of system. *The British journal of radiology* 46, 1016–1022 (1973).

17. Boerckel, J. D., Mason, D. E., McDermott, A. M. & Alsberg, E. Microcomputed tomography: approaches and applications in bioengineering. *Stem Cell Res Ther* 5, 144 (2014).

18. Krüger, Ph. *et al.* Synchrotron X-ray tomography for investigations of water distribution in polymer electrolyte membrane fuel cells. *Journal of Power Sources* 196, 5250–5255 (2011).

19. Fazeli, M. *et al.* Pore network modeling to explore the effects of compression on multiphase transport in polymer electrolyte membrane fuel cell gas diffusion layers. *Journal of Power Sources* 335, 162–171 (2016).

20. Alrwashdeh, S. S. *et al. In Operando* Quantification of Three-Dimensional Water Distribution in Nanoporous Carbon-Based Layers in Polymer Electrolyte Membrane Fuel Cells. *ACS Nano* 11, 5944–5949 (2017).

21. Rawson, S. D., Maksimcuka, J., Withers, P. J. & Cartmell, S. H. X-ray computed tomography in life sciences. *BMC Biol* 18, 21 (2020).

22. Elliott, J. C. & Dover, S. D. X-ray microtomography. *Journal of Microscopy* 126, 211–213 (1982).

23. Kress, J. W. & Feldkamp, L. A. X-Ray Tomography Applied to NDE of Ceramics. in *Volume 5: Ceramics; Structures and Dynamics; Controls, Diagnostics and Instrumentation; Education; Process Industries* V005T11A003 (American Society of Mechanical Engineers, 1983). doi:10.1115/83-GT-206.

24. Stock, S. R. X-ray microtomography of materials. *International Materials Reviews* 44, 141–164 (1999).

25. Grodzins, L. Critical absorption tomography of small samples. *Nuclear Instruments and Methods in Physics Research* 206, 547–552 (1983).

26. Grodzins, L. Optimum energies for x-ray transmission tomography of small samples. *Nuclear Instruments and Methods in Physics Research* 206, 541–545 (1983).

27. Thompson, A. C. *et al.* Computed tomography using synchrotron radiation. *Nuclear Instruments and Methods in Physics Research* 222, 319–323 (1984).

28. Heiken, J. P., Brink, J. A. & Vannier, M. W. Spiral (helical) CT. *Radiology* 189, 647–656 (1993).

29. Kalender, W. A. 1.5 Spiral volumetric CT with single-breathhold technique, continuous transport, and continuous scanner rotation. *Classic Papers in Modern Diagnostic Radiology* 64, (2005).

30. Polacin, A., Kalender, W. A. & Marchal, G. Evaluation of section sensitivity profiles and image noise in spiral CT. *Radiology* 185, 29–35 (1992).

31. Rubin, G. D., Leung, A. N., Robertson, V. J. & Stark, P. Thoracic spiral CT: influence of subsecond gantry rotation on image quality. *Radiology* 208, 771–776 (1998).

32. Hu, H., He, H. D., Foley, W. D. & Fox, S. H. Four Multidetector-Row Helical CT: Image Quality and Volume Coverage Speed. *Radiology* 215, 55–62 (2000).

33. Ballabriga, R. *et al.* Photon counting detectors for X-ray imaging with emphasis on CT. *IEEE Transactions on Radiation and Plasma Medical Sciences* (2020).

34. Kruth, J. P. *et al.* Computed tomography for dimensional metrology. *CIRP Annals* 60, 821–842 (2011).

35. Steinbock, L. & Dustmann, C.-H. Investigation of the Inner Structures of ZEBRA Cells with a Microtomograph. *J. Electrochem. Soc.* 148, A132 (2001).

36. Sinha, P. K., Halleck, P. & Wang, C.-Y. Quantification of Liquid Water Saturation in a PEM Fuel Cell Diffusion Medium Using X-ray Microtomography. *Electrochem. Solid-State Lett.* 9, A344 (2006).

37. Shearing, P. R., Howard, L. E., Jørgensen, P. S., Brandon, N. P. & Harris, S. J. Characterization of the 3-dimensional microstructure of a graphite negative electrode from a Li-ion battery. *Electrochemistry communications* 12, 374–377 (2010).

38. Hutzenlaub, T., Thiele, S., Zengerle, R. & Ziegler, C. Three-dimensional reconstruction of a LiCoO2 Li-ion battery cathode. *Electrochemical and Solid State Letters* 15, A33 (2011).

39. Yan, B., Lim, C., Yin, L. & Zhu, L. Three dimensional simulation of galvanostatic discharge of LiCoO2 cathode based on X-ray nano-CT images. *Journal of The Electrochemical Society* 159, A1604 (2012).

40. Ebner, M., Marone, F., Stampanoni, M. & Wood, V. Visualization and Quantification of Electrochemical and Mechanical Degradation in Li Ion Batteries. *Science* 342, 716–720 (2013).

41. Loveridge, M. *et al.* Looking Deeper into the Galaxy (Note 7). *Batteries* 4, 3 (2018).

42. Meyer, Q. *et al.* Multi-Scale Imaging of Polymer Electrolyte Fuel Cells using X-ray Micro- and Nano-Computed Tomography, Transmission Electron Microscopy and Helium-Ion Microscopy. *Fuel Cells* 19, 35–42 (2019).

43. Maire, E. & Withers, P. J. Quantitative X-ray tomography. *International Materials Reviews* 59, 1–43 (2014).

44. Gelb, J., Finegan, D. P., Brett, D. J. L. & Shearing, P. R. Multi-scale 3D investigations of a commercial 18650 Li-ion battery with correlative electron- and X-ray microscopy. *Journal of Power Sources* 357, 77–86 (2017).

45. Finegan, D. P. *et al.* Investigating lithium-ion battery materials during overcharge-induced thermal runaway: an operando and multi-scale X-ray CT study. *Phys. Chem. Chem. Phys.* 18, 30912–30919 (2016).

46. Gelb, J. *et al.* Energy Tunability in Laboratory 3D Nano-XRM. *Microscopy and Microanalysis* 25, 388–389 (2019).

47. Rack, A. Hard X-ray Imaging at ESRF: Exploiting Contrast and Coherence with the New EBS Storage Ring. *Synchrotron Radiation News* 33, 20–28 (2020).

48. Meirer, F. *et al.* Three-dimensional imaging of chemical phase transformations at the nanoscale with full-field transmission X-ray microscopy. *J Synchrotron Rad* 18, 773–781 (2011).

49. Müller, S. *et al.* Multimodal Nanoscale Tomographic Imaging for Battery Electrodes. *Adv. Energy Mater.* 10, 1904119 (2020).

50. Yin, L. *et al.* High Performance Printed AgO-Zn Rechargeable Battery for Flexible Electronics. *Joule* 5, 228–248 (2021).

51. Pietsch, P. *et al.* Quantifying microstructural dynamics and electrochemical activity of graphite and silicon-graphite lithium ion battery anodes. *Nat Commun* 7, 12909 (2016).

52. Taiwo, O. O. *et al.* Microstructural degradation of silicon electrodes during lithiation observed via operando X-ray tomographic imaging. *Journal of Power Sources* 342, 904–912 (2017).

53. Gonzalez, J. *et al.* Three dimensional studies of particle failure in silicon based composite electrodes for lithium ion batteries. *Journal of Power Sources* 269, 334–343 (2014).

54. Vanpeene, V. *et al.* Dynamics of the Morphological Degradation of Si-Based Anodes for Li-Ion Batteries Characterized by In Situ Synchrotron X-Ray Tomography. *Adv. Energy Mater.* 9, 1803947 (2019).

55. Gent, W. E. *et al.* Persistent State-of-Charge Heterogeneity in Relaxed, Partially Charged Li1−xNi1/3Co1/3Mn1/3O2 Secondary Particles. *Advanced Materials* 28, 6631–6638 (2016).

56. Komini Babu, S., Mohamed, A. I., Whitacre, J. F. & Litster, S. Multiple imaging mode X-ray computed tomography for distinguishing active and inactive phases in lithium-ion battery cathodes. *Journal of Power Sources* 283, 314–319 (2015).

57. Chen-Wiegart, Y. K., Liu, Z., Faber, K. T., Barnett, S. A. & Wang, J. 3D analysis of a LiCoO2–Li(Ni1/3Mn1/3Co1/3)O2 Li-ion battery positive electrode using x-ray nano-tomography. *Electrochemistry Communications* 28, 127–130 (2013).

58. Heenan, T. M. M. *et al.* Resolving Li-Ion Battery Electrode Particles Using Rapid Lab-Based X-Ray Nano-Computed Tomography for High-Throughput Quantification. *Adv. Sci.* 7, 2000362 (2020).

59. Frisco, S., Kumar, A., Whitacre, J. F. & Litster, S. Understanding Li-Ion Battery Anode Degradation and Pore Morphological Changes through Nano-Resolution X-ray Computed Tomography. *J. Electrochem. Soc.* 163, A2636–A2640 (2016).

60. Su, Z. *et al.* X-ray Nanocomputed Tomography in Zernike Phase Contrast for Studying 3D Morphology of Li–O $_2$ Battery Electrode. *ACS Appl. Energy Mater.* 3, 4093–4102 (2020).

61. Lu, X. *et al.* 3D microstructure design of lithium-ion battery electrodes assisted by X-ray nano-computed tomography and modelling. *Nat Commun* 11, 2079 (2020).

62. Usseglio-Viretta, F. L. E. *et al.* Quantitative Relationships Between Pore Tortuosity, Pore Topology, and Solid Particle Morphology Using a Novel Discrete Particle Size Algorithm. *J. Electrochem. Soc.* 167, 100513 (2020).

63. Ebner, M., Chung, D.-W., García, R. E. & Wood, V. Tortuosity Anisotropy in Lithium-Ion Battery Electrodes. *Adv. Energy Mater.* 4, 1301278 (2014).

64. Xradia, Z. Versa 510 - Submicron X-ray Imaging: Maintain High Resolution Even at Large Working Distances. 14.

65. Xradia, Z. Versa 610 - Extend the Limits of Your Exploration. 40.

66. Varslot, T., Kingston, A., Myers, G. & Sheppard, A. High-resolution helical cone-beam micro-CT with theoretically-exact reconstruction from experimental data. *Medical Physics* 38, 5459–5476 (2011).

67. Li, T. *et al.* Three-Dimensional Reconstruction and Analysis of All-Solid Li-Ion Battery Electrode Using Synchrotron Transmission X-ray Microscopy Tomography. *ACS Appl. Mater. Interfaces* 10, 16927–16931 (2018).

68. Ghorbani Kashkooli, A. *et al.* Synchrotron X-ray nano computed tomography based simulation of stress evolution in LiMn2O4 electrodes. *Electrochimica Acta* 247, 1103–1116 (2017).

69. Xradia, Z. 810 Ultra - Nanoscale X-ray Imaging: Explore at the Speed of Science. 22.

70. Frisco, S. *et al.* Internal Morphologies of Cycled Li-Metal Electrodes Investigated by Nano-Scale Resolution X-ray Computed Tomography. *ACS Appl. Mater. Interfaces* 9, 18748–18757 (2017).

71. Yermukhambetova, A. *et al.* Exploring 3D microstructural evolution in Li-Sulfur battery electrodes using in-situ X-ray tomography. *Sci Rep* 6, 35291 (2016).

72. Yufit, V. *et al.* Investigation of lithium-ion polymer battery cell failure using X-ray computed tomography. *Electrochemistry Communications* 13, 608–610 (2011).

73. Taiwo, O. O. *et al.* Investigating the evolving microstructure of lithium metal electrodes in 3D using X-ray computed tomography. *Phys. Chem. Chem. Phys.* 19, 22111–22120 (2017).

74. Ito, Y., Wei, X., Desai, D., Steingart, D. & Banerjee, S. An indicator of zinc morphology transition in flowing alkaline electrolyte. *Journal of Power Sources* 211, 119–128 (2012).

75. Ko, J. S. *et al.* Robust 3D Zn Sponges Enable High-Power, Energy-Dense Alkaline Batteries. *ACS Appl. Energy Mater.* 2, 212–216 (2019).

76. Mitsch, T. *et al.* Preparation and Characterization of Li-Ion Graphite Anodes Using Synchrotron Tomography. *Materials* 7, 4455–4472 (2014).

77. Arlt, T., Schröder, D., Krewer, U. & Manke, I. *In operando* monitoring of the state of charge and species distribution in zinc air batteries using X-ray tomography and model-based simulations. *Phys. Chem. Chem. Phys.* 16, 22273–22280 (2014).

78. Yu, Y.-S. *et al.* Three-dimensional localization of nanoscale battery reactions using soft X-ray tomography. *Nat Commun* 9, 921 (2018).

79. Tonin, G. *et al.* Operando investigation of the lithium/sulfur battery system by coupled X-ray absorption tomography and X-ray diffraction computed tomography. *Journal of Power Sources* 468, 228287 (2020).

80. Lewis, J. A. *et al.* Linking void and interphase evolution to electrochemistry in solid-state batteries using operando X-ray tomography. *Nature Materials* 1–8 (2021).

81. Wang, J., Chen-Wiegart, Y. K. & Wang, J. In Situ Three-Dimensional Synchrotron X-Ray Nanotomography of the (De)lithiation Processes in Tin Anodes. *Angew. Chem. Int. Ed.* 53, 4460–4464 (2014).

82. Vanpeene, V. *et al.* Monitoring the morphological changes of Si-based electrodes by X-ray computed tomography: A 4D-multiscale approach. *Nano Energy* 74, 104848 (2020).

83. Christensen, M. K., Mathiesen, J. K., Simonsen, S. B. & Norby, P. Transformation and migration in secondary zinc–air batteries studied by in situ synchrotron X-ray diffraction and X-ray tomography. *Journal of Materials Chemistry A* 7, 6459–6466 (2019).

84. Carter, R., Huhman, B., Love, C. T. & Zenyuk, I. V. X-ray computed tomography comparison of individual and parallel assembled commercial lithium iron phosphate batteries at end of life after high rate cycling. *Journal of Power Sources* 381, 46–55 (2018).

85. Jervis, R. *et al.* In situ compression and X-ray computed tomography of flow battery electrodes. *Journal of Energy Chemistry* 27, 1353–1361 (2018).

86. Doux, J. *et al.* Stack Pressure Considerations for Room-Temperature All-Solid-State Lithium Metal Batteries. *Adv. Energy Mater.* 10, 1903253 (2020).

87. Franke-lang, R., Arlt, T., Manke, I. & Kowal, J. X-ray tomography as a powerful method for zinc-air battery research. *Journal of Power Sources* 370, 45–51 (2017).

88. Tippens, J. *et al.* Visualizing Chemomechanical Degradation of a Solid-State Battery Electrolyte. *ACS Energy Lett.* 4, 1475–1483 (2019).

89. Lu, B. *et al.* Quantitatively Designing Porous Copper Current Collectors for Lithium Metal Anode. *arXiv preprint arXiv:2102.03962* (2021).

90. Ghani, M. U. *et al.* Noise Power Characteristics of a Micro–Computed Tomography System: *Journal of Computer Assisted Tomography* 41, 82–89 (2017).

91. *Micro-computed Tomography (micro-CT) in Medicine and Engineering*. (Springer International Publishing, 2020). doi:10.1007/978-3-030-16641-0.

92. Schlüter, S., Sheppard, A., Brown, K. & Wildenschild, D. Image processing of multiphase images obtained via X-ray microtomography: A review. *Water Resour. Res.* 50, 3615–3639 (2014).

93. Barrett, J. F. & Keat, N. Artifacts in CT: Recognition and Avoidance. *RadioGraphics* 24, 1679–1691 (2004).

94. Iassonov, P. & Tuller, M. Application of Segmentation for Correction of Intensity Bias in X-Ray Computed Tomography Images. *Vadose Zone Journal* 9, 187 (2010).

95. Tuller, M., Kulkarni, R. & Fink, W. Segmentation of X-Ray CT Data of Porous Materials: A Review of Global and Locally Adaptive Algorithms. in *SSSA Special Publications* (eds. Anderson, S. H. & Hopmans, J. W.) 157–182 (American Society of Agronomy and Soil Science Society of America, 2015). doi:10.2136/sssaspecpub61.c8.

96. Carvalho, L. E., Sobieranski, A. C. & von Wangenheim, A. 3D Segmentation Algorithms for Computerized Tomographic Imaging: a Systematic Literature Review. *J Digit Imaging* 31, 799–850 (2018).

97. Serra, J. Mathematical morphology and image analysis. *SIAM, Washington DC à paraître* (1982).

98. Doyle, M., Fuller, T. F. & Newman, J. Modeling of Galvanostatic Charge and Discharge of the Lithium/Polymer/Insertion Cell. *J. Electrochem. Soc.* 140, 1526–1533 (1993).

99. Newman, J. S. & Tobias, C. W. Theoretical Analysis of Current Distribution in Porous Electrodes. *J. Electrochem. Soc.* 109, 1183 (1962).

100. Landesfeind, J., Ebner, M., Eldiven, A., Wood, V. & Gasteiger, H. A. Tortuosity of Battery Electrodes: Validation of Impedance-Derived Values and Critical Comparison with 3D Tomography. *J. Electrochem. Soc.* 165, A469–A476 (2018).

101. Trembacki, B. L. *et al.* Editors' Choice—Mesoscale Analysis of Conductive Binder Domain Morphology in Lithium-Ion Battery Electrodes. *J. Electrochem. Soc.* 165, E725–E736 (2018).

102. Duquesnoy, M., Lombardo, T., Chouchane, M., Primo, E. N. & Franco, A. A. Data-driven assessment of electrode calendering process by combining experimental results, in silico mesostructures generation and machine learning. *Journal of Power Sources* 480, 229103 (2020).

103. Chouchane, M., Rucci, A. & Franco, A. A. A Versatile and Efficient Voxelization-Based Meshing Algorithm of Multiple Phases. *ACS Omega* 4, 11141–11144 (2019).

104. GeoDict. https://www.math2market.com/.

105. Cooper, S. J., Bertei, A., Shearing, P. R., Kilner, J. A. & Brandon, N. P. TauFactor: An open-source application for calculating tortuosity factors from tomographic data. *SoftwareX* 5, 203–210 (2016).

106. Westhoff, D. *et al.* Parametric stochastic 3D model for the microstructure of anodes in lithium-ion power cells. *Computational Materials Science* 126, 453–467 (2017).

107. Kashkooli, A. G. *et al.* Multiscale modeling of lithium-ion battery electrodes based on nano-scale X-ray computed tomography. *Journal of Power Sources* 307, 496–509 (2016).

108. Yan, B., Lim, C., Yin, L. & Zhu, L. Simulation of heat generation in a reconstructed LiCoO2 cathode during galvanostatic discharge. *Electrochimica Acta* 100, 171–179 (2013).

109. Ngandjong, A. C. *et al.* Multiscale Simulation Platform Linking Lithium Ion Battery Electrode Fabrication Process with Performance at the Cell Level. *J. Phys. Chem. Lett.* 8, 5966–5972 (2017).

110. Roberts, S. A., Brunini, V. E., Long, K. N. & Grillet, A. M. A Framework for Three-Dimensional Mesoscale Modeling of Anisotropic Swelling and Mechanical Deformation in Lithium-Ion Electrodes. *J. Electrochem. Soc.* 161, F3052–F3059 (2014).

111. Ferraro, M. E., Trembacki, B. L., Brunini, V. E., Noble, D. R. & Roberts, S. A. Electrode Mesoscale as a Collection of Particles: Coupled Electrochemical and Mechanical Analysis of NMC Cathodes. *J. Electrochem. Soc.* 167, 013543 (2020).

112. Chouchane, M., Primo, E. N. & Franco, A. A. Mesoscale Effects in the Extraction of the Solid-State Lithium Diffusion Coefficient Values of Battery Active Materials: Physical Insights from 3D Modeling. *J. Phys. Chem. Lett.* 11, 2775–2780 (2020).

113. Danner, T. *et al.* Thick electrodes for Li-ion batteries: A model based analysis. *Journal of Power Sources* 334, 191–201 (2016).

114. Lim, C., Yan, B., Yin, L. & Zhu, L. Simulation of diffusion-induced stress using reconstructed electrodes particle structures generated by micro/nano-CT. *Electrochimica Acta* 75, 279–287 (2012).

115. Qiu, G. *et al.* 3-D pore-scale resolved model for coupled species/charge/fluid transport in a vanadium redox flow battery. *Electrochimica Acta* 64, 46–64 (2012).

116. Zhang, D. *et al.* The effect of wetting area in carbon paper electrode on the performance of vanadium redox flow batteries: A three-dimensional lattice Boltzmann study. *Electrochimica Acta* 283, 1806–1819 (2018).

117. Wang, M. *et al.* Numerical evaluation of the effect of mesopore microstructure for carbon electrode in flow battery. *Journal of Power Sources* 424, 27–34 (2019).

118. Zhang, D. *et al.* Understanding the role of the porous electrode microstructure in redox flow battery performance using an experimentally validated 3D pore-scale lattice Boltzmann model. *Journal of Power Sources* 447, 227249 (2020).

119. Torayev, A. *et al.* Stochasticity of Pores Interconnectivity in Li–O2 Batteries and its Impact on the Variations in Electrochemical Performance. *J. Phys. Chem. Lett.* 9, 791–797 (2018).

120. Harris, W. M. & Chiu, W. K. S. Determining the representative volume element size for three-dimensional microstructural material characterization. Part 1: Predictive models. *Journal of Power Sources* 282, 552–561 (2015).

121. Harris, W. M. & Chiu, W. K. S. Determining the representative volume element size for three-dimensional microstructural material characterization. Part 2: Application to experimental data. *Journal of Power Sources* 282, 622–629 (2015).

122. Roberts, S. A., Mendoza, H., Brunini, V. E. & Noble, D. R. A verified conformal decomposition finite element method for implicit, many-material geometries. *Journal of Computational Physics* 375, 352–367 (2018).

123. Landstorfer, M., Prifling, B. & Schmidt, V. Mesh generation for periodic 3D microstructure models and computation of effective properties. *Journal of Computational Physics* 431, 110071 (2021).

124. Chouchane, M., Rucci, A., Lombardo, T., Ngandjong, A. C. & Franco, A. A. Lithium ion battery electrodes predicted from manufacturing simulations: Assessing the impact of the carbon-binder spatial location on the electrochemical performance. *Journal of Power Sources* 444, 227285 (2019).

125. Lu, X. *et al.* Microstructural Evolution of Battery Electrodes During Calendering. *Joule* 4, 2746–2768 (2020).

126. Ngandjong, A. C. *et al.* Investigating electrode calendering and its impact on electrochemical performance by means of a new discrete element method model: Towards a digital twin of Li-Ion battery manufacturing. *Journal of Power Sources* 485, 229320 (2021).

127. Lombardo, T. *et al.* Accelerated Optimization Methods for Force-Field Parametrization in Battery Electrode Manufacturing Modeling. *Batteries & Supercaps* 3, 721–730 (2020).

128. Flannery, B. P., Deckman, H. W., Roberge, W. G. & D'amico, K. L. Three-Dimensional X-ray Microtomography. *Science* 237, 1439–1444 (1987).

129. R. Daemi, S. *et al.* 4D visualisation of in situ nano-compression of Li-ion cathode materials to mimic early stage calendering. *Materials Horizons* 6, 612–617 (2019).

130. Hubbell, J. H. & Seltzer, S. M. *Tables of x-ray mass attenuation coefficients and mass energy-absorption coefficients 1 keV to 20 meV for elements z = 1 to 92 and 48 additional substances of dosimetric interest*. https://www.osti.gov/biblio/76335 (1995).

131. Usseglio-Viretta, F. L. E. *et al.* Resolving the Discrepancy in Tortuosity Factor Estimation for Li-Ion Battery Electrodes through Micro-Macro Modeling and Experiment. *J. Electrochem. Soc.* 165, A3403–A3426 (2018).

132. Bailey, J. J. *et al.* Laser-preparation of geometrically optimised samples for X-ray nano-CT. *Journal of Microscopy* 267, 384–396 (2017).

133. Tan, C. *et al.* Evolution of Electrochemical Cell Designs for In-Situ and Operando 3D Characterization. *Materials* 11, 2157 (2018).

134. Nelson, J. *et al.* Identifying and managing radiation damage during in situ transmission x-ray microscopy of Li-ion batteries. in *X-Ray Nanoimaging: Instruments and Methods* vol. 8851 88510B (International Society for Optics and Photonics, 2013).

135. Borkiewicz, O. J., Wiaderek, K. M., Chupas, P. J. & Chapman, K. W. Best Practices for Operando Battery Experiments: Influences of X-ray Experiment Design on Observed Electrochemical Reactivity. *J. Phys. Chem. Lett.* 6, 2081–2085 (2015).

136. P. Finegan, D. *et al.* Spatial dynamics of lithiation and lithium plating during high-rate operation of graphite electrodes. *Energy & Environmental Science* 13, 2570–2584 (2020).

137. Pietsch, P., Hess, M., Ludwig, W., Eller, J. & Wood, V. Combining operando synchrotron X-ray tomographic microscopy and scanning X-ray diffraction to study lithium ion batteries. *Scientific Reports* 6, 27994 (2016).

138. Finegan, D. P. *et al.* Spatially Resolving Lithiation in Silicon–Graphite Composite Electrodes via in Situ High-Energy X-ray Diffraction Computed Tomography. *Nano Lett.* 19, 3811–3820 (2019).

139. Burnett, T. L. *et al.* Correlative Tomography. *Sci Rep* 4, 4711 (2015).

140. Slater, T. J. A. *et al.* Multiscale correlative tomography: an investigation of creep cavitation in 316 stainless steel. *Sci Rep* 7, (2017).

141. Apeleo Zubiri, B. *et al.* Correlative Laboratory Nano-CT and 360° Electron Tomography of Macropore Structures in Hierarchical Zeolites. *Advanced Materials Interfaces* 2001154 (2020).

142. Daemi, S. R. *et al.* Visualizing the Carbon Binder Phase of Battery Electrodes in Three Dimensions. *ACS Appl. Energy Mater.* 1, 3702–3710 (2018).

143. Xu, H., Usseglio-Viretta, F., Kench, S., Cooper, S. J. & Finegan, D. P. Microstructure reconstruction of battery polymer separators by fusing 2D and 3D image data for transport property analysis. *Journal of Power Sources* 480, 229101 (2020).

144. De Carlo, F. *et al.* TomoBank: a tomographic data repository for computational x-ray science. *Meas. Sci. Technol.* 29, 034004 (2018).

145. UNICORE | Distributed computing and data resources. https://www.unicore.eu/.

146. Franco, A. A. *et al.* Entering the Augmented Era: Immersive and Interactive Virtual Reality for Battery Education and Research**. *Batteries & Supercaps* 3, 1147–1164 (2020).

147. Stephenson, D. E. *et al.* Modeling 3D Microstructure and Ion Transport in Porous Li-Ion Battery Electrodes. *J. Electrochem. Soc.* 158, A781 (2011).

148. Shi, T. *et al.* Characterization of mechanical degradation in an all-solid-state battery cathode. *J. Mater. Chem. A* 8, 17399–17404 (2020).

149. Burnett, T. L. *et al.* Large volume serial section tomography by Xe Plasma FIB dual beam microscopy. *Ultramicroscopy* 161, 119–129 (2016).

150. Winiarski, B. Plasma FIB Spin Milling Accelerates Battery Research. *Microscopy and Microanalysis* 26, 2226–2227 (2020).

151. Kisielowski, C. *et al.* Detection of Single Atoms and Buried Defects in Three Dimensions by Aberration-Corrected Electron Microscope with 0.5-Å Information Limit. *Microscopy and Microanalysis* 14, 469–77 (2008).

152. Wang, X., Li, Y. & Meng, Y. S. Cryogenic Electron Microscopy for Characterizing and Diagnosing Batteries. *Joule* 2, 2225–2234 (2018).

153. Lee, J. Z. *et al.* Cryogenic Focused Ion Beam Characterization of Lithium Metal Anodes. *ACS Energy Lett.* 4, 489–493 (2019).

154. Cheng, D. *et al.* Unveiling the Stable Nature of the Solid Electrolyte Interphase between Lithium Metal and LiPON via Cryogenic Electron Microscopy. *Joule* 4, 2484–2500 (2020).

155. Wen, J. G. *et al.* Analytical electron microscopy of Li1.2Co0.4Mn0.4O2 for lithium-ion batteries. *Solid State Ionics* 182, 98–107 (2011).

156. Pillatsch, L., Östlund, F. & Michler, J. FIBSIMS: A review of secondary ion mass spectrometry for analytical dual beam focussed ion beam instruments. *Progress in Crystal Growth and Characterization of Materials* 65, 1–19 (2019).

157. Harvey, S. P. *et al.* Sodium Accumulation at Potential-Induced Degradation Shunted Areas in Polycrystalline Silicon Modules. *IEEE J. Photovoltaics* 6, 1440–1445 (2016).

158. Lausch, D. *et al.* Sodium Outdiffusion from Stacking Faults as Root Cause for the Recovery Process of Potential-induced Degradation (PID). *Energy Procedia* 55, 486–493 (2014).

159. Farbod, B. *et al.* Anodes for Sodium Ion Batteries Based on Tin–Germanium–Antimony Alloys. *ACS Nano* 8, 4415–4429 (2014).

160. Harris, S. J. & Lu, P. Effects of Inhomogeneities—Nanoscale to Mesoscale—on the Durability of Li-Ion Batteries. *J. Phys. Chem. C* 117, 6481–6492 (2013).

161. Gauthier, N., Courrèges, C., Demeaux, J., Tessier, C. & Martinez, H. Probing the in-depth distribution of organic/inorganic molecular species within the SEI of LTO/NMC and LTO/LMO batteries: A complementary ToF-SIMS and XPS study. *Applied Surface Science* 501, 144266 (2020).

162. Benninghoven, A., Rudenauer, F. G. & Werner, H. W. Secondary ion mass spectrometry: basic concepts, instrumental aspects, applications and trends. (1987).

163. Zinner, E. Depth profiling by secondary ion mass spectrometry. *Scanning* 3, 57–78 (1980).

164. Epstein, N. On tortuosity and the tortuosity factor in flow and diffusion through porous media. *Chemical Engineering Science* 44, 777–779 (1989).

165. Tjaden, B., Brett, D. J. L. & Shearing, P. R. Tortuosity in electrochemical devices: a review of calculation approaches. *International Materials Reviews* 63, 47–67 (2018).

166. Chung, D.-W., Ebner, M., Ely, D. R., Wood, V. & García, R. E. Validity of the Bruggeman relation for porous electrodes. *Modelling Simul. Mater. Sci. Eng.* 21, 074009 (2013).

167. Amira-Avizo Software | Use Case Gallery | Thermo Fisher Scientific. https://cases.amira-avizo.com/.

168. Nguyen, T.-T. *et al.* The electrode tortuosity factor: why the conventional tortuosity factor is not well suited for quantifying transport in porous Li-ion battery electrodes and what to use instead. *npj Comput Mater* 6, 123 (2020).

169. Torayev, A., Magusin, P. C. M. M., Grey, C. P., Merlet, C. & Franco, A. A. Importance of Incorporating Explicit 3D-Resolved Electrode Mesostructures in Li–O $_2$ Battery Models. *ACS Appl. Energy Mater.* 1, 6433–6441 (2018).

170. Ding, N. *et al.* Influence of carbon pore size on the discharge capacity of Li–O $_2$ batteries. *J. Mater. Chem. A* 2, 12433–12441 (2014).

171. Kingston, A. M. *et al.* Space-Filling X-Ray Source Trajectories for Efficient Scanning in Large-Angle Cone-Beam Computed Tomography. *IEEE Transactions on Computational Imaging* 4, 447–458 (2018).

172. Sijbers, J. & Postnov, A. Reduction of ring artefacts in high resolution micro-CT reconstructions. 8.

173. Willemink, M. J. & Noël, P. B. The evolution of image reconstruction for CT—from filtered back projection to artificial intelligence. *Eur Radiol* 29, 2185–2195 (2019).

174. Hsieh, J., Molthen, R. C., Dawson, C. A. & Johnson, R. H. An iterative approach to the beam hardening correction in cone beam CT. *Med. Phys.* 27, 23–29 (2000).

175. Buades, A., Coll, B. & Morel, J.-. A non-local algorithm for image denoising. in *2005 IEEE Computer Society Conference on Computer Vision and Pattern Recognition (CVPR'05)* vol. 2 60–65 vol. 2 (2005).

176. Perona, P. & Malik, J. Scale-space and edge detection using anisotropic diffusion. 11.

177. Russ, J. C., Matey, J. R., Mallinckrodt, A. J. & McKay, S. The Image Processing Handbook. 3.

178. Gonzalez, R. C., Woods, R. E. & Eddins, S. Image segmentation. *Digital image processing* 2, 331–390 (2002).

179. Feeman, T. G. *The Mathematics of Medical Imaging*. (Springer International Publishing, 2015). doi:10.1007/978-3-319-22665-1.

180. Meyer, F. Topographic distance and watershed lines. *Signal Processing* 38, 113–125 (1994).

Chapter 4. Aqueous Zn-AgO Battery Failure Investigation with *In-Situ* X-ray MicroCT

To meet the growing global energy demands, the degradation mechanisms of energy storage devices must be better understood to improve performances. As a non-destructive tool, X-ray Computed Tomography (CT) has been increasingly used by the battery community to perform *in-situ* experiments that can investigate dynamic phenomena. However, few have used X-ray CT to study representative battery systems over long cycle lifetimes (>100 cycles). Here, we report the *in-situ* CT study of Zn-Ag batteries and demonstrate the effects of current collector corrosion over long-term storage and cycling. We develop performance representative *in-situ* CT cells that can achieve >250 cycles at a high areal capacity of 12.5 mAh/cm^2. Combined with electrochemical experiments, the effects of current collector parasitic gassing are revealed with micro-scale CT (MicroCT). The volume expansion and evolution of ZnO and Zn depletion is quantified with cycling and elevated temperature testing. The experimental insights are then utilized to develop larger form-factor (4 cm^2) cells with electrochemically compatible current collectors. With this, we demonstrate >250 cycles at a high capacity of 12 mAh/cm^2 for a 4 cm^2 form. We achieve a cycling volumetric energy density of 104.7 Wh/L and a power density of 34.6 W/cm^3. The results of this work show the capabilities of *in-situ* X-ray CT in long cycle-lifetime studies that can also be applied to a multitude of other battery chemistries to improve their performances.

4.6 Introduction

To address the growing energy concerns, high performance and cost-effective energy storage solutions, such as batteries, need to be developed to enable technologies such as in grid storage, Internet of Things (IoT), and high power electronics.[1–3] While Li-Ion Batteries (LIBs) have received considerable attention due to their high energy densities, there are significant concerns surrounding the safety, recyclability, CO_2 footprint, and mining ethics of precious metals that warrant the development of alternative chemistries.[4–9] With the benefit of lower material costs, benign chemistry, nonflammable materials, ambient processability, and high theoretical energy density (820 mAh/g_{Zn}, 5,854 Ah/L), aqueous zinc batteries (aqZB)[10] are a promising alternative to LIBs.[11–15] Due to the higher ionic conductivities of the aqueous electrolytes (~1 mS/cm for LIB, ~100 mS/cm for aqueous ZBs),[12,13] aqZBs demonstrate superior performances in high current and pulse discharge applications in areas such as electric vehicles[16] and high power electronics.[17,18] Moreover, the benign chemistry and ambient processability allow for the development of flexible and stretchable batteries with easily adjustable form factors for applications in health monitoring and wearable electronics.[17,19–21]

However, aqZBs suffer from poor cyclability and shelf-life, which originate from issues such as Zn anode shape change, dendrite growth, Zn dissolution, and parasitic gassing.[20,22–25] To improve performances, several strategies have been used to stabilize the anode and limit dendrite growth and anode shape change, such as the incorporation of additives in the electrode and electrolyte *(e.g,* Bi_2O_3[26,27], CTAB[28], and polyethylene glycol (PEG)[13,23,29]) and the development of novel 3D Zn sponge structures[16,30,31]. However, a deeper fundamental understanding of the anode degradation is needed to better improve performances.

The instability and corrosion of the Zn anode in basic electrolytes results in gassing and hydrogen evolution reactions (HER) (equations 1-2),[32,33]

$$\mathrm{Zn} + \mathrm{H_2O} \rightarrow \mathrm{ZnO} + \mathrm{H_2} \qquad 0.420\ \mathrm{V\ vs.\ SHE} \qquad (1)$$

$$\mathrm{Zn} + 2\mathrm{H_2O} \rightarrow \mathrm{H_2} + \mathrm{Zn(OH)_2} \qquad 0.417\ \mathrm{V\ vs.\ SHE} \qquad (2)$$

where SHE refers to the standard hydrogen electrode. As a result, electrolyte additives such as ZnO and LiOH are often employed to limit hydrogen evolution reactions (HER) and anode corrosion.[13] Cathode materials in aqZBs tend to suffer from oxygen evolution reactions (OER) caused by high cathode potentials.[34] For instance in Zn-Ag batteries, AgO offers a higher open circuit voltage (OCP) than Ag_2O (1.86 V for AgO vs. 1.56 V for Ag_2O) at nearly double the theoretical capacity (430 mAh/g for AgO vs. 230 mAh/g for Ag_2O) and has demonstrated a high areal capacity of 50 mAh/cm^2 in a printable and flexible architecture.[17,35–37] However, as shown in equations (3-4), OER can facilitate AgO decomposition, resulting in capacity fade and self-discharge in Zn-AgO batteries.[38,39]

$$2\mathrm{AgO} + \mathrm{H_2O} + 2\mathrm{e^-} \rightleftarrows \mathrm{Ag_2O} + 2(\mathrm{OH})^- \qquad 0.604\ \mathrm{V\ vs.\ SHE} \qquad (3)$$

$$2(\mathrm{OH})^- \rightleftarrows \mathrm{H_2O} + \frac{1}{2}\mathrm{O_2} + 2\mathrm{e^-} \qquad 0.401\ \mathrm{V\ vs.\ SHE} \qquad (4)$$

$$2\mathrm{AgO} \rightarrow \mathrm{Ag_2O} + \frac{1}{2}\mathrm{O_2} \qquad (5)$$

OER can also increase the amount of dissolved oxygen in the electrolyte, facilitating the corrosion of the Zn anode.[40] Furthermore, both OER and HER of non-active materials in contact with the electrolyte, such as the current collectors, can limit the electrochemical performances of aqZBs[41]. As Bonnick and Dahn showed, the corrosion and gassing of the current collectors and casing in Ni-Zn coin cells can drastically influence the cycle life.[42]

To investigate these degradation mechanisms, X-ray CT has been increasingly used in zinc-based battery research as a tool to probe and quantify valuable 3D morphological parameters, such as porosity and particle distribution.[43–45]. For example, CT has been used to show how the solid volume fraction in 3D porous Zn structures can improve the Zn Depth-of-Discharge (DoD_{Zn}) and energy density of anodes.[43]. Additionally, CT is ideal for *in-situ* or *operando* studies due to its non-destructive nature, and since grey values in images are proportional to the material's X-ray attenuation, species can often be separated to observe the chemical evolution in electrodes. Franke-Lang *et al.*, for example, were able to distinguish Zn from ZnO, and used *in-situ* CT to visually investigate the degradation and volume expansion of a zinc-air battery.[43] Likewise, Tobias *et al.* used o*perando* CT to reveal Zn particle depletion to follow a core-shell model, in which the ZnO continuously grows around and depletes the Zn particle core.[44]

Most *in-situ* CT studies are limited to only the first few cycles,[46,47] with few reports of long cycle life studies (>100 cycles), representative of practical battery operation.[48] Herein, we used *in-situ* micro-scale X-ray CT (MicroCT) to study the effects of current collector corrosion and parasitic gassing on the performance of printed Zn-AgO batteries. As detailed in **Figure 4.1**, we developed *in-situ* CT cells that are representative of previously reported cell performances[17] to provide high resolution scans and detailed analysis of the battery system. This CT cell design allows for longer cycling (> 250 cycles) and was used to investigate the Zn particle development and growth of ZnO *in-situ* with cycling. Finally, we showed how the insights of this study can be applied to larger scale devices by demonstrating improved shelf and cycle life of a printed Zn-AgO battery.

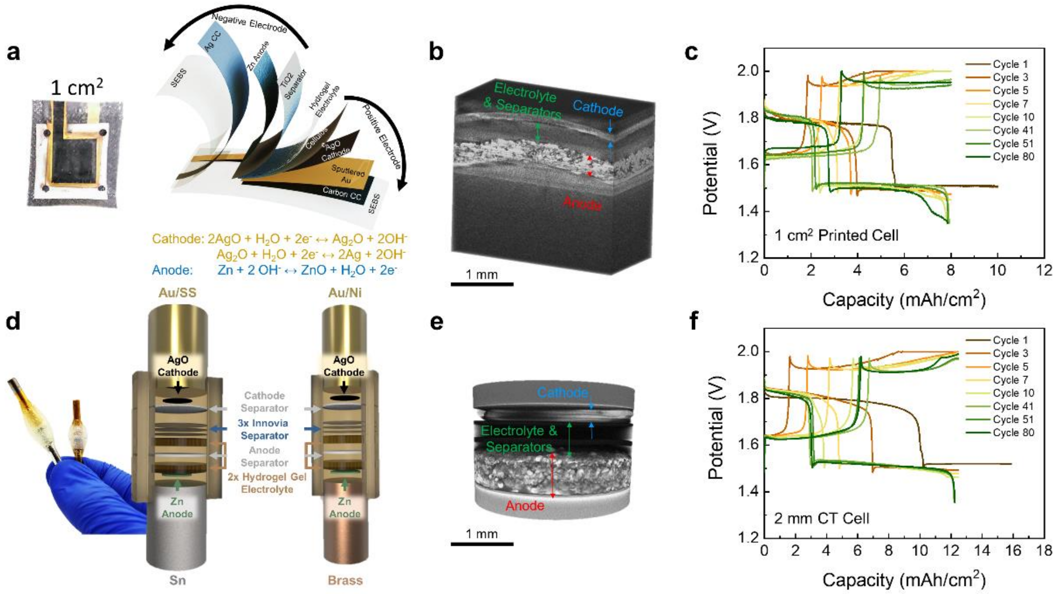

Figure 4.1 | Comparison of the cell design and performances of the Zn-AgO printed cell (top - adapted from Lu, Scharf *et al.*[17]) and *in-situ* CT cell (bottom). Comparison of cell architecture (a, d), 3D X-ray CT tomographic reconstructions (b, e), and electrochemical performances (c, f) for Zn-AgO printed cell (top row) and *in-situ* CT cell (bottom row).

4.7 Experimental Section

4.7.1 Fabrication and Synthesis of Cell Components

The electrodes were fabricated similar to our previous work.[17] A binder resin was prepared by dissolving 1 g GBR-6005 fluorine rubber in 2.75 g acetone. The cathode slurry was prepared by mixing 0.95 g AgO powder and 0.05 g Super-P powder, followed by adding 1.25 g binder resin and mixing in a planetary mixer (Flaktak SpeedmixerTM DAC 150.1 FV) at 2500 rotations per minute (rpm) for 10 min. The anode slurry was prepared by mixing 0.91 g Zn powder and 0.09 g Bi_2O_3 powder, followed by adding 0.25 g binder resin and mixing in a planetary mixer at 1800 rpm for 5 min. Both slurries were then casted using a doctor blade, cured at 80 °C for 30 min, and trimmed into the desired shape for later use.

The synthesis of the PVA hydrogel is adapted from previous work.[17] A PVA solution was prepared by dissolving 1 g of PVA in 5 g of deionized water, and a hydroxide solution was prepared by dissolving 0.2g $Ca(OH)_2$, 0.109 g LiOH and 5 g KOH in 26.159 g deionized water and removing any precipitated solid. The hydroxide solution was then added to the PVA solution in a 15.775: 10 weight ratio while stirring to obtain the hydrogel precursor. The precursor is then placed in a Patri dish in a vacuum desiccator to dry and crosslink until only 27.62% of the original weight was left. The gel was then cut to the desired size and stored in a 10 M KOH + 0.6 M LiOH solution at 20 °C.

4.7.2 CT Cell Construction

The *in-situ* cells were constructed using PTFE tubing with a 4 mm and 3 mm inner diameter for the Sn-Au/SS and Brass-Au/Ni respectively. The following metallic current collector rods were purchased from McMaster-Carr: 18-8 stainless steel, grade 2 titanium, 400 nickel, 360 brass, and 110 Copper. The Sn rods were fabricated in-house by melting lead free solder (99% Sn, .3% Ag, .7% Cu) and using the PTFE tubes as molds for making 4 mm and 3 mm inner diameter rods. Gold electroplating was performed on the cathode rods using commercial plating solutions.[49] Before plating, the rods were first electro-cleaned at -2 V vs. stainless steel for 2 minutes. The stainless-steel rods then underwent an extra nickel strike step for 2 min at -2 V vs. stainless steel to help with the adhesion of the Au. Lastly, the rods were electroplated using a potassium aurocyanide solution by applying -1.5 V vs. a platinum counter electrode for 20 minutes. The calculated thickness from the coulomb count and the surface area of the rods was determined to be ~500 nm. A picture of all the current collector rods is presented in **Figure S4.1a**.

The active material was punched smaller than the current collectors, with a 2 mm diameter, and placed directly onto the rods. For a direct comparison of the device performance, both devices in the *in-situ* study of **Figure 4.3** used the same batch of anode and cathode. Similarly, the active material used the CT cells in **Figure 4.5** were of the same batch. Commercial separators were supplied by ZPower LLC., and are as follows: (1) Flexible Alkaline Separator (FAS) film was used as the anode separator and consists of a microporous polyolefin film with an inorganic filler[50], (2) a cellophane-based film (Innovia Films Company) that was used to help block silver migration,[51,52] and (3) a porous microporous EVOH film to separate the cellophane separator from the cathode. The order of layers for the *in-situ* cells is outlined in **Figure 4.1d**. The hydrogel electrolyte and separators were punched to the size of the tube diameter, larger than the active material to prevent crossover of Zn and Ag species around the edges. A 60% weight ratio of gel electrolyte to active material was found to properly wet electrodes for adequate cycling. The anode-cathode ratio was kept at approximately 5:1 to cycle the anode at ~10% DoD_{Zn}. For consistency, the same weight percentages and ratios of the active material and electrolyte were used for the $4cm^2$ form factor cells. After assembly, commercial epoxy (Gorilla Glue) was used to seal the cells from end to end to avoid electrolyte leakage.

4.7.3 $4cm^2$ Form-Factor Cell Construction

The larger form factor cells were constructed with 4 cm^2 metal foil current collectors with a 0.4 cm × 3 cm tab to allow for electrical contact (See **Figure S4.5a**). The foils were placed on a Styrene-ethylene-butylene-styrene (SEBS) thermo-elastomer substrate with epoxy (Gorilla glue) applied to the tab regions to allow for better sealing of the metals. Following this, the active materials were added atop the foils with 25 µL of liquid electrolyte (10M KOH, 0.6M LiOH) applied to the cathode to enhance wetting. Next, the PVA hydrogel electrolyte and separators were added. The anode and cathode stacks were then joined, and the SEBS sheets were vacuum- and heat-sealed (**Figure S4.5b**). A final layer of wear-resistant nylon (McMaster-Carr) was then added and vacuum and heat sealed outside the SEBS sheets to ensure robust sealing. The final cell measure 3.5 x 3.5 cm^2 with a thickness of 2.05 mm, and an active area of 2 x 2 cm^2.

The following metal foils were used in the assembly of the 4 cm^2 cells and in electrochemical testing: 18-8 stainless steel (McMaster-Carr), 99.99% titanium (Amazon), nickel 200/201 (McMaster-Carr), 260 brass (McMaster-Carr), 99.99% Copper (MTI), and 99.99% Tin (Amazon) with thicknesses of 25-30 µm. For the gold coated foils, ~500 nm of Au was sputtered with a thin Ti adhesion layer at an Ar gas flow rate of 16 SCCM and a DC power of 200 W and 300 W for the Au and Ti respectively. The sputtering was performed with a Denton Discovery 635 Sputter System (Denton Discovery 635 Sputter System, Denton Vacuum, LLC, Moorestown, NJ, USA).

4.7.4 Cell Cycling Protocol

All cells followed the same cycling protocol and were cycled using Neware BTS4000-5V10mA (dual range) and BTS4000-5V50mA (dual range) systems. In the first cycle, cells were initially discharged with a constant current to 60% of the cathode theoretical capacity. Following this, cells were cycled at 50% of the cathode capacity with a voltage cutoff of 1.35 V when discharging, and a 2V constant voltage limit during charging to limit OER and water splitting. The *in-situ* cells were initially discharged during the first cycle at C/10 (1.25 mA/cm^2) and then cycled at C/5 (2.5 mA/cm^2) for the remainder of the cell life. The 4 cm^2 form factor cells were initially discharged at C/10 and then cycled at C/5 for 10 cycles before cycling at the specified rate (*i.e.* C/3 or 4.2 mA/cm^2). The self-discharge rate was determined by letting the 4 cm^2 cells rest for 1, 2, 3, and 4 weeks at room temperature (**Figure S4.6c,d**) before discharging them at 2 mA (0.5 mA/cm^2 or C/50) to a voltage cutoff of 1 V.

The open circuit potential (OCP) measurements presented in **Figure 4.5** were performed using a Landt battery test system (Landt Instruments CT2001A). The cell open circuit voltage was measured every 1 hour. DCIR used to probe the DC resistance was performed using a 5 mA/10mA pulse. The elevated temperature OCP was performed using a temperature chamber with precise control from 0 °C to 65 °C. Galvanostatic-EIS (GEIS) measurements were performed on both the *in-situ* and 4 cm^2 cells using a Biologic-SP150 Potentiostat. Scans were performed from 1 MHz to 1 Hz with 10 points per decade, an average of 8 measures per frequency, and an AC amplitude of 30 µA and 200 µA for *in-situ* CT cells and 4 cm^2 cells respectively.

Cyclic voltammetry (CV) and chronoamperometry (CA) measurements were performed in an aqueous electrolyte (10M KOH, 0.6M LiOH) in a three-electrode configuration with a Hg/HgO reference electrode and a platinum foil counter electrode. The electrochemical stability of the foils was tested first with a 1minute OCP to ensure stability of the reference electrode and was followed by 5 cycles of CV (**Figure S4.8**). The anode was scanned from -1.0 V to -1.5 V vs. Hg/HgO at a rate of 100 mV/s and the cathode from 0.0 V to 0.7 V vs. Hg/HgO at a rate of 10 mV/s. Following this, CA was applied for 2 minutes at the following potentials with a 1 min OCP performed in between: (1) -1.35 V, -1.39 V, and -1.45 V vs. Hg/HgO for the anode current collectors, (2) 0.2 V, 0.5 V, and 0.6 V vs. Hg/HgO for the cathode current collectors.

4.7.5 X-ray CT Experimentation and Analysis

The scans were performed with a *ZEISS Xradia 510 Versa* MicroCT instrument, and parameters were kept consistent between each scan at the various SOCs. An X-ray energy of 140 kV was used at 10 W (71.56 µA) with a voxel size of 2.504 µm, a FOV of 2.48 mm x 2.52 mm, a 1.5 hr scan time, a 4X magnification, an exposure time of 2 s, a binning of 2, and 1600 projections. The source to detector distance was also kept the same at 30.80 mm to ensure similar grey values between scans. No beam hardening correction was necessary during reconstruction. The two *in*-situ CT cells in **Figure 4.3** were scanned at the end of the discharge at different points of cycling: (1) after cycles 11 and 30 for the Sn-Au/SS cell and (2) after cycles 11, 30, 51, and 101 for the

Brass-Au/Ni cell. The initial or pristine case was performed on the bare anode from the same batch used in the respective cells (**Figure S4.2a**).

MicroCT data analysis was performed with Amira 2019 commercial software. Tomograms from the same device, but scanned at different cycles, were aligned using the "Register Images" module which uses an iterative optimization algorithm to align datasets.[53–56] After alignment, the datasets were cropped with a 600 x 600 pixel window (1.5 mm x 1.5 mm) in the XY direction to remove edge effects (**Figure S4.9**). With thresholding and area selection interpolation, the anode was analyzed separately by segmenting out the electrolyte and current collector regions above and below the anode in the Z direction. The volume of each anode was then analyzed, and the average thickness determined by dividing the total anode volume by the XY window.

Once segmented, the following Amira filters were applied to the reference and every anode analyzed to ensure grey-scale values were comparable: (1) Non-Local Means (2) Unsharp Mask (3) Delineate. As shown in **Figure S4.3b**, once filtered, 3 distinct peaks pertaining to the Zn, ZnO, and Electrolyte-Binder-Pore (EBP) regions are visible. Global thresholding was then used to separate the three regions, and the "Volume Fraction" module was implemented to quantify the percentage of each species within the anode. The "Separate Objects" module, which implements a combination of watershed, distance transforms, and numerical reconstruction algorithms, was used on the Zn region to separate the particles.

4.3 Results and Discussion

4.3.1 Current Collector Parasitic Gassing

In the Zn-AgO system, the redox reaction relies on the dissolution of zinc and silver species in the alkaline electrolyte and their supersaturation-induced precipitation, which takes place rapidly while maintaining a stable voltage (Equation 6-12):[37,38,57,58]

Anode

(Dissolution)
$$\mathrm{Zn\ (s) + 4OH^- \ (aq) \leftrightarrow Zn(OH)_4^{2-}\ (aq) + 2e^-} \tag{6}$$

(Relaxation)
$$\mathrm{Zn(OH)_4^{2-}\ (aq) \leftrightarrow ZnO\ (s) + H_2O\ +\ 2OH^-\ (aq)} \tag{7}$$

(Overall)
$$\mathrm{Zn\ (s) + 2OH^-\ (aq) \leftrightarrow ZnO\ (s) + H_2O + 2e^-} \quad -1.260\ \mathrm{V\ vs.\ SHE} \tag{8}$$

Cathode

(Dissolution)
$$\mathrm{Ag\ (s) + OH^-\ (aq) \leftrightarrow AgOH\ (aq) + e^-} \tag{9}$$

(Relaxation)
$$\mathrm{2AgOH\ (aq) \leftrightarrow Ag_2O\ (s) +\ H_2O} \tag{10}$$

(1st Transition)
$$\mathrm{Ag_2O + H_2O + 2e^- \leftrightarrow 2Ag + 2(OH)^-} \quad 0.345\ \mathrm{V\ vs. SHE} \tag{11}$$

(2nd Transition)
$$\mathrm{2AgO + H_2O\ + 2e^- \leftrightarrow Ag_2O +\ 2(OH)^-} \quad 0.604\ \mathrm{V\ vs. SHE} \tag{12}$$

As shown in **Figure 4.1c,f**, the first plateau corresponds to the first phase transition from AgO to Ag_2O (equation 11), while the second corresponds to the transition from Ag_2O to Ag (equation 12). To test the effects of OER and HER of current collect materials typically used in aqZBs,[42] the current due to gassing was monitored through chronoamperometry (CA) and by applying potentials relevant to the reactions indicated above. The current density of the OER after applying cathode-relevant potentials for 2 minutes on metal current collector rods is presented in **Figure 4.2a**. Here, 0.2 V and 0.5 V vs. Hg/HgO corresponds to the first and second plateau of the cathode phase transition at 1.56 V and 1.86 V vs. Zn/ZnO respectively (equations 11 and 12), and can be seen in **Figure S4.7a** at the minima points of the Tafel plot of the cathode. Likewise, **Figure 4.2b** shows the HER current density after a potential hold at the anode potentials indicated in the Tafel plot of the anode in **Figure S4.7b.** The same method was also used to test standard metal foils and the results are shown along with the cyclic voltammetry (CV) in **Figure S4.2**.

These results reveal higher OER gassing currents for bare materials than when electroplated with Au, which can also be seen in **Figure S4.8g** for metal foils that were sputtered with Au. However, the Au coated Ni (Au/Ni) yielded lower OER gassing currents than the Au coated Ti (Au/Ti) and Au coated stainless steel (Au/SS). On the anode end, brass and Sn rods were tested and compared. Brass rods were selected and used in the CT cells since they yielded lower HER gassing currents than copper when testing metal foils (**Figure S4.8h**). Brass rods showed lower HER currents than Sn but were similar in magnitude in the higher potential region (-1.45V vs. Hg/HgO).

To test the cycle reversibility of the anode with the different current collectors, Zn symmetric CT cells with Sn and brass rods were cycled at various DoD_{Zn} (**Figure 4.2c-d**). The anode films were initially discharged to half the desired DoD_{Zn} with a Potentiostat in the basic electrolyte and then assembled in symmetric cells (**Figure S4.4**). The first discharge was set to half the desired DoD_{Zn} to fully discharge one side to the set value and charge the other back to 0%.

The cell was then cycled at the full desired DoD_{Zn}. As expected, a general trend was observed for both cases, in which higher DoD_{Zn} yielded less cyclability. The general failure mode for these cells appears to be capacity fade due to an over oxidation of Zn and a build up a ZnO. However, cell shorting was observed for the brass-brass 40% DoD shown in **Figure 2d** and **Figure S4e**. Yet, in both cases, the symmetric cells were able to cycle >100 cycles for a DoD of 10%, with the brass-brass symmetric cell achieving over 550 cycles. These results indicate good reversibility of the anode and suggest that the likely causes for failure in full cells originate at the cathode.

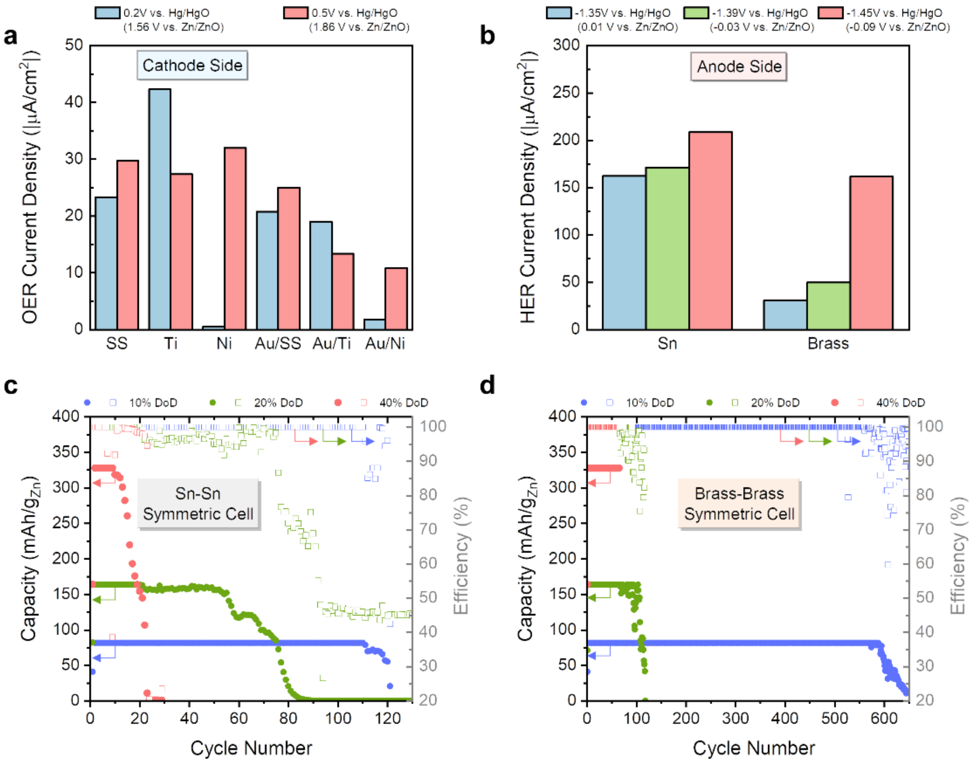

Figure 4.2 | Current collector gas evolution. Gassing currents after 2 minutes of chronoamperometry for OER at cathode relevant potentials (a) and HER at anode relevant potentials (b). Anode symmetric cell cycling performances with Sn current collectors (c) and brass current collectors (d).

4.3.2 In-Situ micro-CT Analysis

The performance of full cells was evaluated using *in-situ* MicroCT with two sets of current collectors, Sn with Au/SS rods (Sn-Au/SS) and brass with Au/Ni rods (Brass-Au/Ni), in order to determine the effects of current collector corrosion and gassing. The architecture (**Figure 4.1d**) of the 2 mm diameter *in-situ* cells were optimized to limit common issues, such as dendrite growth (**Figure S4.1c-d**), so as to be representative of larger form factor performances. As shown in **Figure 4.3**, CT full cells were scanned *in-situ* at various points of cycling. The various phases in the anode were separated using a reference containing Zn and ZnO powder (**Figure S4.3**), and grey-value global thresholding was used to segment the Zn particles from the ZnO and the electrolyte-binder-pore (EBP) region as detailed in the methods section. A visualization of the segmentation process for the Sn-Au/SS case can be seen in **Video S4.1**.

The Sn-Au/SS CT full cell was only able to achieve ~25 cycles, while the cell with less corrosive Brass-Au/Ni current collectors lasted ~125 cycles before starting to exhibit capacity fade. The various species (Zn, ZnO, and EPB) are colorized in the XZ cross-sectional slices and 3D tomograms of **Figure 4.3c-d**. The quantitative analysis is presented in **Figure 4.4a**: it reveals an increase of ZnO with cycling for both cells, confirmed by the increasing impedance of both cells during cycling (**Figure S4.1f**) resulting from the buildup of the insulating ZnO. The XZ slices show a clear increase of ZnO formation (along with a decrease of Zn) near the current collectors, whereas Zn particles near the electrolyte interface are retained at longer cycle lifetimes. This disproportionate depletion of Zn and growth of ZnO near the metal interface could suggest the effects of current collector corrosion or electron transport limitations in the depletion of the active material at the anode.

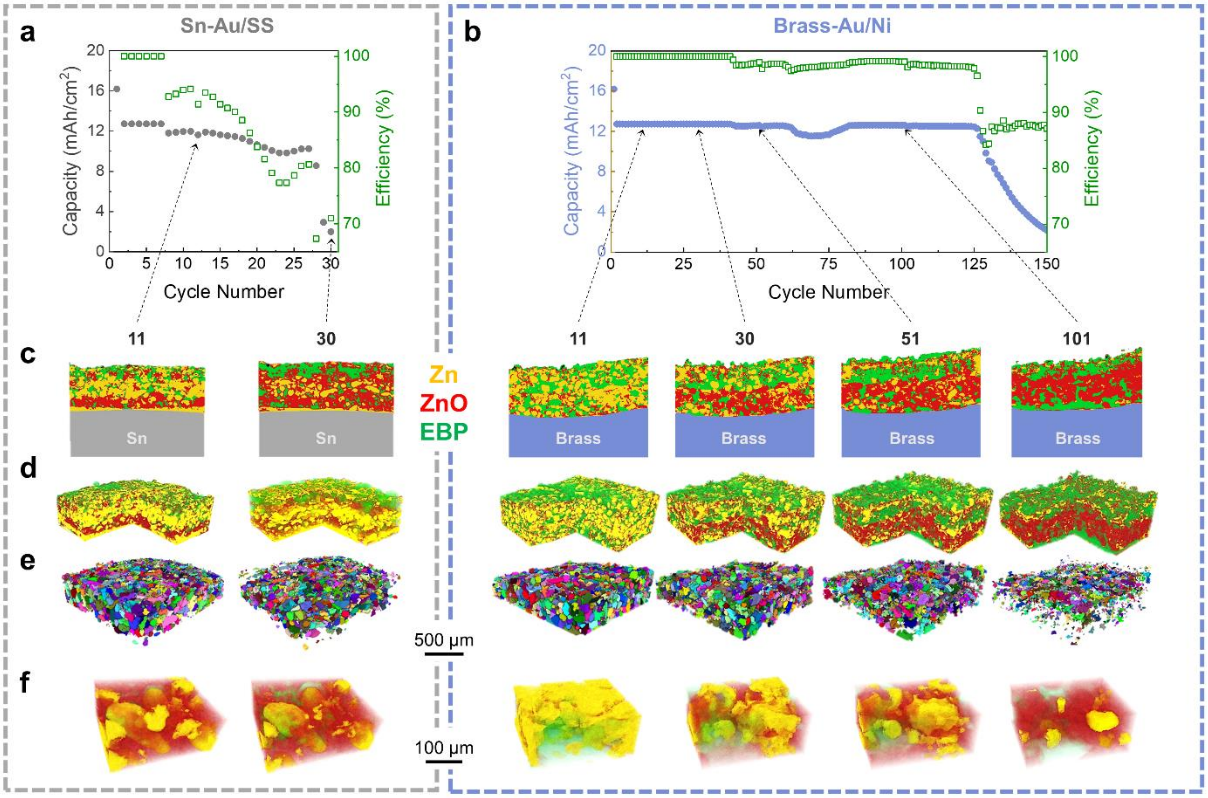

Figure 4.3 | *In-Situ* MicroCT analysis. Electrochemical cycling performance of *in-situ* MicroCT cells with (a) Sn and Au coated stainless-steel current collectors and (b) Brass and Au coated Ni current collectors. MicroCT analysis at specified cycles: (c) colorized XZ slices of Zn anode, (d) colorized corner-cut 3D reconstructed volumes of Zn anode, (e) segmented Zn particles, and (f) colorized particle scale 3D renderings. Segmentation of Zn (yellow), ZnO (red), and electrolyte-binder-pore (EBP) (green) in XZ slices and volume rendering is based on global thresholding. Zn particles in (e) are indistinctly colorized to showcase separation of individual particles.

When comparing the two current collector cases, more Zn and less ZnO is observed for the Brass-Au/Ni cell at the same cycles (*e.g.* at cycles 11 and 30). Furthermore, the EBP volume fraction stays constant after the 11th cycle, showing the increase of ZnO as the main culprit for the volume expansion and the thickness increase shown in **Figure 4.4b**. Our results show the Zn anode volume expansion to be around 100% which is in the same order than the 60-70% reported by Tobias *et al.* for an aqueous alkaline Zn-Air system.[44]

The size of the Zn particles, as depicted in **Figure 4.3e**, decreases with cycling. For the Sn-Au/SS, there is a considerable amount of Zn still left after cell failure at 30 cycles. However, for the Brass-Au/Ni cell, more of the Zn is utilized and by cycle 101, nearly all of it is converted to ZnO. This is shown in **Figure 4.4c**, where the equivalent diameter of the Zn particles shrinks as a function of cycling, and the Brass-Au/Ni cell can cycle longer to utilize more of the Zn particles. Fits for the particle size distribution for the two current collector cases can be seen in **Figure S4.10**. For the Brass-Au/Ni cell, the particles are still densely packed at cycle 11, with little ZnO, as they were when first fabricated (**Figure S4.2a,d**). The particle-scale tomograms (**Figure 4.3f**) reveal that as the cell continues to cycle, more ZnO grows around the Zn particles as the core is depleted, thus following a core-shell model as observed by Tobias *et al.*[44]

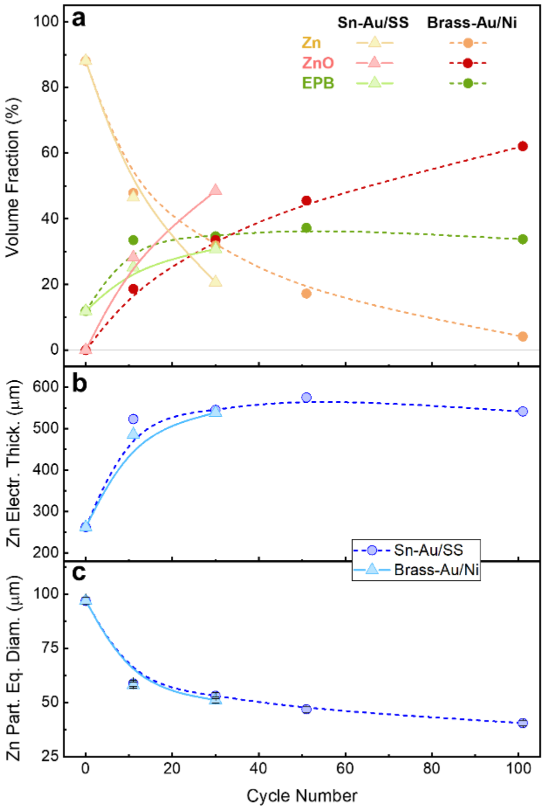

Figure 4.4 | Extracted X-ray CT Statistics. (a) Anode volume fraction of Zn (yellow), ZnO (red), and Electrolyte-Binder-Porosity EBP (green), (b) Zn anode electrode thickness, and (c) Zn particle equivalent diameter evolution during cycling. *In-situ* CT cells with Sn and Au-coated stainless-steel current collectors are represented by solid lines and triangle markers while cells while Brass and Au-coated Ni current collectors are represented by dashed lines and circle markers.

4.3.3 Effects of Current Collector on Shelf and Cycle Life

The symmetric cycling of **Figure 4.2** suggests that the cell performance is limited by effects on the cathode-side. As such, the effects of the cathode current collector on the shelf life and cycling performances were investigated for cells with Au/Ni and Au/SS current collectors. The anode current collectors were fixed to Cu, which was chosen over brass to avoid any side reaction with the electrolyte as Brass contains Zn. The shelf-life performances of the cells were evaluated by monitoring OCP with time at elevated temperatures. CT cells constructed with Au/Ni and Au/SS current collector rods were monitored for two weeks at 40ºC. As shown in **Figure 4.5a**, the Au/Ni cell exhibited less self-discharge before transitioning to the second plateau. After two weeks, CT scans were taken of the two cells and the anodes compared. The colorized XZ slices, 3D tomograms, and volume fraction percentage in **Figure 4.5b-c** reveal more ZnO (and less Zn) for the cell with the Au/SS current collector. Additionally, compared to the pristine case, the Au/SS cell exhibited larger Z-axis volume expansion than the Au/Ni cell. The increase of ZnO can be explained by Zn anode corrosion, originating from an increase of dissolved oxygen from the OER reaction of the cathode current collector.[40]

The self-discharge was also monitored for cells with a larger form factor (4 cm^2) at various temperatures in **Figure 4.5d**. At each temperature, the Au/SS cells fail quicker than the Au/Ni cells. The rapid drop in voltage shown for the Au/SS cell at 55ºC is likely caused by electrolyte depletion due to increased gassing at higher temperatures. However, due to less gassing, the Au/Ni cell at 55ºC demonstrated self-discharge with the expected two-phase transition. The DCIR resistance was also monitored during the OCP measurement in **Figure S4.6a**. The Au/SS cells quickly exhibited large increases in resistances whereas the Au/Ni cells increased slowly or were stable with time. The self-discharge rate for the Au/Ni cell at room temperature was quantified by discharging cells after controlled idle times to measure the percent of capacity loss with time. A discharge was performed every week over 4 weeks, and the results in **Figure S4.6c-d** reveal an average discharge rate of 7.06 %/wk, a considerable improvement with respect to previously reported lifetimes. [39,59]

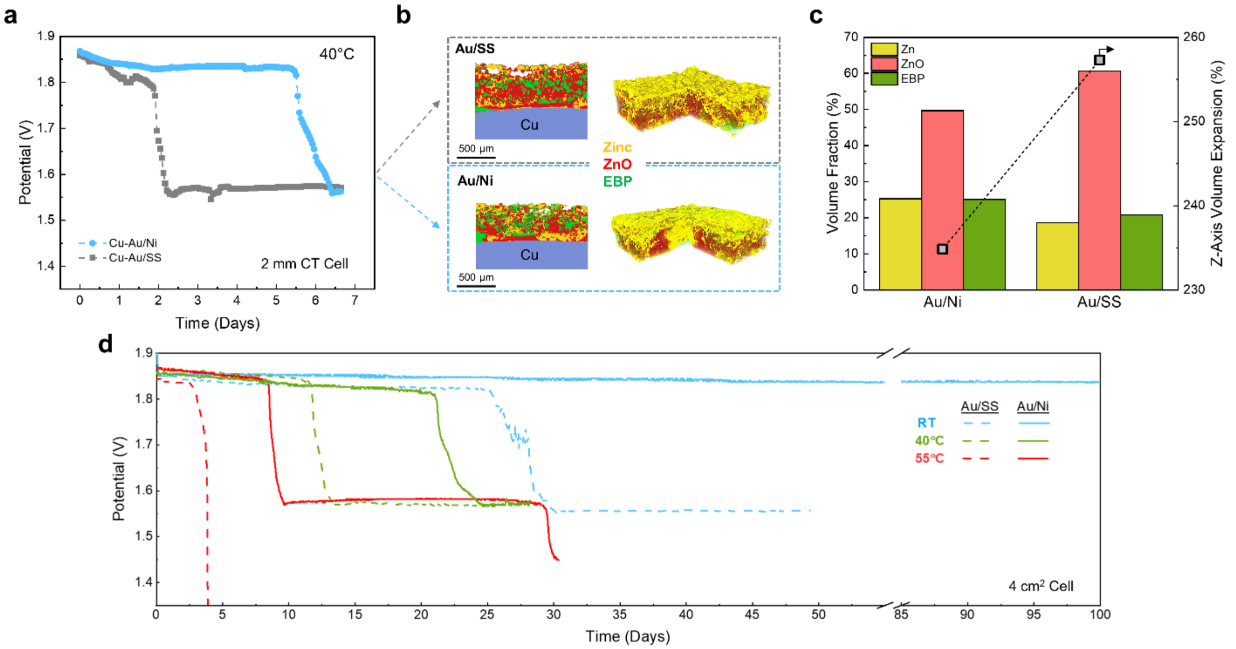

Figure 4.5 | Shelf life and effect of current Collector. (a) Open-circuit voltage at 40ºC of 2 mm diameter *in-Situ* CT cell with Au coated Ni (blue) and Au coated stainless-steel (grey) cathode current collectors. (b) XZ CT slice and colorized corner-cut reconstructed volume and (c) volume fraction (*left*) of Zn (yellow), ZnO (red), and EBP (green) and z-axis volume expansion (*right*) of Zn anode after 1 week at 40ºC. (d) Open-circuit voltage of larger 4 cm^2 cells at room temperature, 40ºC, and 55ºC for different cathode current collectors.

The cycling performance of the Au/Ni cells were also evaluated. **Figure 4.6** compares the cycling at 12.5 mAh/cm^2 of a 4 cm^2 cell with the cells fabricated for CT. With the less corrosive cathode current collector, the CT cells demonstrated >250 cycles above 80% capacity retention. The slight dip in coulombic efficiency at around 50 cycles is due to the transition between the capacity-limited regime and the voltage limited regime. The 4 cm^2 form factor in **Figure 4.6b** illustrate similar performances, >150 cycles at the same rate of C/5 (~2.5 mA/cm^2) and >250 cycles at C/3 (~4.2 mA/cm^2). The low impedance of the 4 cm^2 (**Figure S4.6b**) allows for higher rate cycling, which is also revealed in the capacity-voltage plot in **Figure S4.11f** by the small IR drop when cycling at 4.2 mA/cm^2. Overall, the cell demonstrated a cycling volumetric energy density of 104.7 Wh/L and power density of 34.6 W/cm^3.

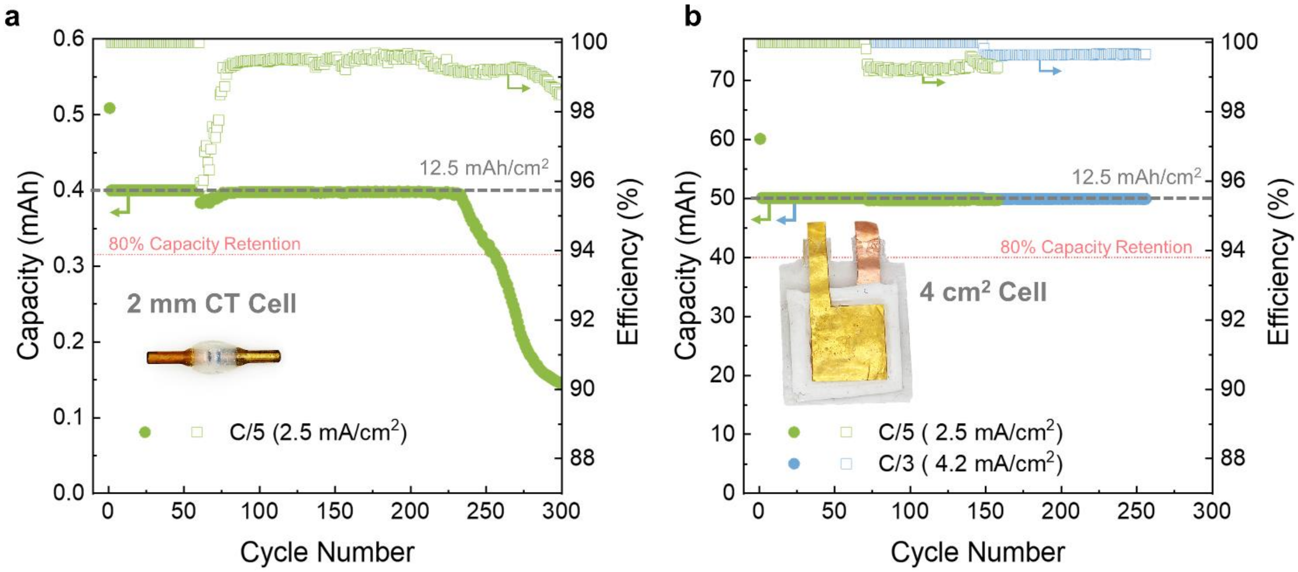

Figure 4.6 | Cycle life performance. Electrochemical cycle life of (a) 2 mm diameter *In-situ* Au/Ni-Brass CT cell and (b) larger 4 cm^2 Au/Ni-Cu Cell.

4.4 Conclusion

In this work, we used *in-situ* X-ray MicroCT in combination with electrochemical experiments to investigate the effects of current collector corrosion on the performances of Zn-AgO batteries. The results reveal the dependency of current collector materials in limiting OER and HER reactions that degrade cell performances. With *in-situ* MicroCT, we quantified the Z-axis volume expansion and showed Zn particle depletion with cycling that follows a shrinking core model. From an improved selection of electrochemically compatible current collectors, we demonstrated superior performances with a high cycling capacity of 12.5 mAh/cm^2 for more than 250 cycles in a 4 cm^2 form factor. This resulted in a cycling volumetric energy density of 104.7 Wh/L and power density of 34.6 W/cm^3. We have demonstrated extended cycle and shelf life enabled by the mitigation of the current collector gassing and have successfully prolonged the lifetimes of Zn/AgO batteries.

However, while we demonstrated a self-discharge rate of 7.06 %/wk, further efforts need to be done to extend cell shelf life beyond that. The investigation on the Zn symmetric cells and shelf-life tests showed that the OERs at the cathode current collector are one of the limiting factors. As a result, current collector treatments and coatings need to be developed to limit the OER and improve performances. Additives in the electrodes and the electrolyte also need be explored to limit parasitic reactions, and further investigations of electrochemically compatible hydrogels could limit silver dissolution known to degrade Zn-Ag battery performances.

Lastly, through the development of representative *in-situ* CT cells, we report the first *in-situ* CT study of Zn-Ag batteries and utilize CT to study the degradation with long-term cycling (>250 cycles at 12.5 mAh/cm^2). The results from this work exemplify the utility and advantages of *in-situ* CT experimentation in elucidating degradation effects in battery systems. Following this work, we expect long-term *in-situ* CT to be increasingly used in academic and industry battery research to better improve device performances and aid in the effort to combat the energy crisis.

4.5 Acknowledgements

This work was supported by funding from ZPower LLC, United States and Qualcomm, United States. For use of the MicroCT system, the authors would like to acknowledge the National Center for Microscopy and Imaging Research (NCMIR) technologies and instrumentation are supported by grant R24GM137200 from the National Institute of General Medical Sciences. This work was performed in part at the San Diego Nanotechnology Infrastructure (SDNI) of UCSD, NANO3, a member of the National Nanotechnology Coordinated Infrastructure, which is supported by the National Science Foundation (Grant ECCS-1542148). The authors would also like to acknowledge Neware Technology Limited for the donation of CT4000 battery cyclers, which are used to obtain the cycling data of cells in this paper.

4.6 Supplementary Information

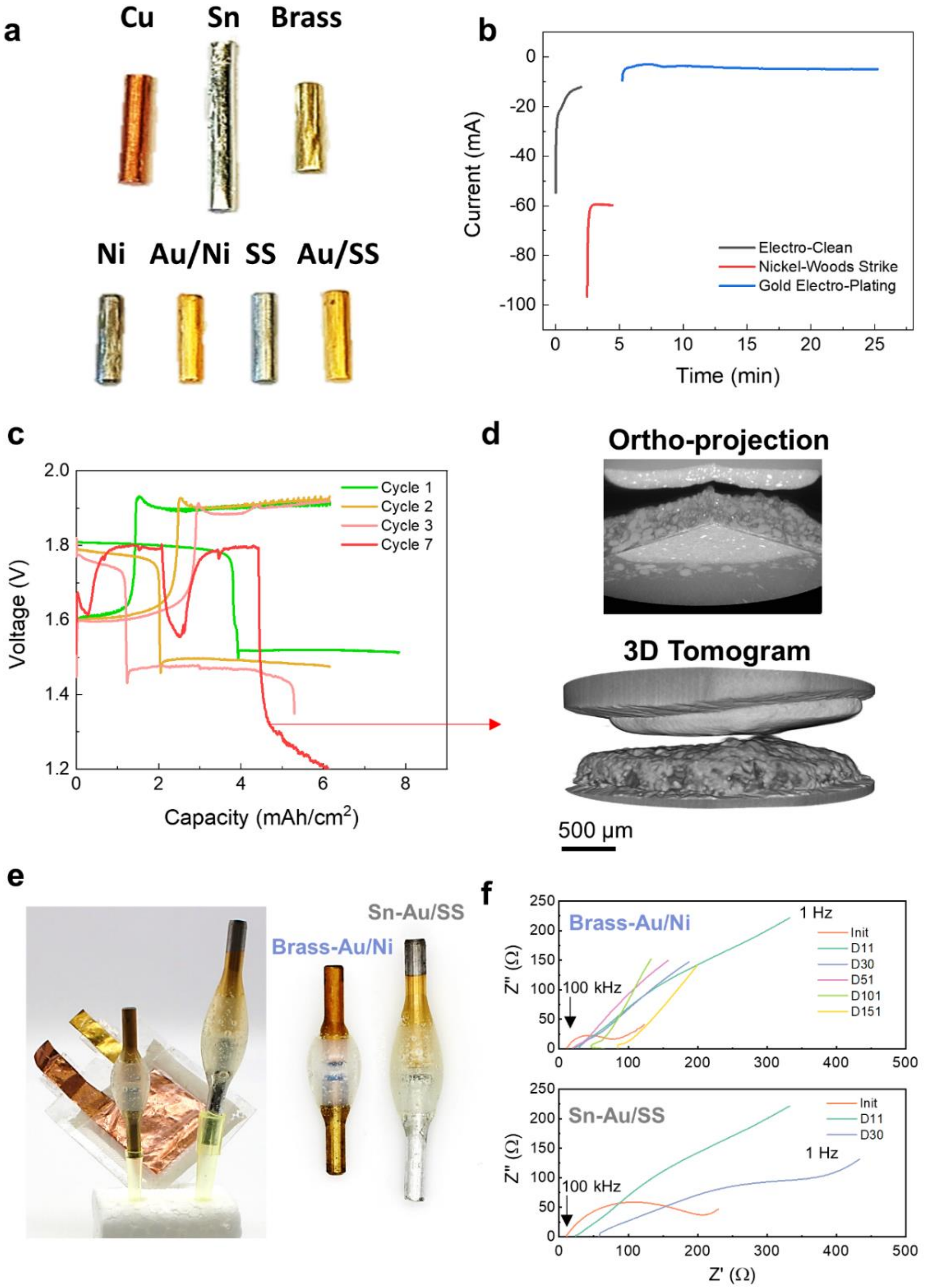

Figure S4.1 | In-situ CT cell information and construction. (a) Picture of current collector rods used in CT cell construction. (b) Current-time plot of electroplating processes of Au coating of stainless-steel rods. (c) Voltage profile of shorted CT cell of an unoptimized in-situ architecture. (d) CT visualization of dendrite short as ortho-projection (top) and 3D tomogram (bottom). (e) Pictures of Brass-Au/Ni (left) and Sn-Au/SS (right) CT cells and size comparison to a 4 cm^2 cell. (f) EIS of in-situ CT cells of **Figure 4.3** at the same cycles where MicroCT characterization was performed.

CT cells of the pristine anode films of **Figure S4.2** were prepared by placing the punched 2 mm diameter films within a 3 mm diameter PTFE tube and PTFE rods at both ends securing the sample. The samples were then sealed end to end in epoxy to create a similar X-ray attenuation environment seen by the *in-situ* cells.

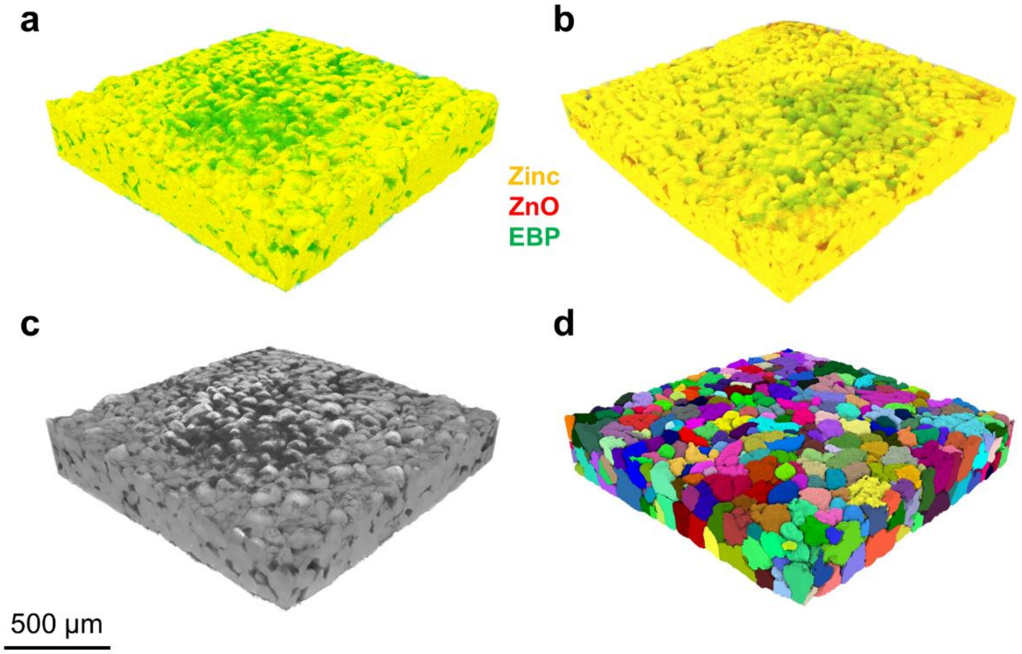

Figure S4.2 | X-Ray MicroCT of pristine anode films. (Top) Colorized X-Ray MicroCT reconstructed tomograms for pristine anode film used in (a) in-situ CT cells of **Figure 4.3** and (b) OCP CT cells used in **Figure 4.5**. The colors represent the different species: yellow (Zn), red (ZnO), green (EPB). (Bottom) Greyscale scale tomogram (a) and Zn particle distribution (d) of pristine anode (a). Zn particles in (d) are indistinctly colorized to showcase the separation of individual particles.

Powder reference CT cells were fabricated to evaluate the gray-value regions pertaining to the Zn and ZnO species. Zn (ZPower) and ZnO (Grillow) powders were packed inside in a 3 mm diameter PTFE tube with 25μm thick PTFE films separating the powder regions. As shown in **Figure S4.3a**, the reference consisted of three distinct powder regions: (top) ZnO powder only, (middle) Zn mixed with ZnO, (bottom) ZnO powder only. The resultant grays value distribution in **Figure S4.3b** reveals the grey-value regions for the two species, 0.07 to 0.11 for ZnO and 0.11 to 0.2 for Zn.

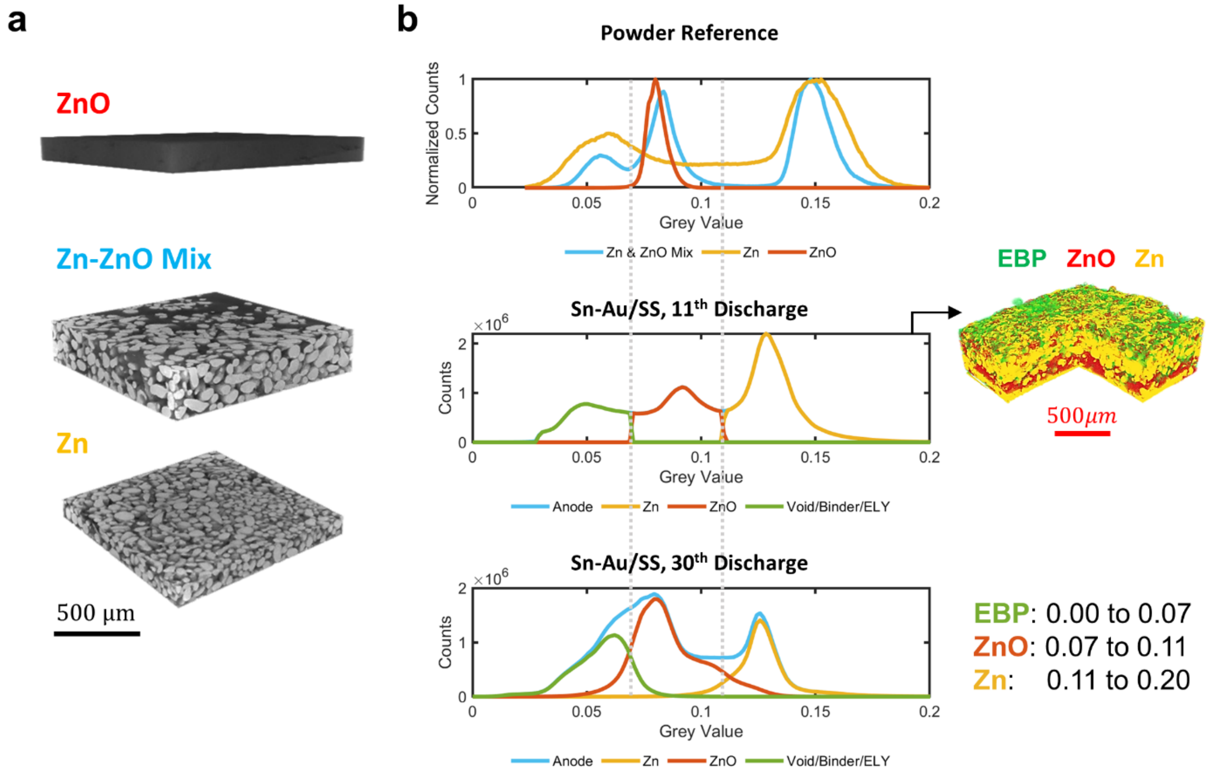

Figure S4.3 | X-Ray MicroCT powder reference samples for species segmentation. (a) Greyscale tomogram of powder reference for ZnO (top), Zn mixed with ZnO (middle) and Zn (bottom) powders. (b) Greyscale distribution of powder reference (Top), Sn-Au/SS in-situ CT cell at 11th discharge (middle), and 30th discharge (bottom). Grey lines indicate regions of global thresholding for species segmentation with specified values and example tomogram shown (right).

The Zn symmetric cells tested in **Figure 4.2** were constructed with 3 mm or 4 mm diameter PTFE tubing and brass or Sn metal rod current collectors. The Zn anode films were initially discharged before assembly to half of the desired cycling Zn Depth-of-Discharge (DoD_{Zn}) using a three electrode setup with a 10 M KOH, 0.6M LiOH aqueous electrolyte, a Hg/HgO reference electrode, and a platinum foil counter electrode (**Figure S4.4a**). A constant current (chronopotentiometry) was applied at 2.5 mA/cm^2 to discharge the anode films in the aqueous electrolyte. The films were then rinsed with DI water and dried before punching 2 mm diameter films to be assembled in cells. The cell architecture in **Figures S4.4c** shows anode films in contact with the rod current collectors and PVA hydrogel electrolytes with an FAS separator in between the gels to hinder dendrite growth. Similar to the CT and larger form factor cells, a 60% weight ratio of hydrogel-active material was used for proper wetting. The symmetric cells were initially discharged to half the desired DoD_{Zn} to allow one end to charge to 0% DoD_{Zn}, and were then cycled at the full desired DoD_{Zn} at 2.5 mA/cm^2 to match the cycling conditions of the CT full cells. A discharge cutoff of -0.2 V and a constant voltage limit of 0.2V was used for the cycling of symmetric cells.

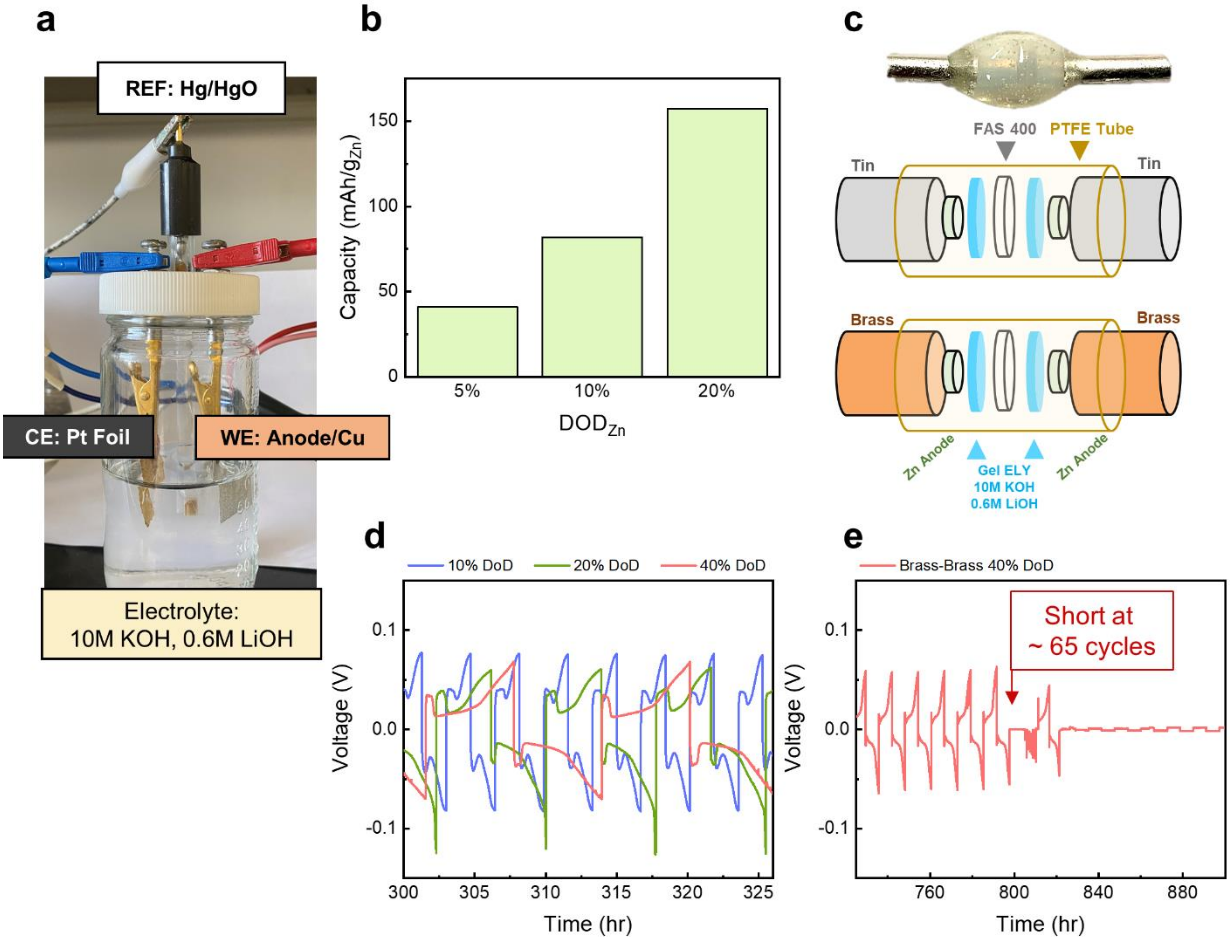

Figure S4.4 | Zinc symmetric cell fabrication and cycling. (a) Picture of 3 electrode electrochemical setup. (b) Initial discharge capacity bar graph of anode films before assembly. (c) Diagram of symmetric cell architectures for Sn-Sn and Brass-Brass cycling performance indicated in **Figure 4.2c-d**. (d) Voltage vs. time example of Brass-Brass cell at different DoD$_{Zn}$. (e) Example of short in Zn symmetrical cell for 40% DoD$_{Zn}$ Brass-Brass cell.

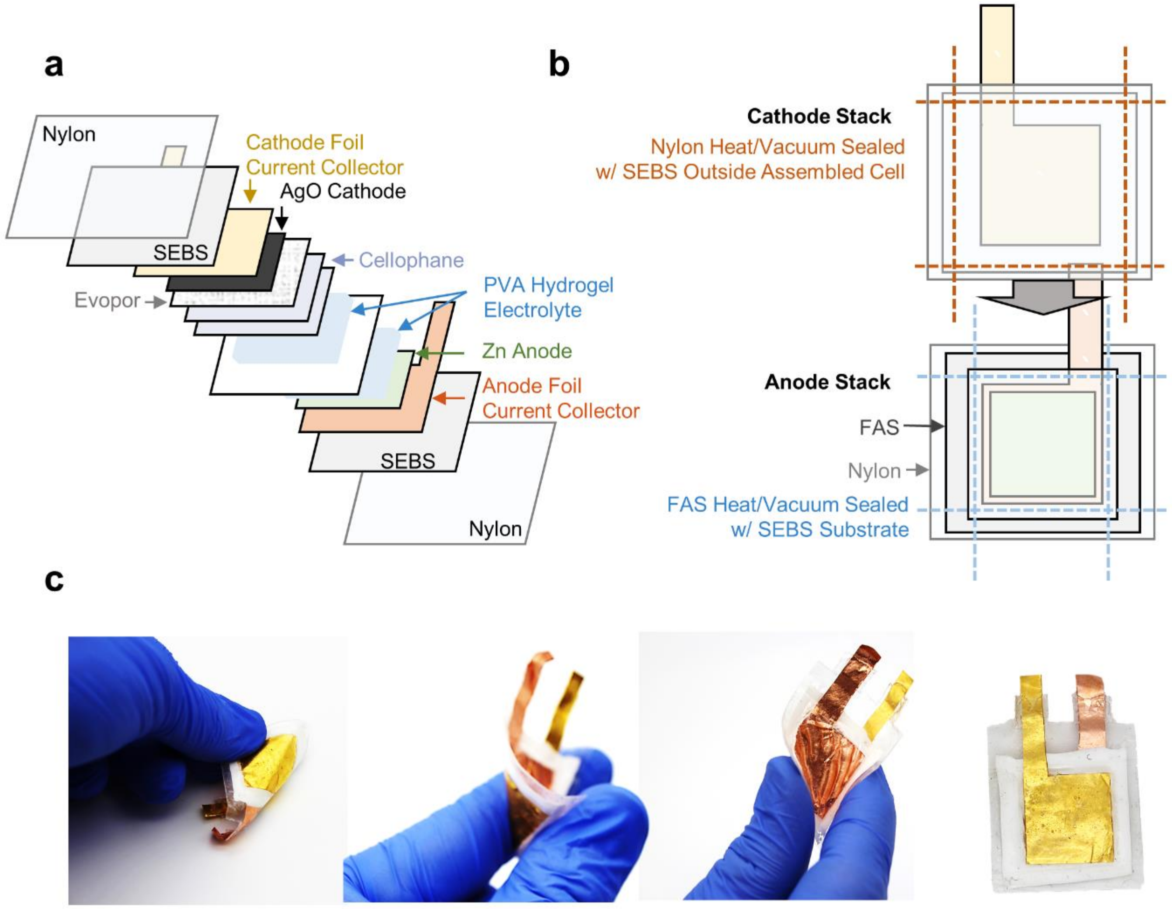

Figure S4.5 | Fabrication of 4 cm^2 form factor Zn-AgO cells. (a) Stack architecture. (b) Diagram of half-cell assembly and sealing. Dotted lines indicate regions of vacuum and heat-sealing SEBS (blue) and Nylon (Orange). (c) Pictures of assembled 4 cm^2 Zn-AgO cell.

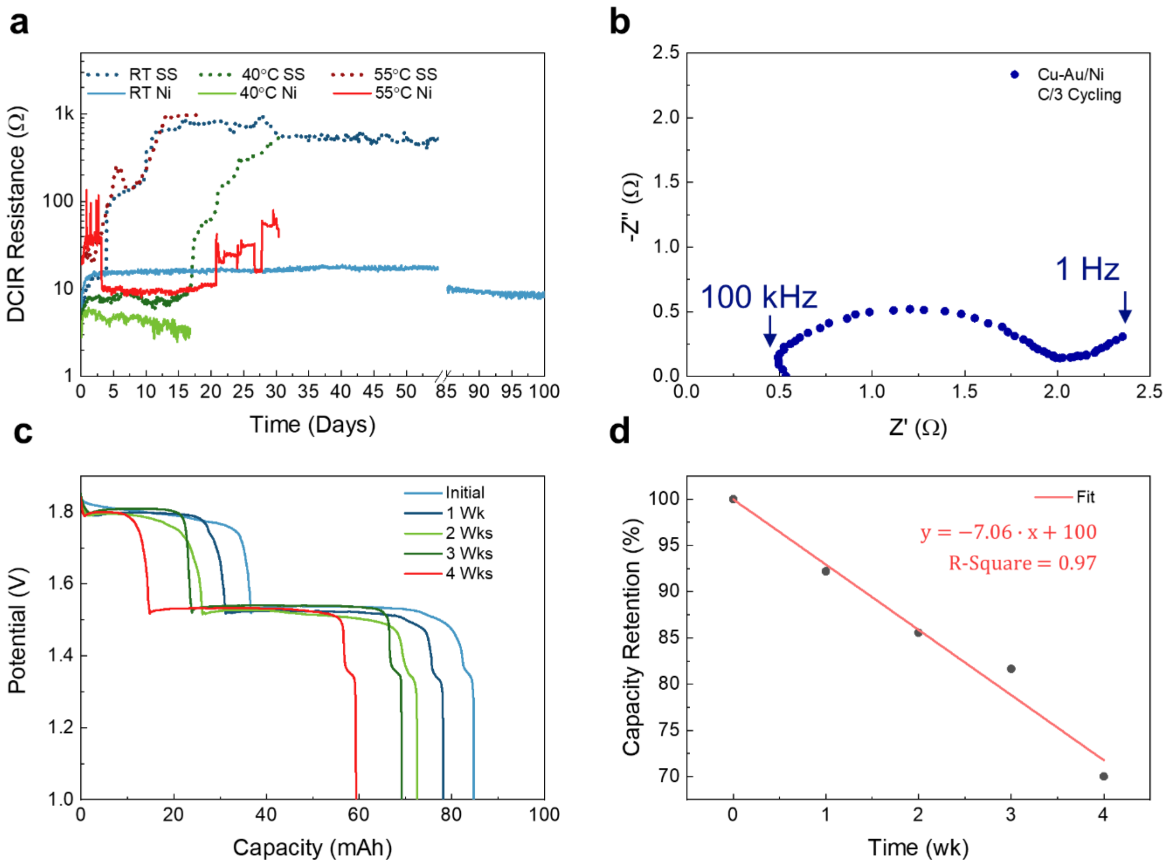

Figure S4.6 | Impedance and self-discharge performance of 4 cm^2 Zn-AgO batteries. (a) DCIR resistances as a function of idling at set temperatures. (b) EIS impedance of Cu-Au/Ni cell in **Figure 4.6** (b) cycled at C/3. (c) Discharge profiles of assembled Cu-Au/Ni cells after idling for different weeks at room temperature. (d) Capacity retention vs. idle time for Cu-Au/Ni cells with linear fit.

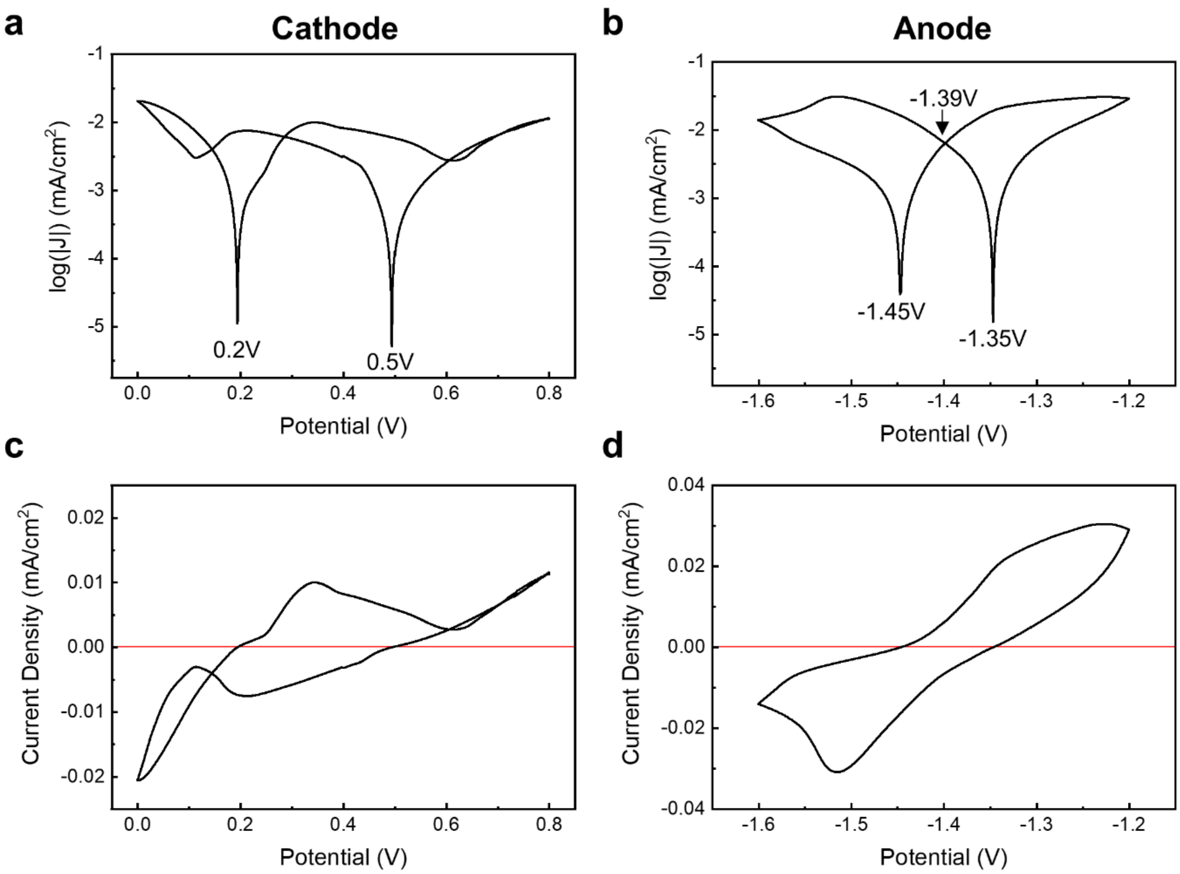

Figure S4.7 | Determination of electrochemical reaction potentials of cathode and anode. Tafel and corresponding cyclic voltammetry (CV) plots of AgO cathode (a, c) and Zn anode (b, d). Red lines in CV indicate oxidation and reduction transition at a current density of 0 where reaction onset occur.

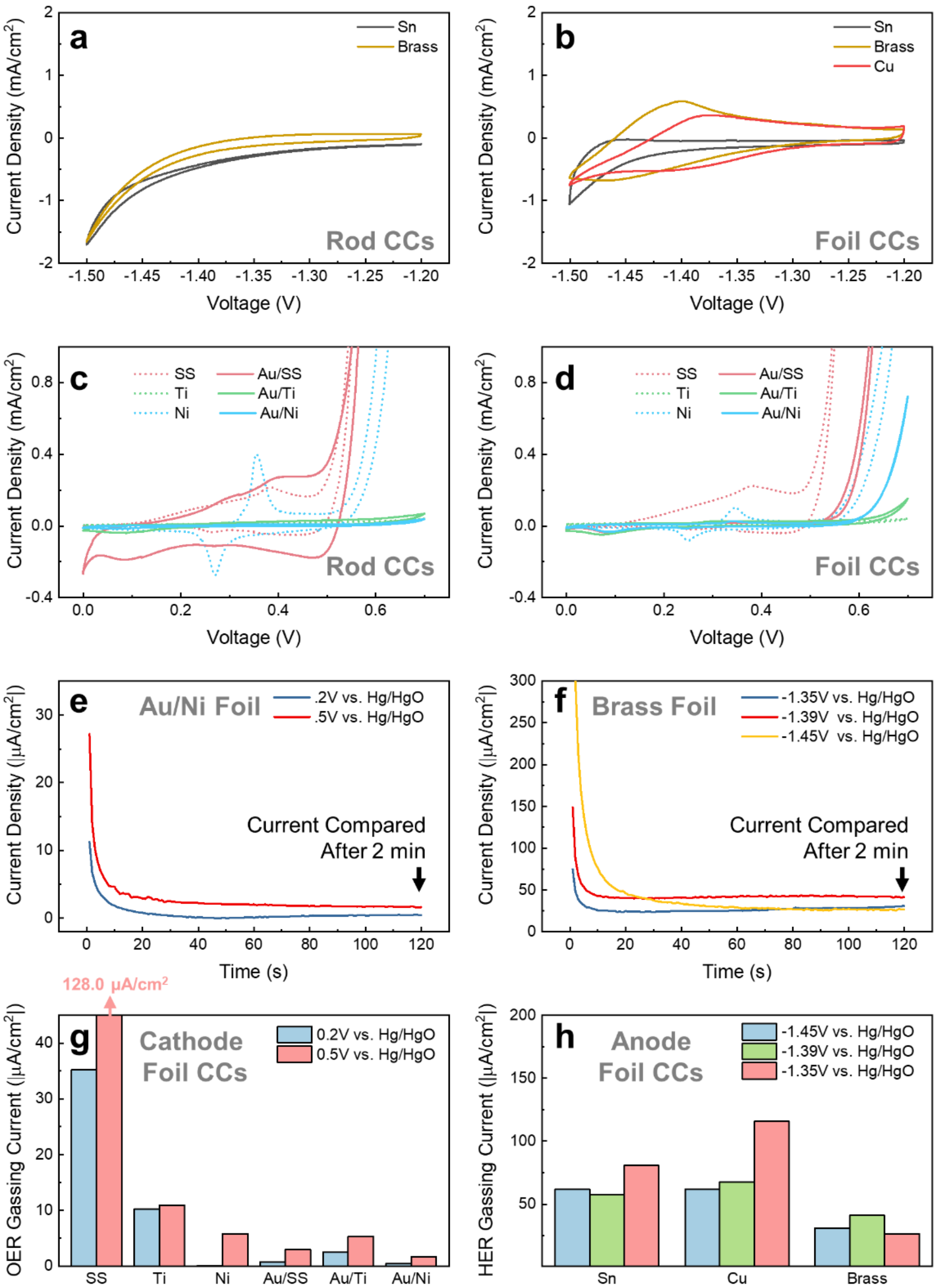

Figure S4.8 | Cyclic voltammetry and chronoamperometry of current collectors. Cyclic voltammetry (CV) of anode current collectors for rods (a) and foils (b) and cathode current collectors for rods (c) and foils (d). CV plots (a-d) show the 5th sweep cycle. Example chronoamperometry of Au/Ni foil (e) and brass foil (f). Arrow indicates time in which current density analyzed for bar graphs in **Figure S4.g-h** and **Figure 4.2a-b**. Bar graphs of current density magnitude after 2 min of chronoamperometry of metal foils shown for cathode current collectors (g) and anode current collectors (h).

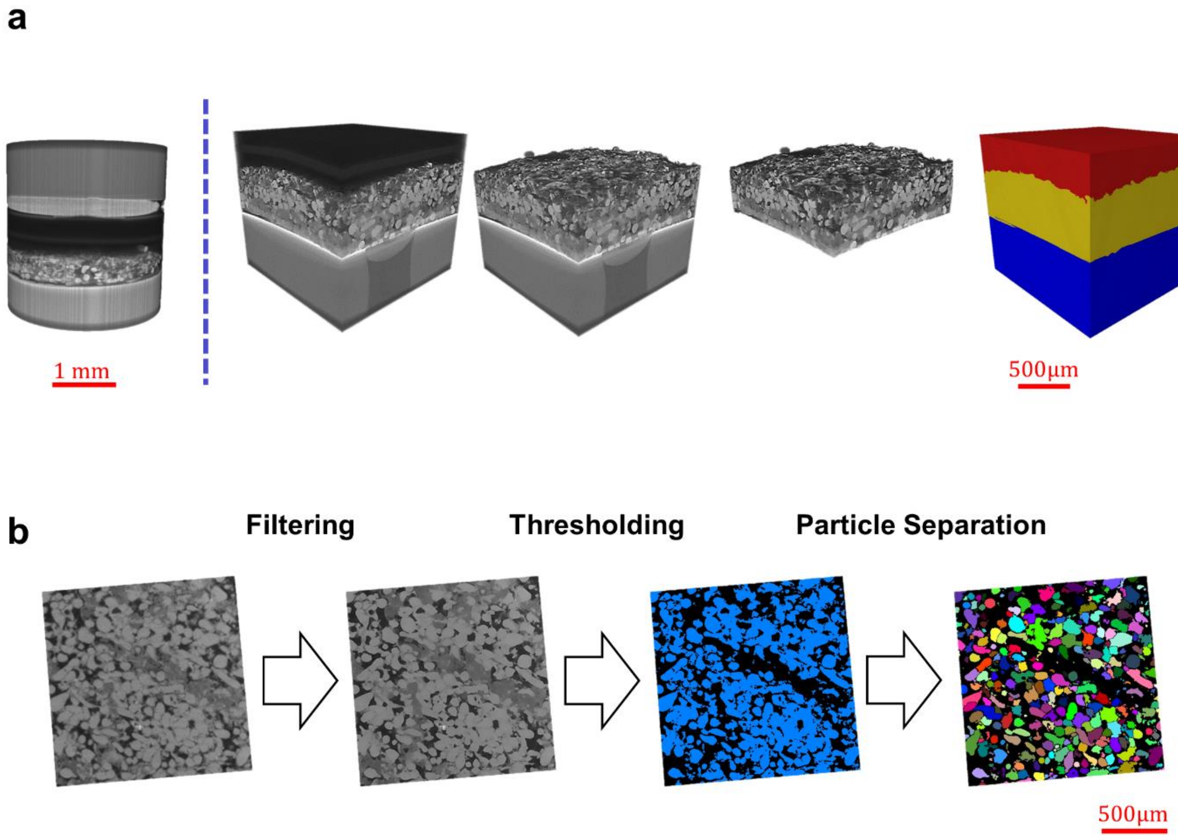

Figure S4.9 | MicroCT segmentation and analysis procedure. (a) Cropping and segmentation workflow to analyze anode region. (b) Filtering and Zn particle segmentation workflow.

Relevant Supplementary Video

Video S4.1 | MicroCT Anode and Species Segmentation of Sn-Au/SS in-situ CT cell

The equivalent zinc particles sizes presented in **Figure 4.4c** were obtained by fitting the particle distributions for the *in-situ* CT anodes shown in **Figure S4.11**. Before cycling, the pristine anodes contain mostly larger particles with an equivalent diameter between 50 µm to 100 µm. As the cycling progresses, the amount of smaller Zn particles (<20 µm) increases and the distribution of larger particles shift to lesser values. The "Label Analysis" module was then used to calculate the equivalent diameter in Equation 1. The distribution of the particle diameter was then fitted using a lognormal distribution with MATLAB as shown in **Figure S4.10** and the extracted mean and standard deviation used in **Figure 4.4c**.

$$EqDiameter = \sqrt[3]{6 \times \frac{Volume}{\pi}} \tag{1}$$

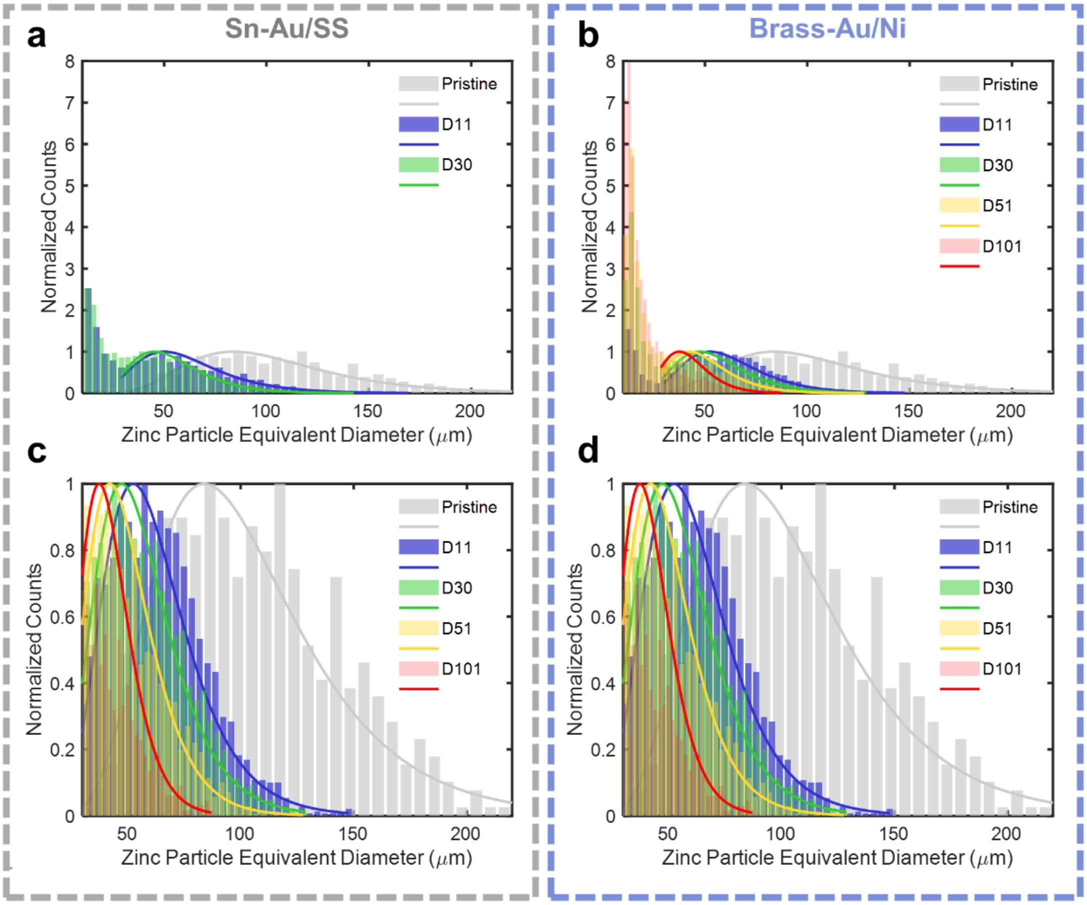

Figure S4.10 | Anode zinc particle size distribution and fitting. Zinc particle distribution and fits for in-situ CT anode at various cycles for Sn-Au/SS (a, c) and Brass-Au/Ni (b, d) cells. Close up plots (b, d) showcase fitted regions with lognormal fits indicated by solid lines. The count values in all plots are normalized to the peak value of the fit.

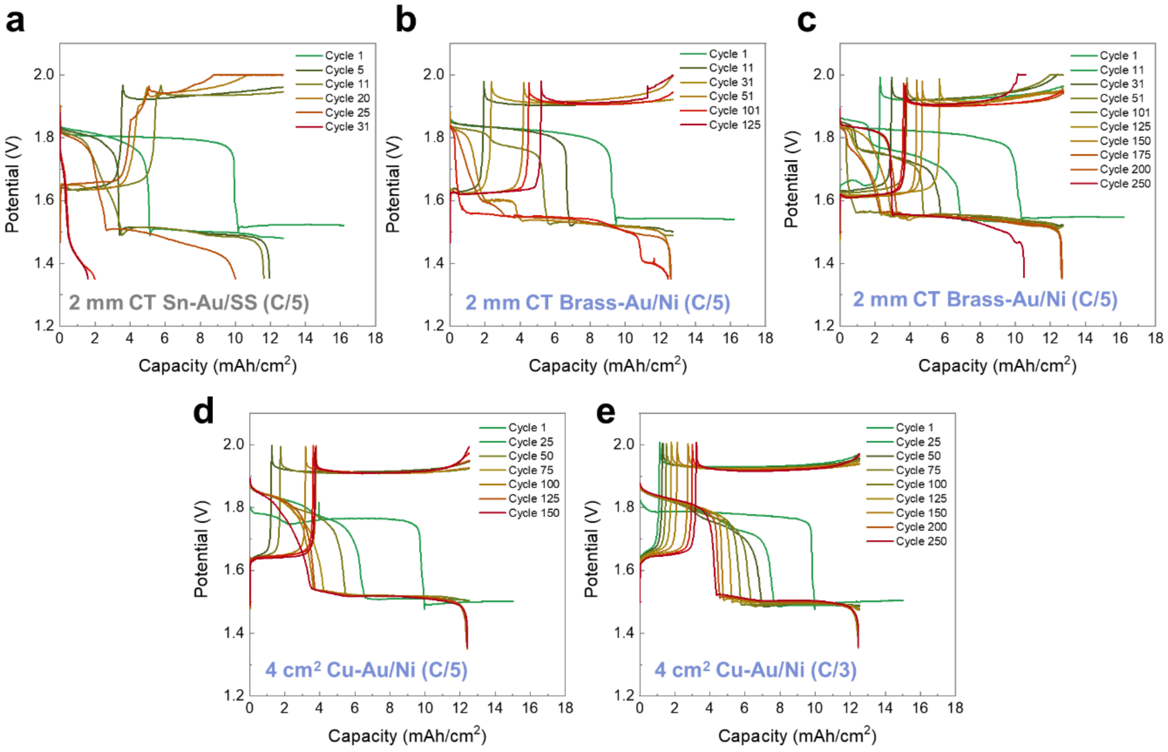

Figure S4.11 | Voltage-capacity profiles of Zn-AgO batteries. (a-c) CT cell voltage-capacity profile of Sn-Au/SS cell (a) and Brass-Au/Ni cell (b) used in-situ study of **Figure 4.3**, and Brass-Au/Ni cell (c) shown in **Figure 4.6a**. (d-e) Voltage-capacity profiles of 4 cm^2 battery cycling of **Figure 4.6b** at C/5 (d) and C/3 (e) rates.

4.7 References

1. Jiang, P., Fan, Y. V. & Klemeš, J. J. Impacts of COVID-19 on energy demand and consumption: Challenges, lessons and emerging opportunities. Applied Energy 285, 116441 (2021).

2. Ahmad, T. & Zhang, D. A critical review of comparative global historical energy consumption and future demand: The story told so far. Energy Reports 6, 1973–1991 (2020).

3. Foley, A. & Olabi, A. G. Renewable energy technology developments, trends and policy implications that can underpin the drive for global climate change. Renewable and Sustainable Energy Reviews 68, 1112–1114 (2017).

4. Talens Peiró, L., Villalba Méndez, G. & Ayres, R. U. Lithium: Sources, Production, Uses, and Recovery Outlook. JOM 65, 986–996 (2013).

5. Eftekhari, A. Lithium Batteries for Electric Vehicles: From Economy to Research Strategy. ACS Sustainable Chem. Eng. 7, 5602–5613 (2019).

6. Calls for lithium battery review after Boeing Dreamliner fire at Heathrow | Boeing | The Guardian. https://www.theguardian.com/business/2015/aug/19/lithium-battery-review-boeing-dreamliner-fire-heathrow.

7. UN bans lithium batteries as cargo on passenger planes. BBC News (2016).

8. Samsung to Recall Galaxy Note 7 Smartphone Over Reports of Fires - WSJ. https://www.wsj.com/articles/samsung-to-recall-galaxy-note-7-smartphone-1472805076.

9. Choi, J. W. & Aurbach, D. Promise and reality of post-lithium-ion batteries with high energy densities. Nat Rev Mater 1, 16013 (2016).

10. Yadav, G. G., Turney, D., Huang, J., Wei, X. & Banerjee, S. Breaking the 2 V Barrier in Aqueous Zinc Chemistry: Creating 2.45 and 2.8 V MnO 2 –Zn Aqueous Batteries. ACS Energy Lett. 4, 2144–2146 (2019).

11. Pan, H. et al. Reversible aqueous zinc/manganese oxide energy storage from conversion reactions. Nat Energy 1, 16039 (2016).

12. Fang, G., Zhou, J., Pan, A. & Liang, S. Recent Advances in Aqueous Zinc-Ion Batteries. ACS Energy Letters 3, 2480–2501 (2018).

13. R. Mainar, A. et al. Alkaline aqueous electrolytes for secondary zinc-air batteries: an overview: Challenges of aqueous alkaline electrolytes for zinc air batteries. Int. J. Energy Res. 40, 1032–1049 (2016).

14. Li, Y. & Dai, H. Recent advances in Zinc-air batteries. Chemical Society Reviews 43, 5257–5275 (2014).

15. Lee, J.-S. et al. Metal–Air Batteries with High Energy Density: Li–Air versus Zn–Air. Advanced Energy Materials 1, 34–50 (2011).

16. Parker, J. F. et al. Rechargeable nickel–3D zinc batteries: An energy-dense, safer alternative to lithium-ion. 418, 415–418 (2017).

17. Yin, L. et al. High Performance Printed AgO-Zn Rechargeable Battery for Flexible Electronics. Joule 5, 228–248 (2021).

18. Turney, D. E. et al. Rechargeable Zinc Alkaline Anodes for Long-Cycle Energy Storage. (2017) doi:10.1021/acs.chemmater.7b00754.

19. Leal, C. et al. Untethered Disposable Health Monitoring Electronic Patches with an Integrated Ag 2 O–Zn Battery, a AgInGa Current Collector, and Hydrogel Electrodes. ACS Appl. Mater. Interfaces 12, 3407–3414 (2020).

20. Li, Y. et al. Recent Advances in Flexible Zinc-Based Rechargeable Batteries. Advanced Energy Materials 1802605, 1802605 (2018).

21. Song, W., Yoo, S., Song, G., Lee, S. & Kong, M. Recent Progress in Stretchable Batteries for Wearable Electronics. 181–199 (2019) doi:10.1002/batt.201800140.

22. Fu, J. et al. Electrically Rechargeable Zinc–Air Batteries: Progress, Challenges, and Perspectives. Advanced Materials 29, (2017).

23. Lyu, L. et al. Improving the cycling performance of silver-zinc battery by introducing PEG-200 as electrolyte additive. Chemical Physics Letters 723, 102–110 (2019).

24. Ma, M. et al. Electrochemical performance of ZnO nanoplates as anode materials for Ni/Zn secondary batteries. Journal of Power Sources 179, 395–400 (2008).

25. Bass, K., Mitchell, P. J., Wilcox, G. D. & Smith, J. Methods for the reduction of shape change and dendritic growth in zinc-based secondary cells. Journal of Power Sources 35, 333–351 (1991).

26. Wang, S. J. et al. Deposition of ZnO on bismuth species towards a rechargeable Zn-based aqueous battery. doi:10.1039/c6cp04566a.

27. Yadav, G. G., Jungsang, C., Wei, X., Nyce, M. & Banerjee, S. Zinc electrodes with high capacity utilizations. (Google Patents, 2020).

28. Wei, X., Nyce, M., Yadav, G. G., Couzis, A. & Banerjee, S. Additive for increasing lifespan of rechargeable zinc-anode batteries. (Google Patents, 2021).

29. Mitha, A., Yazdi, A. Z., Ahmed, M. & Chen, P. Surface Adsorption of Polyethylene Glycol to Suppress Dendrite Formation on Zinc Anodes in Rechargeable Aqueous Batteries. ChemElectroChem 5, 2409–2418 (2018).

30. Parker, J. F. et al. Retaining the 3D Framework of Zinc Sponge Anodes upon Deep Discharge in Zn–Air Cells. ACS Appl. Mater. Interfaces 6, 19471–19476 (2014).

31. Parker, J. F., Chervin, C. N., Nelson, E. S., Rolison, D. R. & Long, J. W. Wiring zinc in three dimensions re-writes battery performance—dendrite-free cycling. Energy Environ. Sci. 7, 1117–1124 (2014).

32. Dirkse, T. P. & Timmer, R. The Corrosion of Zinc in KOH Solutions. J. Electrochem. Soc. 116, 162 (1969).

33. Lee, T. S. Hydrogen Over potential on Pure Metals in Alkaline Solution. J. Electrochem. Soc. 118, 1278 (1971).

34. Liu, J., Xu, C., Chen, Z., Ni, S. & Shen, Z. X. Progress in aqueous rechargeable batteries. Green Energy & Environment 3, 20–41 (2018).

35. Allen, J. P., Scanlon, D. O. & Watson, G. W. Electronic structures of silver oxides. Phys. Rev. B 84, 115141 (2011).

36. Wales, C. P. & Burbank, J. Oxides on the Silver Electrode. JOURNAL OF THE ELECTROCHEMICAL SOCIETY 106, 6 (1959).

37. McMillan, J. Higher Oxidation States of Silver. Chemical Reviews 62, 65–80 (1962).

38. Amlie, R. F. & Rüetschi, P. Solubility and Stability of Silver Oxides in Alkaline Electrolytes. J. Electrochem. Soc. 108, 813 (1961).

39. Kumar, R., Johnson, K. M., Williams, N. X. & Subramanian, V. Scaling Printable Zn–Ag 2 O Batteries for Integrated Electronics. Adv. Energy Mater. 9, 1803645 (2019).

40. Su, L., Liu, L., Liu, B., Meng, J. & Yan, X. Revealing the impact of oxygen dissolved in electrolytes on aqueous zinc-ion batteries. Iscience 23, 100995 (2020).

41. Wei, X. et al. Impact of anode substrates on electrodeposited zinc over cycling in zinc-anode rechargeable alkaline batteries. Electrochimica Acta 212, 603–613 (2016).

42. Bonnick, P. & Dahn, J. R. A Simple Coin Cell Design for Testing Rechargeable Zinc-Air or Alkaline Battery Systems. J. Electrochem. Soc. 159, A981–A989 (2012).

43. Franke-lang, R., Arlt, T., Manke, I. & Kowal, J. X-ray tomography as a powerful method for zinc-air battery research. Journal of Power Sources 370, 45–51 (2017).

44. Arlt, T., Schröder, D., Krewer, U. & Manke, I. In operando monitoring of the state of charge and species distribution in zinc air batteries using X-ray tomography and model-based simulations. Phys. Chem. Chem. Phys. 16, 22273–22280 (2014).

45. Ko, J. S. et al. Robust 3D Zn Sponges Enable High-Power, Energy-Dense Alkaline Batteries. ACS Appl. Energy Mater. 2, 212–216 (2019).

46. Yermukhambetova, A. et al. Exploring 3D microstructural evolution in Li-Sulfur battery electrodes using in-situ X-ray tomography. Sci Rep 6, 35291 (2016).

47. Christensen, M. K., Mathiesen, J. K., Simonsen, S. B. & Norby, P. Transformation and migration in secondary zinc–air batteries studied by in situ synchrotron X-ray diffraction and X-ray tomography. J. Mater. Chem. A 7, 6459–6466 (2019).

48. Taiwo, O. O. et al. Investigating the evolving microstructure of lithium metal electrodes in 3D using X-ray computed tomography. Phys. Chem. Chem. Phys. 19, 22111–22120 (2017).

49. 24K Pure Gold Plating Solution - Bath. Gold Plating Services https://www.goldplating.com/products/24k-pure-gold-solution.

50. Arora, P. & Zhang, Z. (John). Battery Separators. Chem. Rev. 104, 4419–4462 (2004).

51. Tsehaye, M. T. et al. Membranes for zinc-air batteries: Recent progress, challenges and perspectives. Journal of Power Sources 475, 228689 (2020).

52. Innovia Films - BOPP Film for Food and Tobacco Packaging and Labels. http://www.innoviafilms.com/.

53. Viola, P. Alignment by Maximization of Mutual Information. 18 (1997).

54. Collignon, A. et al. Automated multi-modality image registration based on information theory. In: Bizais (1995).

55. Pluim, J., Maintz, J. & Viergever, M. Mutual-Information-Based Registration of Medical Images: A Survey. Medical Imaging, IEEE Transactions on 22, 986–1004 (2003).

56. Roche, A., Malandain, G., Pennec, X. & Ayache, N. The correlation ratio as a new similarity measure for multimodal image registration. in Medical Image Computing and Computer-Assisted Intervention — MICCAI'98 (eds. Wells, W. M., Colchester, A. & Delp, S.) 1115–1124 (Springer, 1998). doi:10.1007/BFb0056301.

57. Bonk, J. F. & Garrett, A. B. A Study of the Silver (I) Oxide-Silver (II) Oxide Electrode. J. Electrochem. Soc. 106, 612 (1959).

58. Takeda, K. & Hattori, T. Optimal Process for Fabricating AgO Cathode for AgO/Zn Cells Improved in High Drain Pulse Performance at Low Temperatures. J. Electrochem. Soc. 146, 3190–3195 (1999).

59. Berchmans, S. et al. An epidermal alkaline rechargeable Ag-Zn printable tattoo battery for wearable electronics. Journal of Materials Chemistry A 2, 15788–15795 (2014).

Chapter 5. Summary and Perspective

As we head toward a greener and more interconnected future, the scientists and engineers of the world must develop sustainable energy generation and storage solutions to combat climate change and pave the way for emerging technologies, such as wearables, 5G, and IoT. As such, to extend operational lifetimes and lower costs of energy generation and storage technologies, we must understand the fundamental degradation mechanisms that limit device performances. This dissertation explores key degradation mechanisms that limit lifetimes in solar module energy generation and Zn-based battery energy storage. The insights learned from the advanced characterization utilized and developed in this dissertation enables enhanced device performances as well as solutions for the broader scientific and research communities to implement.

To extend lifetimes and lower the cost of silicon solar energy generation devices, chapter 1 introduces a characterization technique developed to track sodium ion migration in dielectrics, which is known to degrade solar module performances. The Trap-Corrected Bias-Temperature Stress Method (TraC-BTS) developed accounts for electronic traps when measuring Na^+ ion migration within the antireflection SiNx layer of the module stack. This allows for the extraction of practical ion drift velocities and diffusivities, relevant to solar module degradation temperatures and lifetimes (~25-30 years). The kinetics extracted from the TraC-BTS method are then used to simulate the time of Na^+ to migrate cross the SiN_x layer, thus revealing practical timeframes of module degradation. As a result, it is expected that the solar community will utilize this method to model the degradation of silicon solar modules and to engineer antireflection coatings that can block Na^+ migration and thus extend module lifetimes.

To enable high power and flexible electronics, chapter 2 focuses on developing a high-performance printable and flexible Zn-based battery. Through the optimization of the formulation, fabrication, and cell architecture, a flexible battery with a benign chemistry, a high areal capacity of 54 mAh/cm^2, and a rechargeability of 80 cycles at 8 mAh/cm^2 is developed. Furthermore, through electrochemical characterization, low cell impedances are demonstrated that make this battery ideal for high current pulses undergone in high power electronics. To demonstrate this, the flexible Zn-AgO battery is paired with a flexible display and Bluetooth microcontroller. The flexibility with battery operation is also explored with electrochemical-mechanical device testing and shows the ability to discharge and charge the battery with repeated mechanical bending tests. The flexibility of this battery is also demonstrated with X-ray Micro-scale Computed Tomography (X-ray MicroCT), which illustrates the individual electrode structures and showcases excellent contact of the material layers with mechanical stress.

As X-ray CT (XRCT) was proven to be a useful method to characterize battery device degradation, chapter 3 reviews the uses of XRCT in the present and future analysis of battery systems. In this review, the history of XRCT is outlined, and the key advancements that have enabled the tool for battery characterization are discussed. As such, the virtues and limitations of the tool for a variety of battery chemistries is explored as well as the key morphological parameters that can be extracted. The methods of proper data analysis and filtering is examined, and the emerging uses of artificial intelligence (AI) and machine learning (ML) in battery modelling is discussed. Finally, the review provides a perspective of the future of XRCT, in which AI and ML can be used in combination with XRCT and other techniques to characterize battery systems on multiple length-scales and to develop multi-physics performance-predictive models.

Lasty, chapter 4 explores using XRCT as a tool for long-term *in-situ* characterization of a Zn-based battery system. In this work, *in-situ* CT cells are developed that are performance-representative of the larger form-factor flexible Zn battery introduced in chapter 2. With the developed CT cells, the degradation effects at the anode are explored with high resolution 3D tomograms. The effects of current collector corrosion and gassing on cycle and shelf life are revealed by combining XRCT with electrochemical characterization. Using long-term *in-situ* CT characterization, the evolution of the Zn and ZnO species in the anode is analyzed as a function of cycle and shelf life, and the particle size distribution and Z-axis volume expansion is quantified. Based on these findings, the materials system of the battery is optimized for prolonged shelf and cycle life. The improved materials system demonstrate superior performances (12.5 mAh/cm^2 for >250 cycles) for both *in-situ* CT cells and larger 4 cm^2 form-factor printed cells. These larger format cells exhibits a prolonged shelf life, a cycling volumetric energy density of 104.7 Wh/L, and a power density of 34.6 W/cm^3.

In sumamry, this dissertation explores the characterizartion of energy generation and storage devices for extending operation lifetimes. Through the work with silicon solar modules, a method is developed to quanitfy device degradation for future scientists and engineers to extend lifetimes. Additionally, a Zn-based flexible battery is developed, the degradation mechanisms analyzed with MicroCT, and then greatly improved based on the findings. Finally, with X-ray CT emerging as powerful tool for electrochemical systems, the historical and present uses of CT is reviewed, and a prospective is provided of the future of XRCT in battery research. Finally, the work performed in this dissertation showcases methods for characterizing degradation mechanisms in energy generation and storage systems, and thus will greatly aid the broader scientific and research communities to extend device lifetimes and improve systems to combat climate change and pave the way for emerging technologies.